DIPLOMA THESIS

The effect of cobalt nanoparticles on the microstructure and mechanical properties of hybrid solder joints

carried out at

Technischen Universität Wien
Institute of Chemical Technologies and Analytics

supervised by

Associate Prof. Mag.a rer.nat. Dr.in techn. Golta Khatibi Damavandi
Projektass.in Dipl.-Ing.in Irina Wodak, BSc

by

Sophie Stiefler

23. April 2025, Vienna

Signature

Abstract

The restriction on the use of lead-based solder has created an urgent need to develop alternative materials, that match or exceed the performance of traditional lead-containing solders. Since conventional alloying processes have not been sufficient to achieve the desired properties, new approaches are needed to enhance the performance of solder materials. One promising strategy for improving solder performance is the incorporation of reactive nanoparticles, by adding them to the solder or the flux. They interact with the material at microscopic level. This process enhances key characteristics such as mechanical strength, heat resistance and overall long-term stability. As a result, so called advanced "hybrid solder systems" have developed. This thesis investigates the impact of cobalt nanoparticles (Co NP) on mechanical properties and microstructure of hybrid solder joints, with a key focus on the growth of brittle intermetallic compounds (IMC), the shear strength and time and temperature dependent mechanical properties.

Sn-3.5Ag solder and flux doped with up to 1.00 % cobalt nanoparticles was used to prepare the solder joints. Subsequently, some of the specimens were subjected to a variety of thermal treatments. Metallographic analysis was used to observe microstructural differences and measure IMC thickness to evaluate growth kinetics and the formation of brittle intermetallic compounds. Push-off shear tests provided insights into the mechanical performance. Stress-relaxation tests (SRT), were conducted to measure the relaxation behaviour and calculate the stress exponent to determine the creep resistance.

The results show that the addition of 0.10 % cobalt nanoparticles significantly reduces the growth of the Cu_6Sn_5 IMC layer, with only a slight effect on the Cu_3Sn layer, for as reflow and thermally treated specimen. This reduction in brittle intermetallic compounds growth leads to an improved long-term stability. However, this effect is most pronounced at low concentrations of Co NP additions. Push-off shear tests and the shear tests with the stress-relaxation samples both showed an significant increase in performance with 0.10 and 0.25 % Co NP additions, leading to an improvement of the mechanical properties. Increased concentrations showed no enhancement. The load drop measured in stress relaxation tests did not exhibit any significant change with the addition of cobalt nanoparticles. However, the stress exponent revealed a clear trend, demonstrating that the creep resistance could be considerable improved with the addition of 0.10 % cobalt nanoparticles.

These findings highlight the potential of adding reactive nanoparticles to solve significant issues related to lead-free solder joints, by improving both their initial performance as well as their long-term stability. A key and recent discovery is that the increase in shear strength does not directly correlate with an improvement in creep behaviour of the cobalt nanoparticle doped solder joints. Future research could concentrate on optimizing the nanoparticle concentration and evaluating the effects of other metallic nanoparticles to further improve solder joint properties.

Kurzfassung

Das Verbot bleibasierter Lote hat einen dringenden Bedarf an der Entwicklung alternativer Materialien geschaffen, deren Eigenschaften mit denen traditioneller bleihaltiger Lote vergleichbar sind oder diese sogar übertreffen. Da herkömmliche Legierungsverfahren nicht ausreichen, um die gewünschten Eigenschaften zu erzielen, sind neue Ansätze erforderlich, um die Leistungsfähigkeit der Lote zu verbessern. Eine vielversprechende Strategie, um die Eigenschaften zu verbessern, ist die Zugabe von reaktiven Nanopartikeln. Diese interagieren mit dem Material auf mikroskopischem Level. Dieser Prozess verbessert wichtige Eigenschaften wie die mechanische Festigkeit, die Temperaturbeständigkeit und die generelle Langzeitstabilität, was zu sogenannten fortgeschrittenen "Hybrid-Lötsystemen"führt. Diese Arbeit untersucht den Einfluss von Cobalt Nanopartikeln auf die mechanischen Eigenschaften und die Mikrostruktur von Hybrid-Lötverbindungen, mit einem Fokus auf das Wachstum der spröden intermetallischen Phasen, der Scherfestigkeit und der zeit- und temperaturabhängigen mechanischen Eigenschaften.

Zur Herstellung der Lötstellen wurde Sn-3,5Ag-Lot und Flussmittel verwendet, das mit bis zu 1,00 % Cobalt Nanopartikeln dotiert war. Anschließend wurden einige Proben verschiedenen Wärmebehandlungen unterzogen. Mithilfe von metallographischen Untersuchungen wurden die mikrostrukturellen Unterschiede untersucht sowie die IMC-Dicke, die Wachstumskinetik und die Bildung spröder intermetallischer Verbindungen ausgewertet. Mit Push-off-Scherversuche wurden die mechanischen Eigenschaften der Lotverbindung analysiert. Spannungsrelaxationstests wurden durchgeführt, um das Relaxationsverhalten zu messen und den Spannungsexponenten zur Bestimmung der Kriechfestigkeit zu berechnen.

Die Ergebnisse zeigen, dass die Zugabe von 0.10 % Cobalt-Nanopartikeln das Wachstum der Cu_6Sn_5 Phase sowohl bei as reflow als auch bei thermisch gealterten Proben deutlich reduziert, aber nur einen minimalen Effekt auf die Cu_3Sn Phase hat. Diese Verringerung des Wachstums spröder intermetallischer Verbindungen führt zu einer verbesserten Langzeitstabilität. Dieser Effekt ist jedoch bei niedrigen Konzentrationen von Cobalt Nanopartikel Zusätzen am ausgeprägtesten. Push-off-Schertests und die Schertests mit den Stress-Relaxationsproben zeigten einen signifikanten Anstieg in der Performance bei 0.10 und 0.25 % Cobalt-Nanopartikel zugabe, welche zu einer Verbesserung der mechanischen Eigenschaften führten. Erhöhte Konzentrationen stellen keine Verbesserung dar. Der in Spannungsrelaxationstests gemessene Lastabfall zeigte durch die Zugabe von Cobalt Nanopartikeln keine signifikante Veränderung. Der Spannungsexponent demonstriert jedoch den klaren Trend, dass die Kriechfestigkeit durch die Zugabe von 0,10 % Kobalt Nanopartikeln erheblich verbessert werden konnte.

Diese Resultate heben das Potenzial von reaktiven Nanopartikel-Zugaben hervor, um typische Probleme von bleifreien Loten zu lösen. Dadurch wird sowohl ihre anfängliche Leistung als auch ihre langfristige Stabilität verbessert. Eine wichtige aktuelle Erkenntnis ist, dass eine Erhöhung der Scherfestigkeit nicht direkt mit einer Verbesserung des Kriechverhaltens von Hybridlötverbindungen zusammenhängt. Zukünftige Forschung könnte sich auf die Optimierung der Nanopartikelkonzentration und die Bewertung der Auswirkungen anderer metallischer Nanopartikel konzentrieren, um die Eigenschaften der Lötverbindung weiter zu verbessern.

Contents

1. Introduction

Tin-lead solders have been widely used in the electronic industry for many years due to their excellent soldering properties and proper performance and reliability.[1] But as a consequence of the harmful environmental and health effects of lead, they have been significantly restricted in electronic industries.[2] This created an urgent need for lead-free solders with the same or better properties. However, to become a viable alternative, several criteria must be met, such as:

- similar melting temperatures as tin-lead-solders
- a narrow plastic range
- sufficient wetting properties
- physical properties at least comparable to tin-lead-solders
- good fatigue resistance
- suitable for use with existing liquid flux systems
- relatively non-toxic
- low cost[1]

1.1. Alloying Additions to Bulk Materials

Since there was no drop-in replacement for tin-lead-solders an alternative which meets most of the criteria needed to be found. Therefore the Sn-Ag-Cu-family (SAC) was introduced as the best match for general purpose alloys, with a composition of 3.4 to 4.1 % silver and 0.5 to 0.9 % copper near the eutectic alloy. However all alternatives faced big difficulties due to their melting behaviour. Sn-37Pb for example has an eutectic temperature of 183 °C where as tin, the main component of SAC-solders has a melting temperature of 232 °C, almost 50 °C higher. For this reason alloying additions which fulfil the following requirements where searched:

1. Liquidus temperature close to 183 °C, to avoid changes in manufacturing processes.
2. Only a small difference between solidus and liquidus temperatures, to avoid fillet lifting and tombstoning phenomena.
3. A significantly higher solidus temperature than the maximum operation temperature.

Criteria two can be easily fulfilled with binary or ternary eutectics. Table 1 shows some alternative tin-eutectic alloys divided in tin-rich and addition-rich alloys.

	Alloy	Liquidus temperature
tin-rich alloys	Sn-0.9Cu	227 °C
	Sn-3.5Ag	221 °C
	Sn-0.16Ni	231 °C
	Sn-10Au	217 °C
	Sn-9Zn	199 °C
	Sn-3.5Ag-0.9Cu	217 °C
addition-rich alloys	Sn-58Bi	139 °C
	Sn-59Bi-1.2Ag	138 °C
	Sn-59Bi-0.4Cu	139 °C
	Sn-51In	120 °C
	Sn-33Cd	177 °C

Table 1: Comparison of liquidus temperatures from tin-eutectic-alloys.

The comparison of the tin-rich alloys with the addition-rich shows, that with small amounts of additions, only higher liquidus temperatures can be reached. The SnCd system would fulfil requirement one perfectly, however due to its high toxicity, it is unusable. Although bismuth-containing alloys are a frequently used substitute, their low liquidus temperature makes them unsuitable for some applications. Deciding from the liquidus temperature the SnZn alloy of the tin-rich alloys looks most promising, however, it was observed that, zinc-containing alloys oxidize easily and are therefore prone for corrosion. The SnAu alloy is used only for specialized applications due to the high cost of gold. Therefore the only remaining options, with a liquidus temperature about 35 degrees higher than the tin-lead-solder, are SnAgCu and SnAg.[3]

Even tough these are the best options they are still not good enough, because tin, the major component in both cases, forms layer of intermetallic compounds with common conduction materials like copper, nickel and silver. If these IMCs grow extensively they degrade the mechanical strength, due to their brittleness, and additionally change the electrical characteristics.[4] This layer thickens due to the diffusion of tin from the bulk solder especially during service at higher temperatures. Consequently it is of general interest to research ways to limit the growth of the brittle IMC layer. Since the potential of traditional alloying additions has been fully explored, a novel approach has been introduced, utilizing nanoparticles to enhance the stability of the solder and improve its overall performance.[5]

1.2. Reinforcement through the Addition of Nanoparticles

Studies reveal that the addition of nanoparticles leads to a distinguished increase of hardness, strength and creep resistance of bulk solders. Yet the solder performance not only depends on the bulk properties but as well on the IMC characteristics. As a result of the ongoing miniaturization in modern electronic devices, the intermetallic compound is becoming an increasingly larger part of the solder volume. Which implies that the IMC characteristics are crucial in determining the longevity of solider joints.

The nanoparticles used can be assigned two groups, reactive, metallic, nanoparticles and non-reactive, ceramic or carbon based, nanoparticles. The main methods to incorporate them into the solder are paste mixing [6] and nanoparticle doped flux.[7]

1.2.1. Non-reactive Nanoparticles

Non-reactive nanoparticles are chemically inert, meaning they do not interact with the molten solder during processing or undergo any reactions while in service, making them ideal for maintaining long-term stability. During reflow soldering they act as an heterogenous nucleation site for β-tin and the IMC, which reduces the size of both significantly. Therefore, the non-reactive nanoparticles can be found mainly in the fracture surface of solder joints.[8]

Ceramic nanoparticles

The most commonly used ceramic nanoparticles are ZrO_2, Al_2O_3, SiO_2 and TiO_2. Due to the absorption on the grain boundaries during soldering, the nanoparticles suppress the growth of the IMC.[9] Figure 1 depicts the decreased IMC thickness and risen shear strength with the addition of ZrO_2, SiO_2 or TiO_2. However, the data also indicate that the incorporation of a substantial amount of ceramic nanoparticles results in a noticeable reduction of this effect. This phenomenon is likely due to the tendency of the nanoparticles to cluster together, resulting in agglomeration and segregation. As a result, the intended reinforcement provided by the nanoparticles may be reduced, potentially altering the expected mechanical performance of the composite.[10] Similar improvements were also reported by Tsao et al. (2011)[11] for TiO_2, Wang et al. (2015)[12] for SiO_2, and Gain et al. (2011)[13] for ZrO_2.

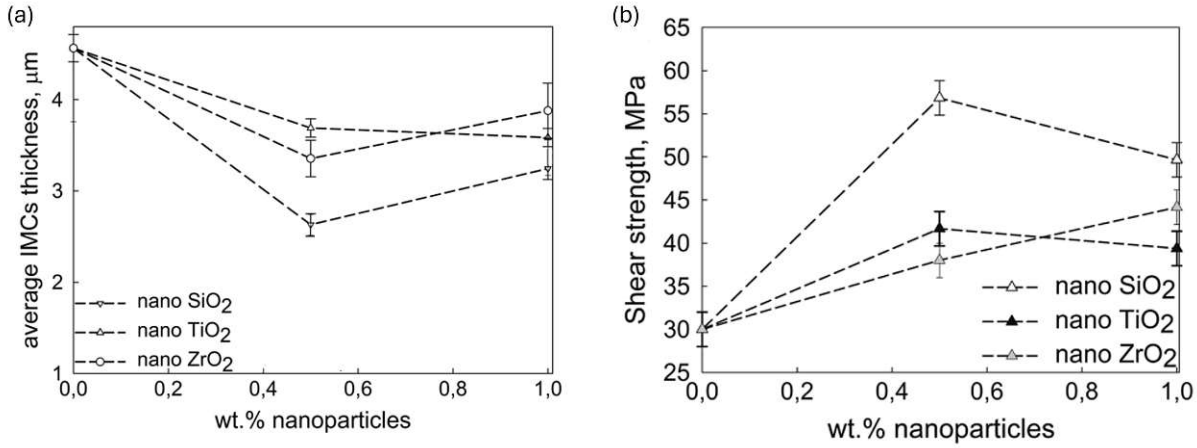

Figure 1: (a) IMC thickness and (b) shear strength with the addition of ceramic nanoparticles.[10]

Carbon based nanoparticles

With the addition of carbon-based nanoparticles, such as carbon black (CB), graphene (G) and single-walled carbon nanotubes (SWCNT), metal matrix nanocomposites can be produced. These incorporations can result in improved mechanical strength, greater resistance to wear and fatigue, and enhanced electrical conductivity, making the material more durable and versatile for various applications. Figure 2 illustrates the observed increase in both hardness and shear load as a result of incorporating different types and varying concentrations of carbon based nanoparticles. This trend highlights the strengthening effect of nanoparticles on the overall properties of the material.[14] Van Son et al. (2012)[15], Zhu et al. (2028)[16], and Sun et al. (2016)[17] also investigated the influence of carbon nanoparticles and reported enhanced properties.

(a)

Solder samples	Induction mixed and cast in vacuum at 1200 °C
CS	C-Solder®
CB_0.01	C-Solder® reinforced by 0.01 wt.% CB
CB_0.05	C-Solder® reinforced by 0.05 wt.% CB
G_0.01	C-Solder® reinforced by 0.01 wt.% graphene
G_0.05	C-Solder® reinforced by 0.05 wt.% graphene
SWCNT_0.01	C-Solder® reinforced by 0.01 wt.% SWCNT
SWCNT_0.05	C-Solder® reinforced by 0.05 wt.% SWCNT

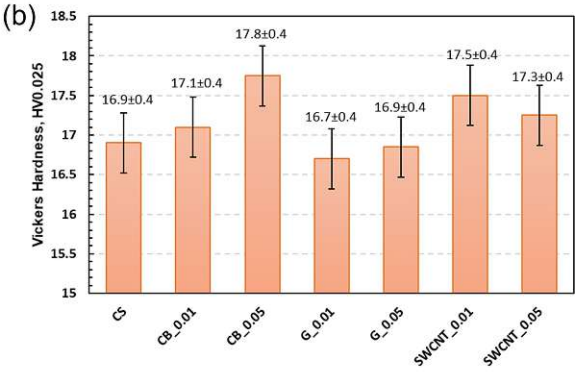

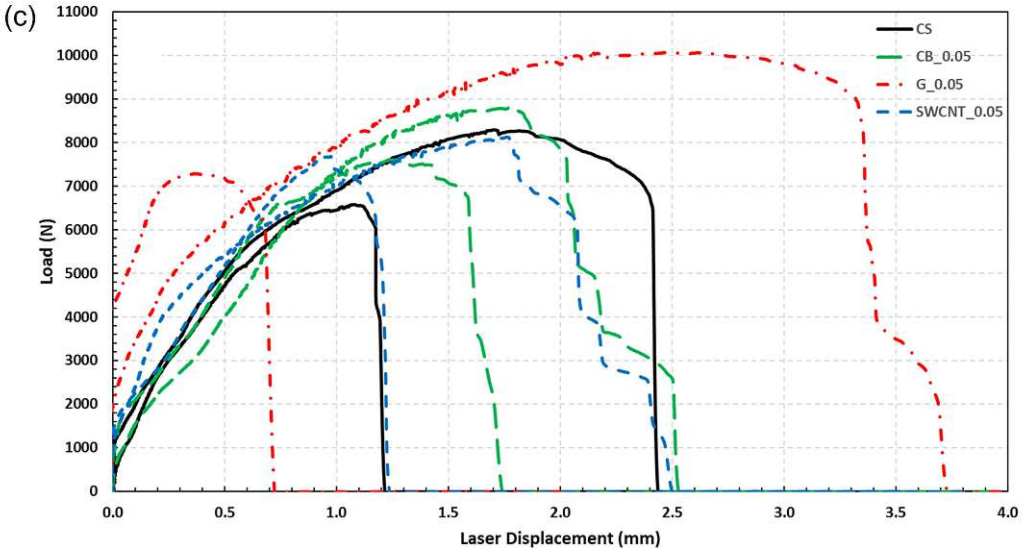

Figure 2: An (a) overview of the samples with C-Solder® a commercial tin-based lead-free soldering alloy and (b) their Vickers hardness and (c) shear load with different carbon additions and amounts.[14]

1.2.2. Reactive Nanoparticles

Reinforcing solder joint through the addition of reactive nanoparticles, can regulate the IMC thickness and morphology, as a consequence of the alloying effect by absorbing at the interface.[7] Typical metallic nanoparticles are Cu, Ni, Co, Zn, Mo, Mn and Ti. These elements have a wide range of properties like melting point and oxidation stability. These additions can increase strength, hardness and creep resistance.[6]

The decrease of the IMC thickness with the addition of cobalt and nickel nanoparticles to the flux of SAC solder joints is depicted in Fig. 3.[18] Sujan et al. (2014) [7] report that Co and Ni primarily remain at the interface, with only small amounts located near it. They undergo reactive dissolution during reflow, which affects the IMC thickness through alloying. They also suggest that the nanoparticles influence the nucleation process, leading to fine and numerous nuclei, which could be the reason for the initial IMC thickness reduction. It is noticeable that this effect is only observed with small additions and does not influence the IMC thickness at higher concentrations. This may happen because with the dissolution of more nanoparticles, the copper consumption increases, causing a reduction in copper concentration that could destabilize the interfacial product and lead to detachment.[18]

An enhancement in both shear strength and Vickers hardness for cobalt nanoparticle reinforced solder joints produced by solder paste mixing is demonstrated in Fig. 4. The shear strength is the highest at 0.3 %, then declines with further additions, ending up even lower than without cobalt nanoparticles. The different optimal cobalt nanoparticle concentration compared to the example in Fig. 3, can be explained by the contrasting methods used to incorporate them. However, the Vickers hardness shows a different behaviour, it continues to rise with increasing additions, although the rise slows down. Huang et al. explained, that the rise of shear strength with limited Co addition was caused by Orowan strengthening through Co particles situated at interfaces and grain refinement of $(Cu,Co)_6Sn_5$. Excessive increases in the Co content, up to 0.7 wt%, resulted in particle agglomeration, leading to structural discontinuities and the formation of thicker needle-shaped IMC, which may induce increased internal stresses. [19] Similar improvements were also observed by Shang et al. (2019)[20] for Cu, Yang et al. (2021)[21] for Mo, Lee et al. (2008)[22] for Co, Ali et al. (2016)[23] for Fe, and Yao et al. (2008)[24] for Ni.

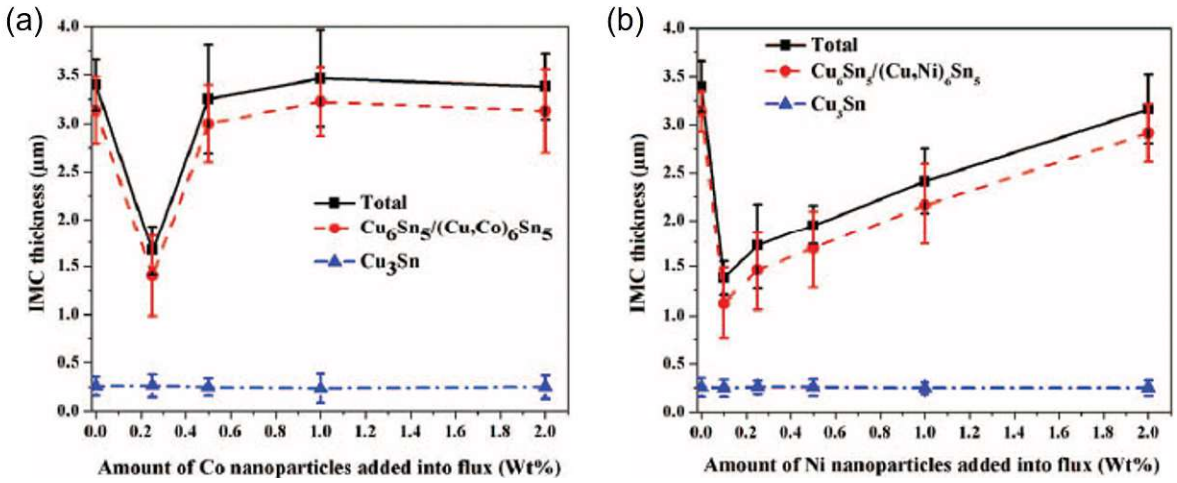

Figure 3: IMC thickness with the addition of (a) cobalt and (b) nickel nanoparticles.[18]

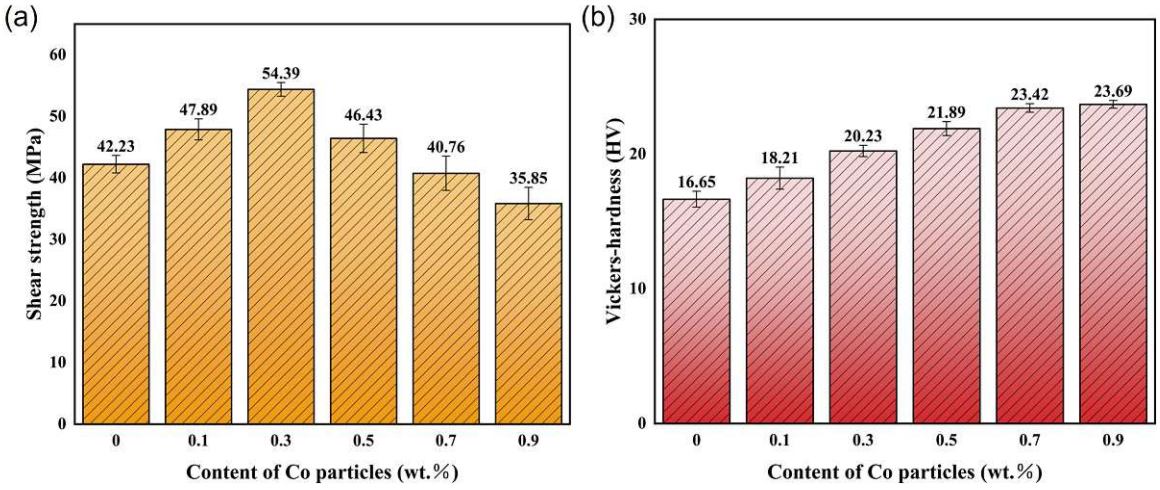

Figure 4: (a) Shear stress and (b) Vickers hardness with the addition of cobalt nanoparticles.[19]

1.2.3. Incorporation of Nanoparticles

One possibility to incorporate nanoparticles is the solder paste mixing method. As the name suggests, the solder paste is mixed with the nanoparticles and then blended for several minutes to get a homogeneous paste.[25] This method is very simple but it also brings some problems. A major drawback is the large amount of nanoparticles required, as a large part of it ends up in the bulk and not only cannot be used, but also has negative effects on the solder, because they reduce the ductility through the formation of IMC within the bulk. Another drawback is the increase of the viscosity, since the paste already has micron sized particles before the nanopowder addition, the stickiness gets enhanced leading to a decreased wettability.

To manage these concerns there is an approach to deposit the nanoparticles on the substrate before the solder gets applied.[18] More precisely, nanoparticles are incorporated into the flux. Solder joints prepared using this method are referred to as "hybrid solder joints". The manufacturing process is similar to the paste mixing, first the flux and the nanoparticles get mixed an then mechanically stirred for several minutes.[26] Since the nanoparticles are applied exactly where they are crucial, only smaller amounts are needed which also makes this method more cost effective. Further advantages are, that thereby the negative impacts on the bulk can be prevented and that the control of the whole system gets better.[25] A comparison of the two methods is shown in the Fig. 5.

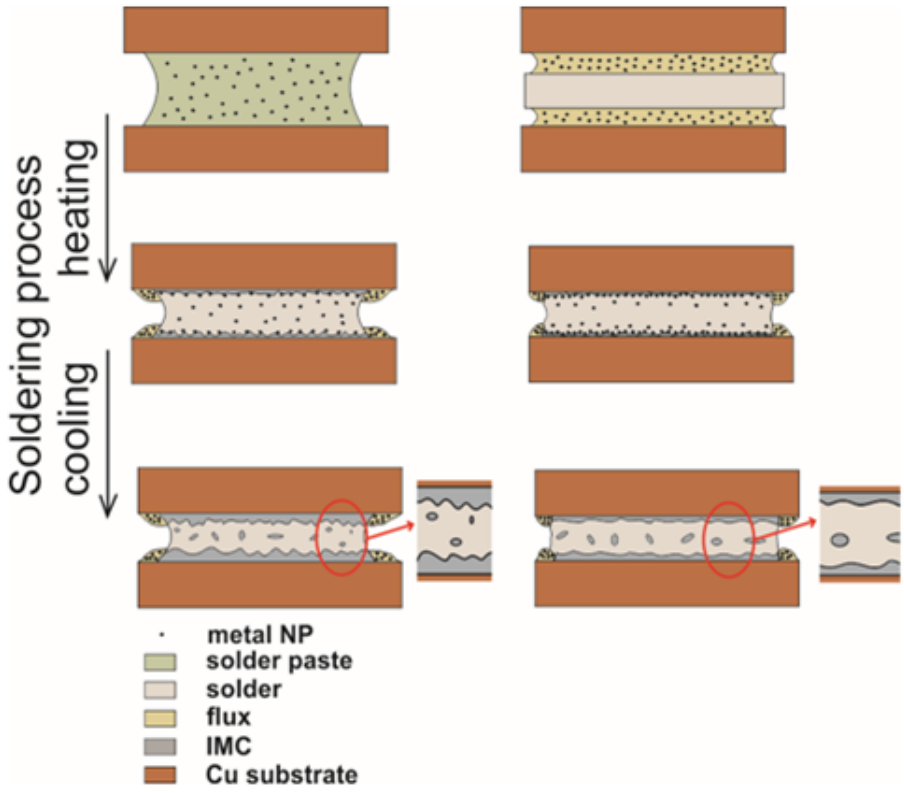

Figure 5: Demonstration of the incorporation of nanoparticles through solder paste mixing and flux doping.

1.3. Sn-3.5Ag Solder and Intermetallic Compounds

In Figure 6, an SEM image of the solder joint is displayed, providing a detailed close-up of the intermetallic compound and the surrounding solder, illustrating their microstructural characteristics. Examining the Sn-Cu phase diagram in Fig. 7 (a), it becomes evident that at a soldering temperature of 280 °C, as indicated by the blue line shown in (a), two distinct intermetallic phases, Cu_3Sn and Cu_6Sn_5, are formed. These phases emerge as a result of the interaction between tin and copper within the solder, following the phase equilibrium conditions depicted in Fig. 7 (a). As evident from the microstructural image, the darker IMC layer that forms directly next to the copper substrate corresponds to the copper-rich Cu_3Sn phase, whereas the lighter IMC layer situated closer to the tin region represents the Cu_6Sn_5 phase. The difference in contrast between these phases can be attributed to variations in their composition and therefore different electron scattering behaviour, where Cu_3Sn absorbs more electrons and appears darker, while Cu_6Sn_5, being richer in tin, exhibits a relatively lighter shade.

As a solder material tin with 3.5 % silver can be used. It consists of tin-rich dendrites that are surrounded by an eutectic mixture of β-tin and small amounts of Ag_3Sn according to the phase diagram of Sn-Ag in Fig. 7 (b). Fine and hard Ag_3Sn precipitates play a crucial role in improving the overall mechanical strength of the material through dispersion hardening. These uniformly distributed precipitates act as obstacles to dislocation motion, improving the resistance of the material to deformation and increasing its durability [8]

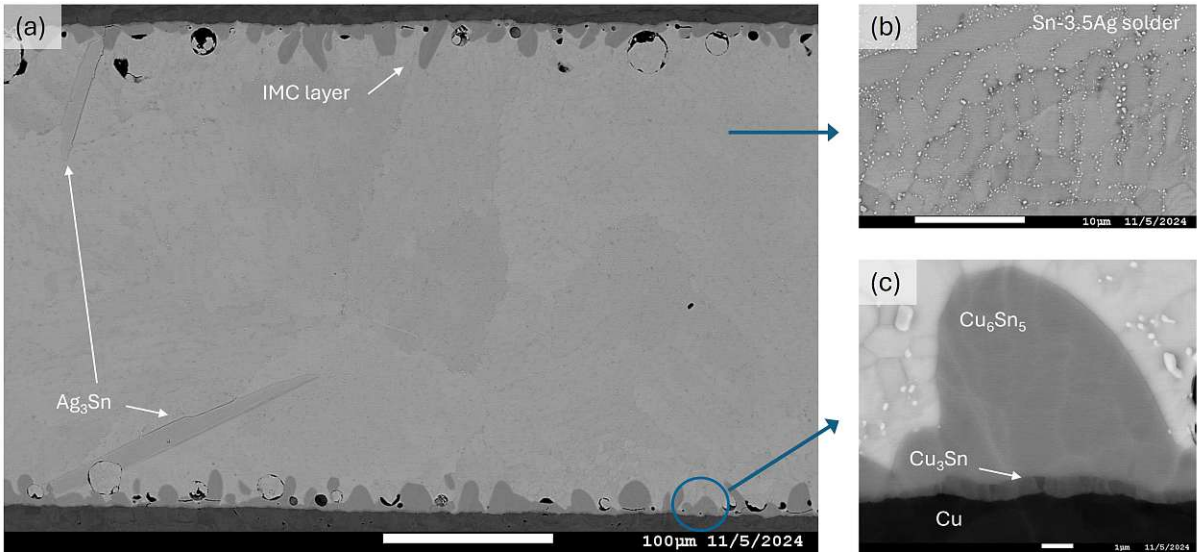

Figure 6: SEM image (a) of the solder joint with a close up of (b) the solder and (c) the IMC.

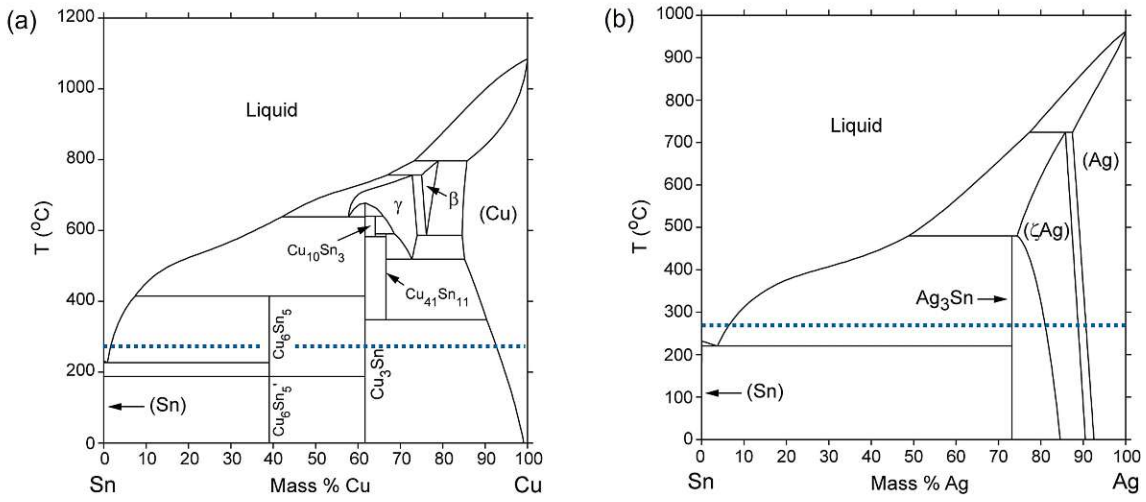

Figure 7: Phase diagrams of (a) tin-copper [27] and (b) tin-silver alloy, with the soldering temperature marked blue[28].

1.4. Importance of Flux during Soldering

Fluxes are important, because they play a crucial role in cleaning the metal surface before soldering while also preventing the formation of further oxides, that could interfere with the bonding process. The copper substrate has three different layers, the pure copper, the absorption layer and the adhesive layer. The reaction layer contains strongly bound materials like oxides, carbonates, sulphides and residues from the production, which need to be removed. At the absorption layer, gases, water, and residues from previous procedures are collected and must be dissolved before soldering. Furthermore some substrate molecules must be dissolved to initiate the formation of IMC. Beyond the fundamental roles of cleaning and covering, fluxes also require several additional secondary characteristics to be effective in soldering processes. These include the ability to withstand the high temperatures, typically encountered during soldering, without degrading, as well as the capability to leave easily removable residues, after the process is completed. Furthermore, fluxes must not attack or corrode the joint or surrounding materials, ensuring the integrity of the assembly. They also need to be effective in breaking down any oxides that may have formed on the surface of the molten metals, for better adhesion. These requirements can vary depending on the specific demands of the application, and therefore, the flux formulation must be tailored to meet the particular specifications of the material and process involved.

Figure 8 displays a close up of a copper sheet with a thin oxide layer, flux and solder, where the solder is melting and flowing. During heating the flux melts and becomes chemically active, in the process it dissolves the oxides from the surface in addition to preventing further oxidation. As the cleaned surface is wetted by the solder, it displaces the flux, allowing the fluxing action to progress, which in turn enhances the wetting. The effectiveness of fluxes ability of removing oxides is considered with the activity. For thin oxide layers only a low activity is needed, whereas thicker layer requires a higher activity.

However, higher activity also results in more corrosive residues, which may corrode the solder. Therefore, the type of flux has to be appropriate for the purpose of use.

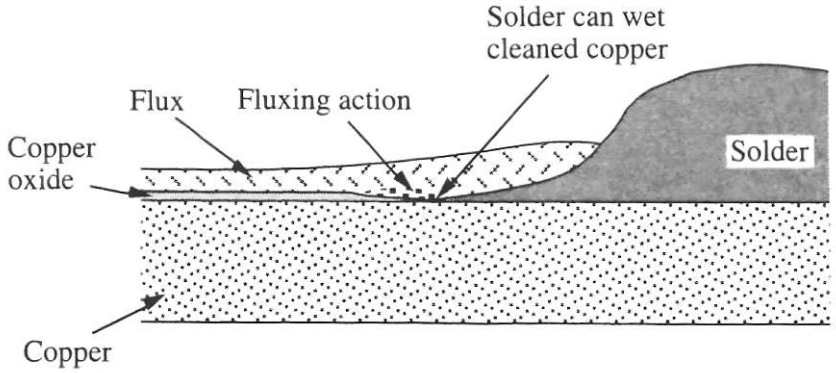

Figure 8: Close up of the flux action during soldering.[29]

Fluxes can be categorized in many different ways, therefore the International Standards Organisation distinguishes them by four variables:

- Flux type: Whether it exists in resin-based, non-resin organic, or inorganic form.
- Flux basis: If it is based on natural occurring or synthetic materials.
- Flux activation: If an activator is included and which type.
- Flux form: Whether it is liquid, solid or paste.

Another common characterization is whether the residues are organically or water soluble. In the following, the different flux types, resin, organic or inorganic, and their properties are examined more closely.

The resin used in flux is dissolved in an organic solvent, such as alcohol, and the residues can also be removed using an organic solvent. Rosin which is natural occurring and obtained from pine tree sap, has excellent properties [29] and consits of 80 to 90 % abietic acid ($C_{20}H_{30}O_2$), 10 to 15 % dehydroabietic acid ($C_{20}H_{28}O_2$) and dihydroabietic ($C_{20}H_{32}O_2$), and the rest is natural matter.[30] It is liquid and therefore active at soldering temperatures and mildly acid, leading to great wetting abilities for metals with a thin oxide layer. Additional the residues are solid after soldering and do not react or corrode the joint, therefore no cleaning is required. However due to the mild activity it is only suitable for thin oxide layers. Synthetic resins perform very similar and have some additional advantages like a greater consistency of quality and lower fuming. For metals that are too tarnished activators need to be added, which however lead to corrosive residues. Typical activators are shown in table 2. This leads to another categorisation of fluxes: halide free fluxes. Certain international and military standards prohibit the use of halide as a result of their corrosiveness, compared to other activators.

Table 2: Activators used in resin fluxes

	Name	Formula
organic halide salts	dimethylammoniumchloride	C_2H_8ClN
	diethylammoniumchloride	$C_4H_{12}ClN$
organic mono-basic acids	formic acid	CH_2O_2
	acetic acid	$C_2H_4O_2$
	propionic acid	$C_3H_6O_2$
organic di-basic acids	oxalic acid	$C_2H_2O_4$
	malonic acid	$C_3H_4O_4$
	sebacic acid	$C_{10}H_{18}O_4$

Organic and inorganic fluxes lead to water soluble residues most of the time. To take over where the resin based fluxes reach their limit, they are often produced to be highly active, so that they can cope with high amounts of oxides and since the highly corrosive residues are water soluble, they can be easily removed. Their formulation is based on the activator used, some common organic and inorganic ones are salts, acids or amines are shown in table 3. However, the solvents typically include some form of alcohol or water which is not ideal because water, tends to spatter when heat is applied rapidly.

Table 3: Activators used in organic and inorganic fluxes

		Name	Formula
organic	salts	dimethylammoniumchloride	C_2H_8ClN
	acids	lactic acid	$C_3H_6O_3$
	amines	urea	CH_4N_2O
inorganic	salts	zinc chloride	$ZnCl_2$
	acids	hydrochloric acid	$HCl \cdot x(H_2O)$
	amines	ammonia	NH_3

The flux used is typically chosen to suit the cleaning process and considers how clean the assembly is prior to fluxing and whether it must be cleaned after soldering.[29]

1.5. Stress-Strain Relationship

Most materials are subjected to forces or mechanical loads during their use, and their mechanical behaviour reflects how they respond to these loads. The most important mechanical properties are the strength, hardness, ductility and toughness. When testing materials the the type of load, impact duration and the surrounding must be taken into account. If the impact is static or only changes slowly and the force is evenly distributed on the cross section, the mechanical properties can be determined using stress-strain measurements. The tests are conducted using tensile, compression, shear stress. Additionally torsion stresses can also occur. These types of stress can be seen in Fig. 9.

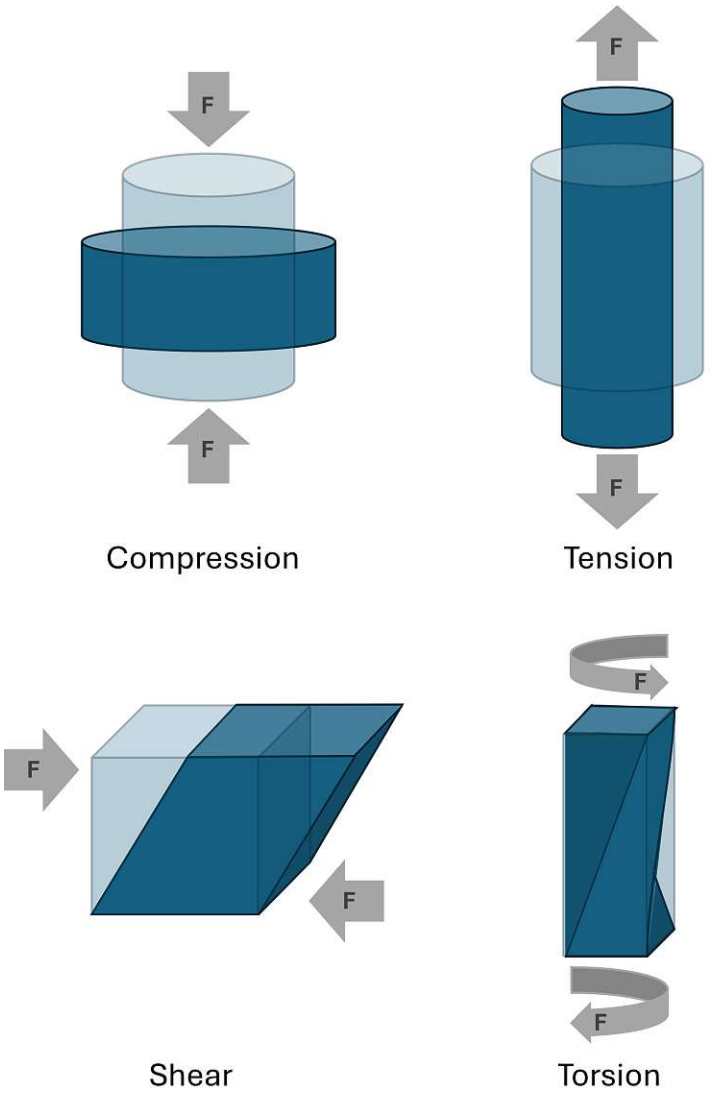

Figure 9: Types of stress that deform materials.

Tensile testing is the most frequently used method, during testing, the sample is exposed to tensile load perpendicular to its cross section, which deforms the specimen until failure, producing a force. During the experiment the sample is clamped in the test machine and the longitudinal extension is recorded with an extensometer during the force application,

producing an extension curve. However, both tensile force and extension are dependent on the geometry of the specimen, meaning no qualitative results can be obtained just comparing the curves. Instead, the tensile force and the extension are standardized to stress σ in MPa and strain ϵ which is dimensionless. Equations 1 and 2 show the conversion containing the force F, the initial cross-sectional area A_0, the initial length l_0 and the current length l_i.

$$\sigma = \frac{F}{A_0} \tag{1}$$

$$\epsilon = \frac{l_i - l_0}{l_0} = \frac{\Delta l}{l_0} \tag{2}$$

Compression tests are especially important for materials which exhibit compression forces during use. The experiment is conducted the same way as tensile test, with the only difference that the direction of the force changes and that the sample is compressed when there is unhindered lateral expansion. Therefore the compressive stress and compressive strain can be calculated with equations 1 and 2 too, with the change that the signs are negative. Compression tests are mostly used for materials not suitable for tensile test, for example due to brittle behaviour.

In shear test, the sample is subjected to shear loads which are directed parallel to the lap-shear joint as depicted in Fig. 10. The shear stress τ and the shear strain γ are calculated in equations 3 and 4 with the expansion angle θ shown in Fig. 10. Torsion is a variant of shearing, in which the specimen gets twisted. It is mainly used for machine axes or drive shafts.

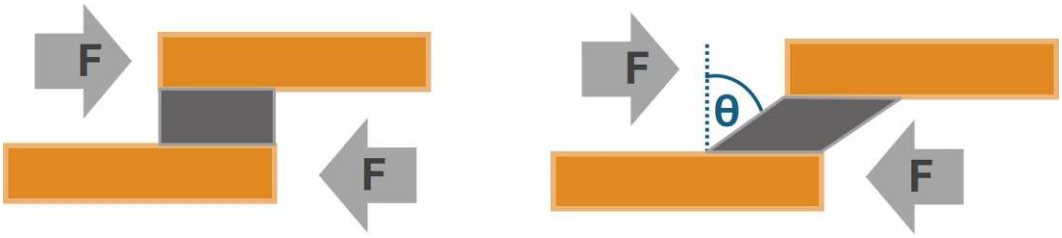

Figure 10: Scheme of a shear test with lap-shears joints.

$$\tau = \frac{F}{A_0} \tag{3}$$

$$\gamma = tan(\theta) \tag{4}$$

The strain of a material is determined by the applied stress, and at low loads the connection is linear. This dependency can be described by Hooke's law in equation 5. Defined by the slope of the stress-strain curve, the Young's modulus E in GPa characterizes the elastic deformation region, where deformation increases proportionally with stress. It is an indicator of stiffness, representing the material's resistance to elastic deformation.

This deformation is a reversible phenomena, because after removing the load the sample returns to its original shape.

$$\sigma = E \cdot \epsilon \tag{5}$$

Figure 11 represents a typical stress-strain curve under tensile load for a material without yield point. The linear region from the start until B shows the reversible elastic deformation, which is followed by irreversible plastic deformation. Which occurs as a result of slipping processes, where dislocation movements take place. In most materials, this transition is continuous and is marked by a curvature that evolves as stress increases. This point is called the proportional limit stress, which is difficult to determine. However, through shifting Hooks line to 0.2 % strain, the yield strength can be easily calculated. But some steels show a different behaviour, where the transition is abrupt which leads to an easily determinable yield point. In the region after B strain hardening is happening, leading to lower a stress increase until the maximum stress is achieved in C, which is called the ultimate stress. Beyond this point, necking begins, causing the cross-section to reduce and resulting in a higher stress per area. This phase ends with the fracture of the sample depicted in D, leading to the elongation after rupture, which describes the ductility of a material.[31]

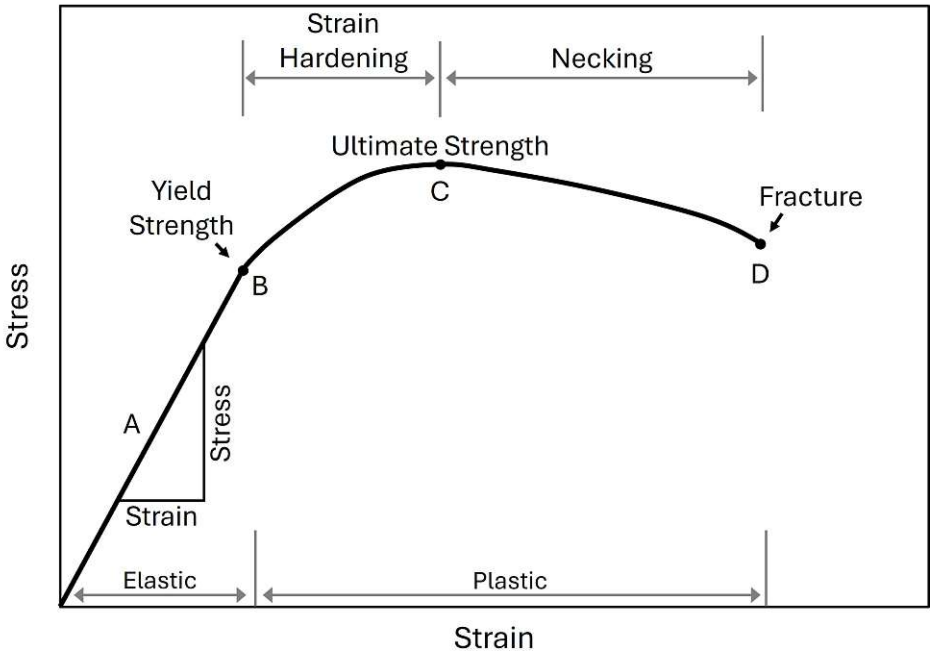

Figure 11: A typical stress–strain curve for a material without yield point.

1.6. Time and Temperature dependent Properties

The time-dependent deformation of materials under constant stress is called creep. This phenomenon is observed in all types of materials and leads to shorter lifespans. Creep in metals typically becomes significant at temperatures above approximately 40 % of their melting point. In a standard creep test, the specimen is subjected to a uniform load or stress while being maintained at a stable temperature. Most investigations are done at a constant load since the area changes during testing which makes it difficult to maintain a constant stress.

A typical creep curve of metals under constant load can be seen in Fig. 12. The onset of stress leads to a sudden purely elastic deformation, afterwards three different areas can be seen. In the first stage, the primary or transient creep, the creep rate and the rise of the curve decreases constantly. As strain hardening progressively intensifies throughout the deformation process, the energy requirements for this deformation significantly increases. The start of the constant creep rate marks the secondary or steady state creep, where the curve shows a linear progression. This stage is usually the longest. The constant creep rate is explained by the balance of the strain hardening process and recovery, where the material regains its ability to plastically deform. As the creep rate increases, the tertiary creep phase begins, which is characterized by accelerated deformation due to microstructural damage such as the formation of cracks, pores and voids as well as separation at grain boundaries. This progressive damage ultimately leads to the complete failure of the material, which is also called creep fracture. In addition, necking can occur within the deformation area under tensile stress. This leads to a reduced effective cross-sectional area, therefore increasing the strain rate.

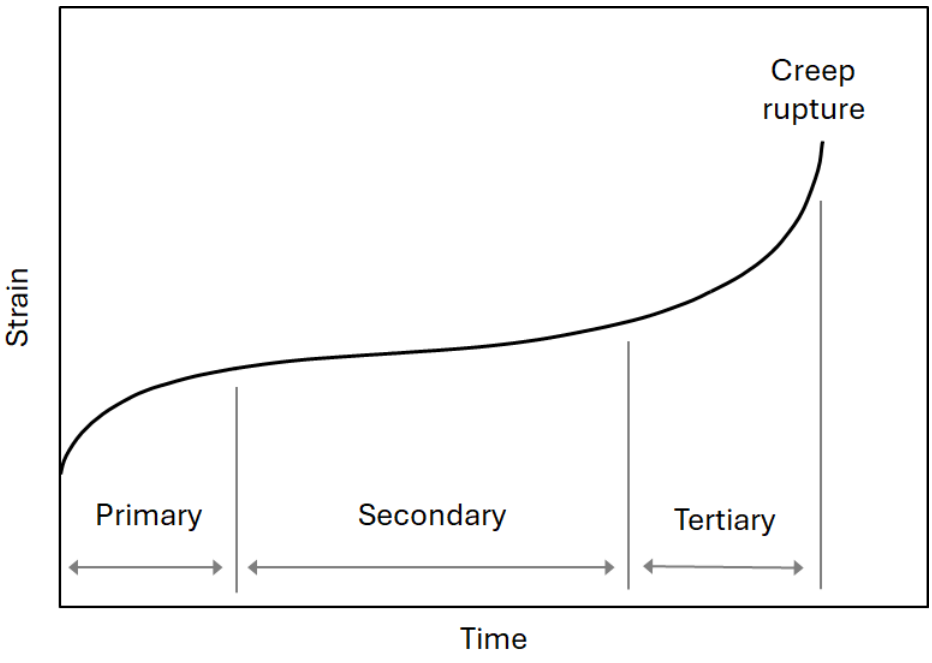

Figure 12: Strain-time-curve at constant load and temperature.

One of the most important values gained during creep tests is the slope of the secondary creep region, which is known as the steady-state creep rate $\dot{\epsilon}_s$, it is calculated in equation 6 by dividing the change of stress $\Delta\epsilon$ by the change of time Δt. This value is especially important for mechanical engineers when designing components that are intended for long periods of use. Whereas for short-term creep situations the time until creep fracture is more important. Therefore creep tests must be carried out until failure, which are called creep fracture tests in this case. These properties make it possible to evaluate the suitability of a material for specific applications.

$$\dot{\epsilon}_s = \frac{\Delta\epsilon}{\Delta t} \tag{6}$$

The temperature, similar to the applied stress, has a massive impact on the creep behaviour, this is depicted in Fig. 13. The curve shown at the bottom represents temperatures that are below 40 % of the material's melting point. In this temperature range, only the initial phase of elastic deformation is observed. After this initial elastic response, the strain remains independent of time, meaning that no significant time-dependent deformation can be seen beyond this point. At temperatures above this limit the following phenomena can be observed when the stress or temperature increases:

- The elastic deformation, that occurs immediately after the onset of tension, increases.
- The steady-state strain rate increases.
- The time until fracture decreases.

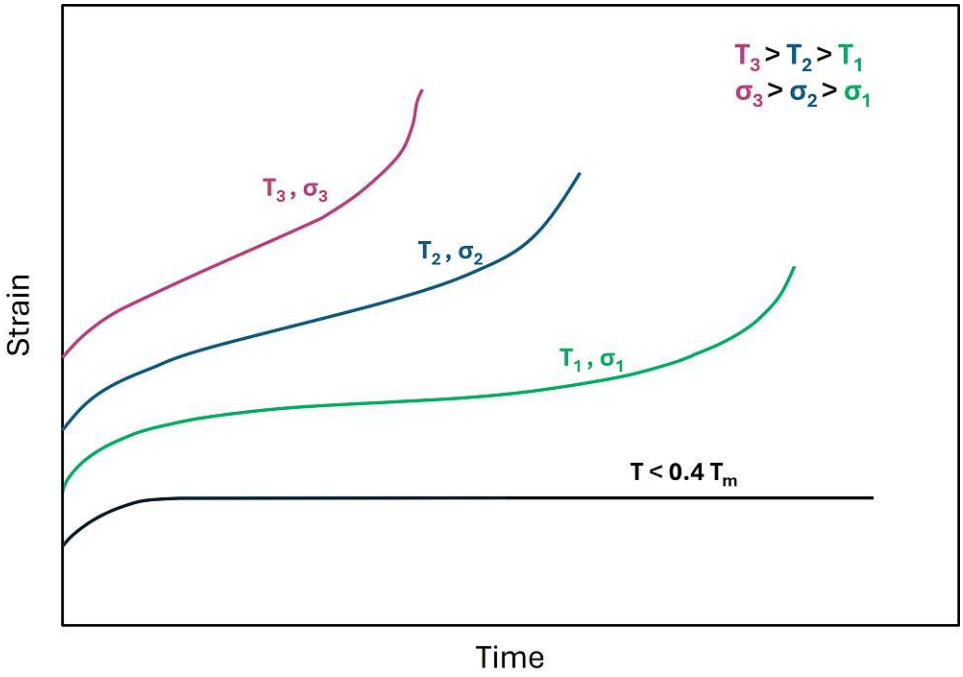

Figure 13: Influence of temperature and stress on the creep behaviour.

The dependence of the stationary creep speed on stress and temperature is described in equations 7 and 8, where 7 is a more simplified version. K_1 and K_2 are material-dependent

constants, σ represents the applied stress, n is the stress exponent, that determines the relationship between stress and strain rate, E_A is the activation energy for the creep process, R is the universal gas constant and T is the absolute temperature at which the process is measured.

$$\dot{\epsilon}_s = K_1 \cdot \sigma^n \tag{7}$$

$$\dot{\epsilon}_s = K_2 \cdot \sigma^n \cdot e^{-\frac{E_A}{R \cdot T}} \tag{8}$$

To describe the creep behaviour of materials, numerous models have been developed, each accounting for different deformation mechanisms. These fundamental mechanisms include grain boundary diffusion, vacancy diffusion, grain boundary sliding, and dislocation motion. Since each mechanism contributes differently to the overall deformation process, they lead to distinct values of the stress exponent, which serves as an indicator of the dominant creep mechanism under specific conditions. The comparison of experimentally determined stress exponent values with theoretical predictions from different models allows the identification of the most relevant creep mechanism for a given material.[31]

1.6.1. Stress Relaxation Theory

Another approach to studying creep behaviour is through stress-relaxation tests, which characterize time-dependent deformation under constant displacement displayed in Fig. 14.

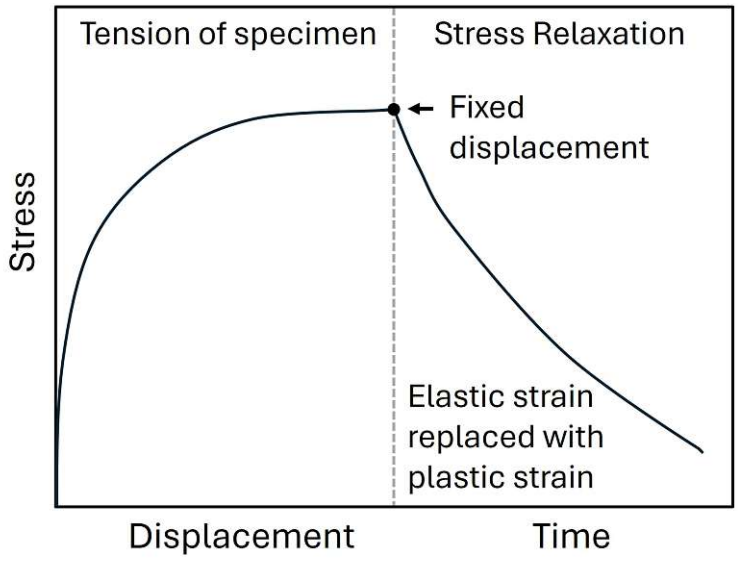

Figure 14: Illustration of stress relaxation tests.

They are especially useful, because they better represent the stress history experienced by solder joints, which undergo thermomechanical cycling during service.[32]. Another advantage is that a single test creates data that represents the stress-strain relationship

across a broad spectrum of stresses at the testing temperature, which is less time consuming compared to creep tests. Furthermore, the plastic strain increment is small leading to only minimal microstructural changes, making the measured stress-strain rate specific to the respective microstructure.[33] During the deformation the total strain, consisting of plastic ϵ_p and elastic strain ϵ_e, remains constant. However the elastic strain gets replaced with the plastic strain due to creep, resulting in a stress reduction as shown in Fig. 14. This subsequent load drop is recorded over time. Considering the stress-strain relationship discussed earlier in equation 5, the stress reduction over time $\frac{d\sigma}{dt}$ can be described by equation 9.[32]

$$\frac{d\sigma}{dt} = E \cdot \frac{d\epsilon_e}{dt} = -E \cdot \frac{d\epsilon_p}{dt} \tag{9}$$

Using a power law relationship, the temperature dependency of stress-relaxation can be calculated using equation 10, where B is a constant.[34] Comprehensive instructions for calculating the stress exponent are outlined in the Experimental section.

$$\dot{\sigma}_p = B \cdot \sigma^n \cdot e^{-\frac{E_A}{R \cdot T}} \tag{10}$$

2. Experimental Procedures

2.1. Sample Preparation

For the preparation of the samples, cobalt nanoparticles, obtained from Nanografi Nanotechnology, were used. The nanoparticles had an average particle size of 28 nm, a purity of 99.85 % and were partially passivated. A transmission electron microscopy (TEM) image of cobalt nanoparticles is presented in Fig. 15, in which the oxide layer with a thickness ranging from 2 to 7 nm can be seen.

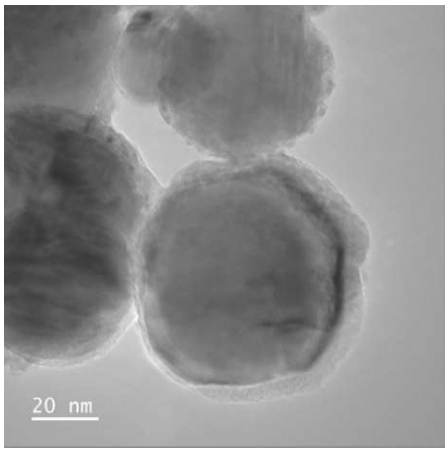

Figure 15: TEM image of Co NP

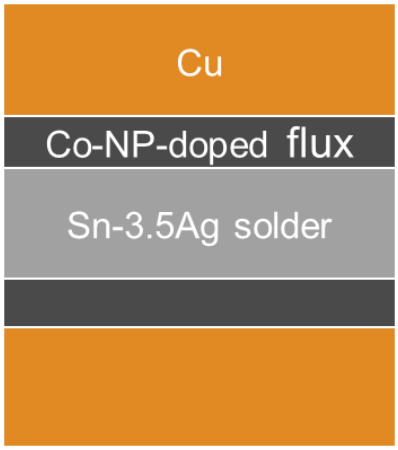

Figure 16: Structure of the sample

To minimize agglomeration, the cobalt nanoparticles were mixed with flux from Stannol GmbH & Co. KG for at least 30 minutes with an ultrasonic lance. Using this methodology, five different concentrations were made: 0.00, 0.10, 0.25, 0.50 and 1.00 wt. % Co NPs in the flux. As a solder, commercial Sn-3.5Ag foil was used. A single fold was applied, resulting in a final height of 0.2 mm. Before assembling the sample, the copper substrate was abraded with 1200P SiC sandpaper and subjected to ultrasonic cleaning using isopropanol. To create the solder joint, the flux was first applied to the lower copper plate with a cotton swab so that the entire surface was covered with a continuous, visible layer. Care was taken to ensure that the same amount was always applied. Subsequently, the folded solder foil was positioned on the surface and coated with an another layer of flux. In the last step the upper copper plate was arranged atop. The structure of the sample is depicted in Fig. 16. To ensure proper alignment of the lap-shear joints during assembly and soldering, an aluminium mount, shown in Fig. 17, was used. To maintain consistency, six samples were fitted into the mount during each soldering process.

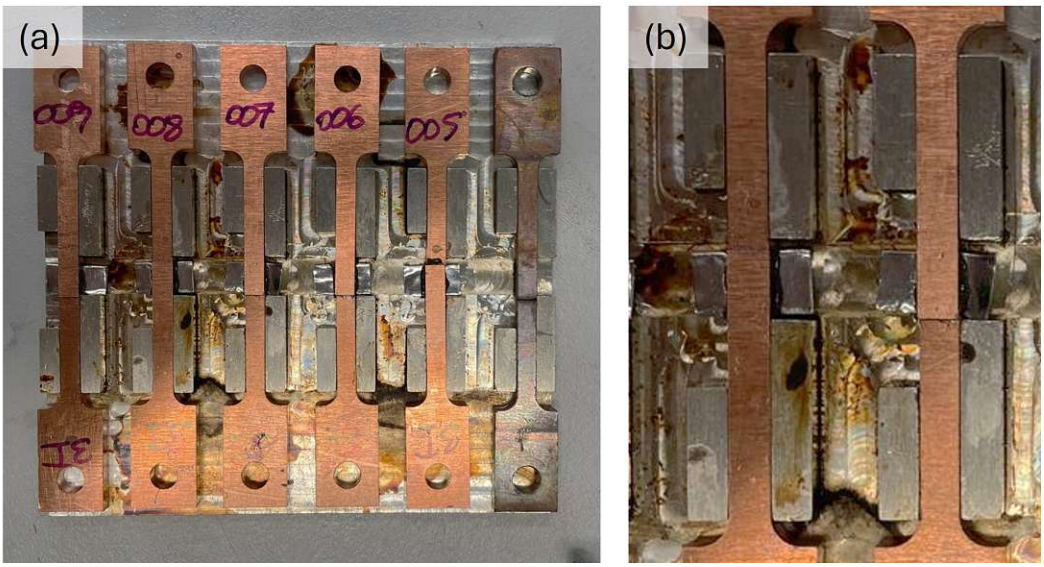

Figure 17: (a) Preparation of lap-shear joints (b) with a close up of the solder joint.

The prepared solder joint was subjected to a reflow soldering process for 4 minutes at 180 °C, followed by an additional 6 minutes at 270 ° C. After air cooling, several of the specimens were thermally aged at 120 or 180 ° C for 10 or 20 days as summarized in table 4. Three different sample types were used, which are depicted in Fig. 18. Sample (a) was used for metallography, (b) for the push-off shear tests and (c) for the stress-relaxation tests.

Table 4: Overview of the used thermal treatments.

Name	Thermal Treatment
as reflow	reflow soldered for 4 minutes at 180 °C followed by 6 minutes at 270 ° C
120 °C 20 d	as reflow + aging for 20 days at 120 °C
180 °C 10 d	as reflow + aging for 10 days at 180 °C
180 °C 20 d	as reflow + aging for 20 days at 180 °C

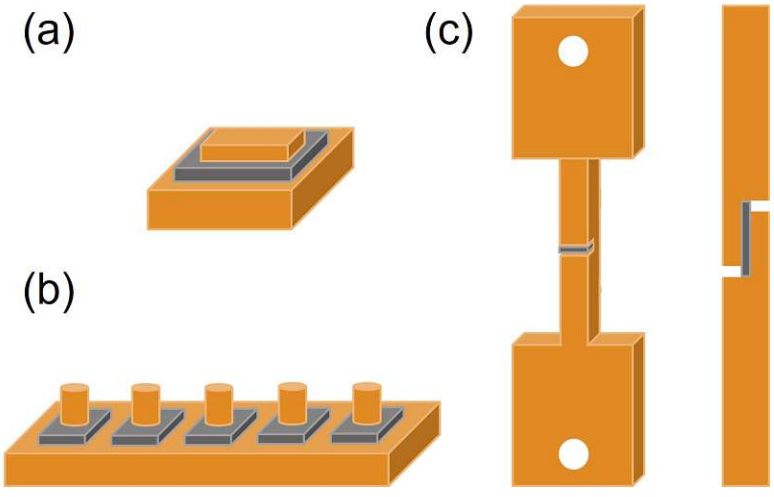

Figure 18: (a) Metallography sample (b) push-off shear test sample (c) lap-shear sample.

2.2. Metallographic and Mechanical Testing Methods

2.2.1. Investigation of Microstructural Differences

In preparation for microstructural analysis, the samples were grinded with P600, P1200, P2400, and P4000 SiC sanding papers. Subsequently, they were polished using a 1 µm diamond suspension followed by OP-S, an amorphous silicon dioxide polishing agent, with each polishing step lasting for about 10 minutes. To investigate the samples, images of the solder joint and IMC were obtained using both light microscopy (Olympus GX 51) and scanning electron microscopy (Quanta 200). For a better characterization of the IMC behaviour a few stress-relaxation samples where deep etched until solely the IMC remained. Therefore, a procedure similar to Jacksons was used [35]. First the sample was grounded using P400 SiC sanding paper and then treated with 20 % 3 M HCL in Ethanol for one hour. Afterwards, the sample gets rinsed with water and etched with 15 % HNO_3 for 10 minutes and ultrasonic cleansed subsequently.

2.2.2. Determination of IMC Growth Rate and Activation Energy

To measure the IMC thickness, six light microscope images were taken for each sample, except for the as-reflowed samples, where scanning electron microscopy images were required to examine the Cu_3Sn phase. The images were evenly distributed between the IMC layers on both sides of the solder joint. To calculate the thickness, the total areas of the IMC layers were measured using ImageJ as depicted in Fig. 19 and subsequently divided by the width of the IMC using formula 11.

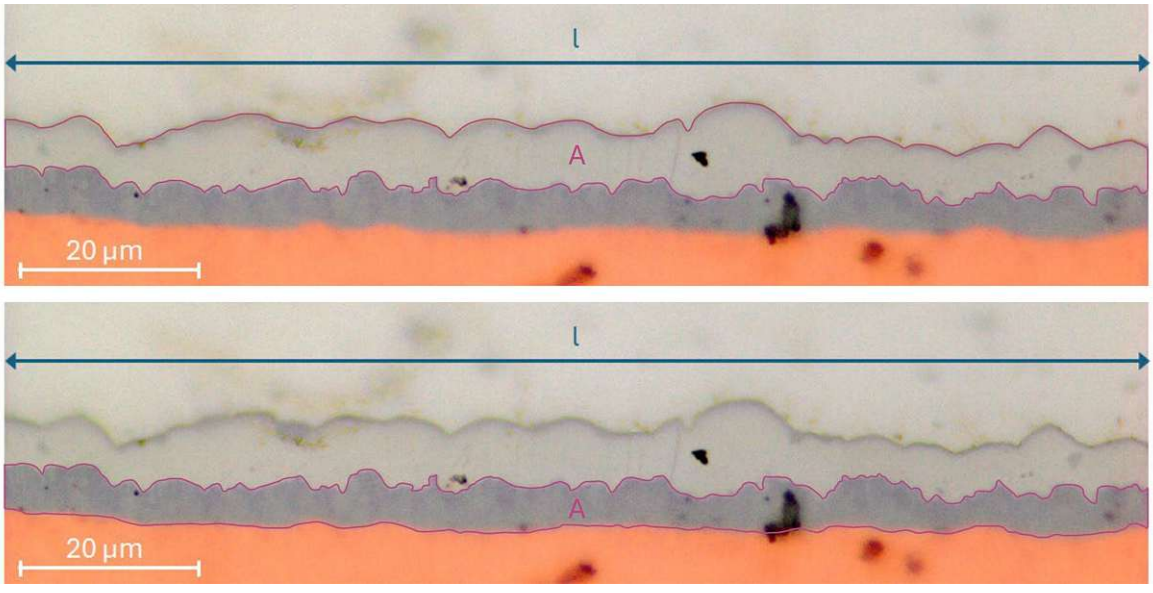

Figure 19: Example of the thickness calculation using ImageJ.

$$d = \frac{A}{l} \tag{11}$$

Assuming that the formation of IMC is a diffusion-controlled reaction, the diffusion coefficient D can be calculated using equation 12.

$$d = d_0 + (D \cdot t)^{1/2} \tag{12}$$

The IMC layer thickness d, in relation to the initial layer thickness d_0, exhibits parabolic growth over time t in theory. The layer thicknesses measured for the reflowed and aged samples at 120 °C or 180 °C for 20 days can be plotted as a function of the square root of time as shown in Fig. 20 (a). From this plot, a linear regression line can be established, and the slope of the line can be used to calculate the diffusion coefficient. The activation energies E_A and diffusion constants D_0 can be determined using the diffusion coefficients and the corresponding temperatures according to the Arrhenius equation 13.

$$D = D_0 \cdot e^{-\frac{E_A}{R \cdot T}} \tag{13}$$

For this purpose, the logarithm of the diffusion coefficients is plotted against the inverse absolute temperature T, and a linear regression line is created, from which the activation energy can be determined, as demonstarted in Fig. 20 (b). Here, R represents the universal gas constant.

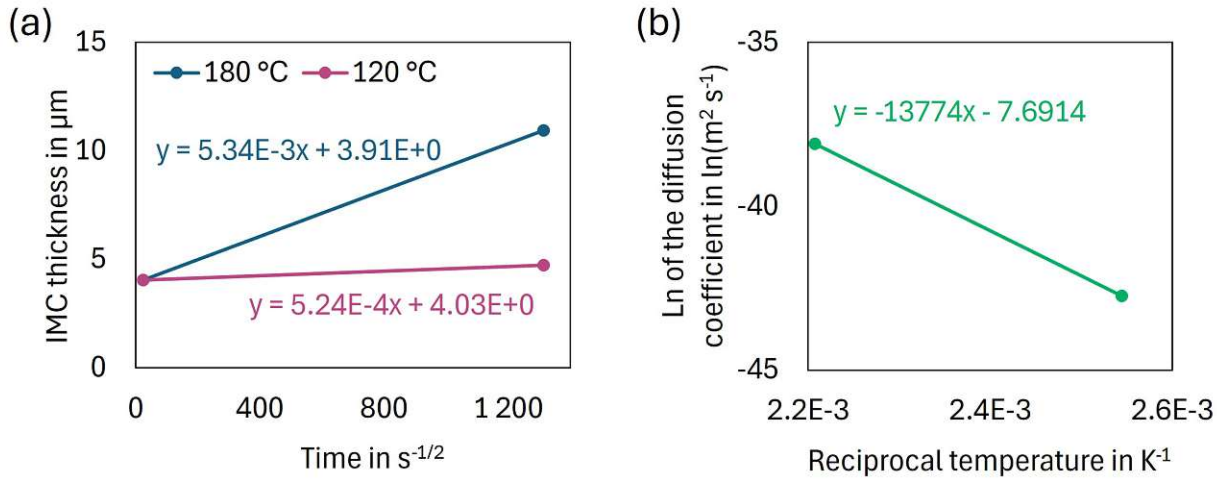

Figure 20: (a) The IMC thickness plotted against time for the diffusion coefficient calculations, and (b) the natural logarithm of the diffusion coefficient plotted against the reciprocal temperature for the activation energy calculations, shown here for a sample without cobalt nanoparticle additions.

2.2.3. Shear Testing

For shear testing a micro tensile machine form Messphysik Materials Testing GmbH depicted in Fig. 21 (c) was used. The push-off shear test was carried out at a speed of 1 mm min^{-1} and the shear strength was calculated by normalizing the maximum load before failure to the fracture area. An example of a load-extension curve (a) and the surface of a sample after shear testing (c) are depicted in Fig. 21.

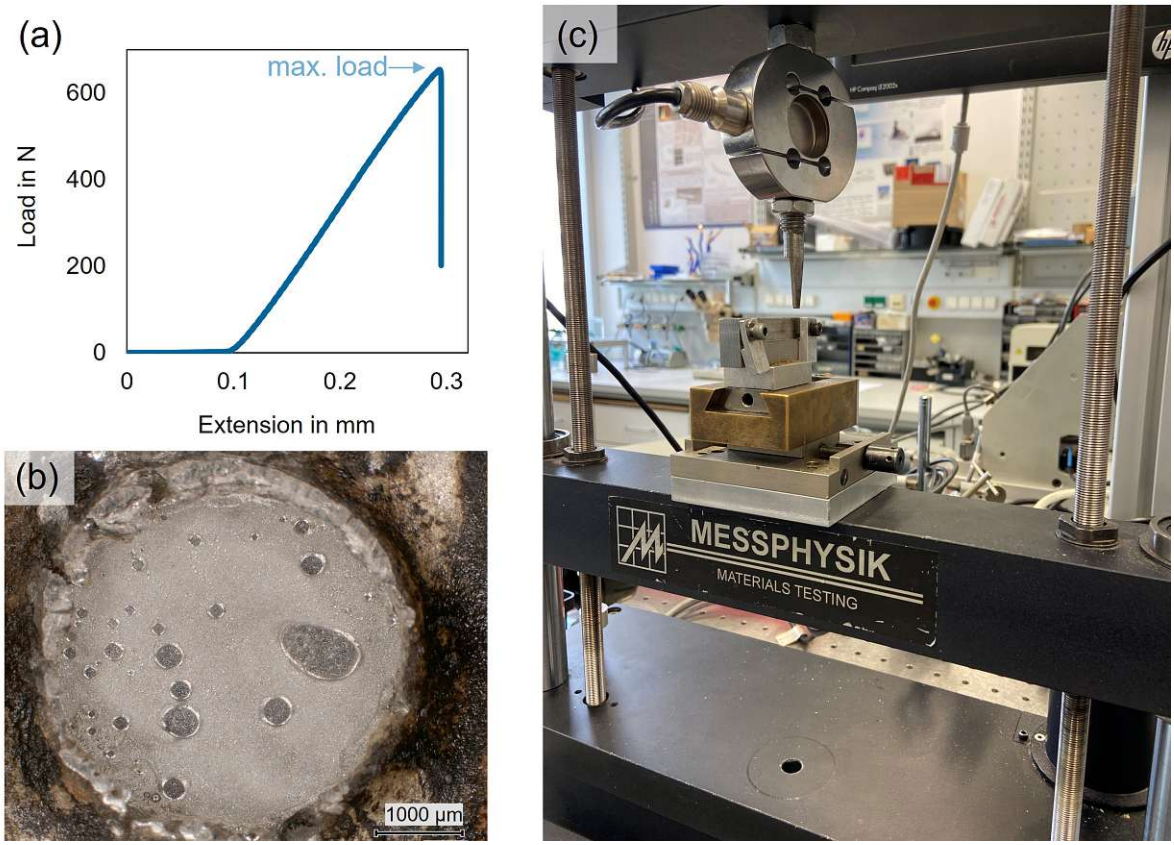

Figure 21: (a) Example load-extension curve, (b) surface of a sample after shear testing, (c) micro tensile machine form Messphysik Materials Testing GmbH.

2.2.4. Stress-Relaxation Testing

Before performing the stress-relaxation-test, the solder joints must be properly prepared. Therefore the excess solder is removed using a combination of grinding and sawing with a diamond wire. To precisely measure the solder gap, the surface of the solder joint is polished. Figure 22 shows the lap-shear joint, and a close-up of the solder joint during different progress steps (left), the untreated specimen after ageing is shown in 1, followed by 2 where the excess solder has already been removed, a further polished version is depicted in 3, subsequently 4 presents the joint after testing. The accurate dimensions of the lap-shear joint is provided in Fig. 23.

Figure 22: Progress of the solder joint preparation for the stress-relaxation-tests.

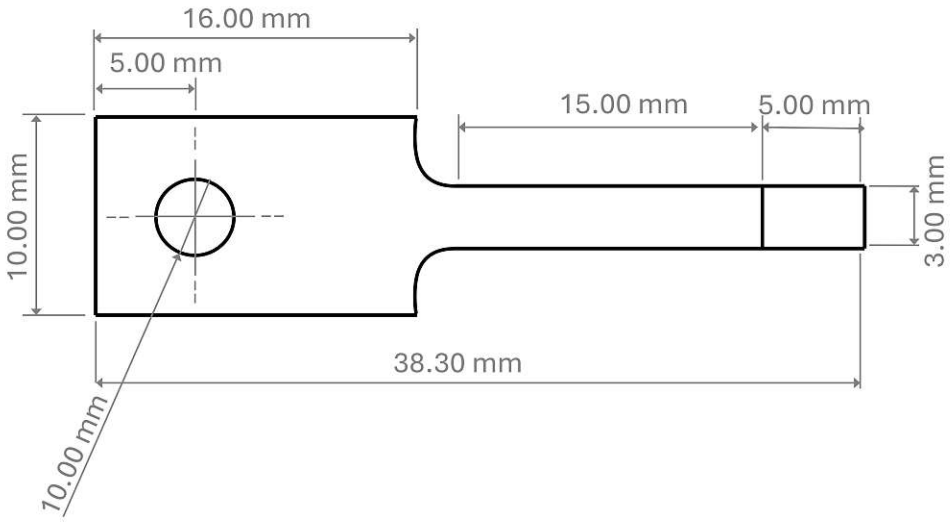

Figure 23: Dimensions of the lap-shear joint.

The prepared samples are mounted into another micro-tensile testing machine with a load capacity oof 1000 N and speed of 0.2 mm min^{-1} from Messphysik Materials Testing GmbH, equipped with a U2B load cell from Hottinger Brüel & Kjaer GmbH. For conducting the stress-relaxation tests, the specimen is elongated until a designated load is achieved. At this strain, the sample remains for one hour, and the decrease in the required load over time is observed. The change of load and strain over time during stress-relaxation-tests is shown in Fig: 24 (a). To determine the required load, preliminary tests where carried out which correspond to single joint shear tests. The recorded load over time of a sample pretest is depicted in 24 (b). The initial load for the stress relaxation tests is determined as 75 % of the average maximum load obtained from the preliminary tests. Three different test conditions were performed: room temperature (RT), 100 ° C, and 150 ° C.

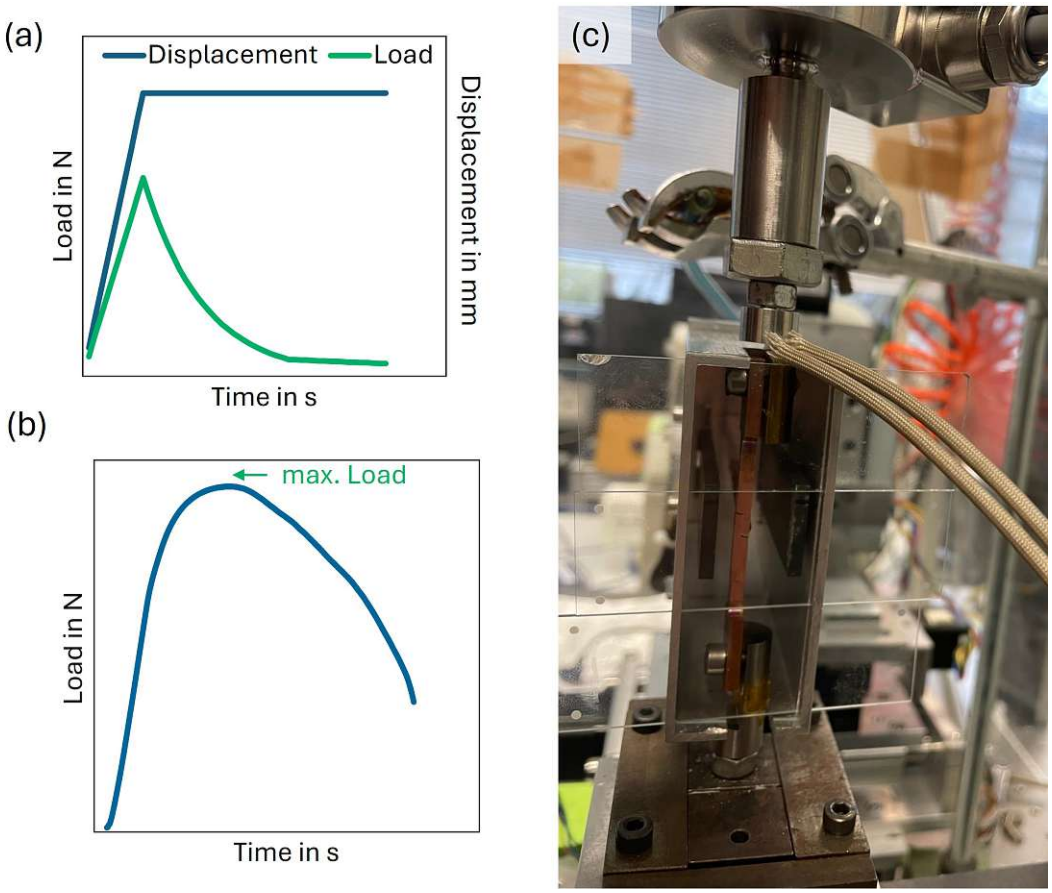

Figure 24: (a) Load and strain over time (b) pretest sample (c) stress-relaxation-test machine.

To compare stress-relaxation curves with distinct initial loads, which were necessary due to varying thermal treatments and strength, all curves are normalized to 100 %, which is illustrated in Fig. 25. Therefore, the load drop could be calculated by evaluating the difference between the stress after one hour and the initial stress.

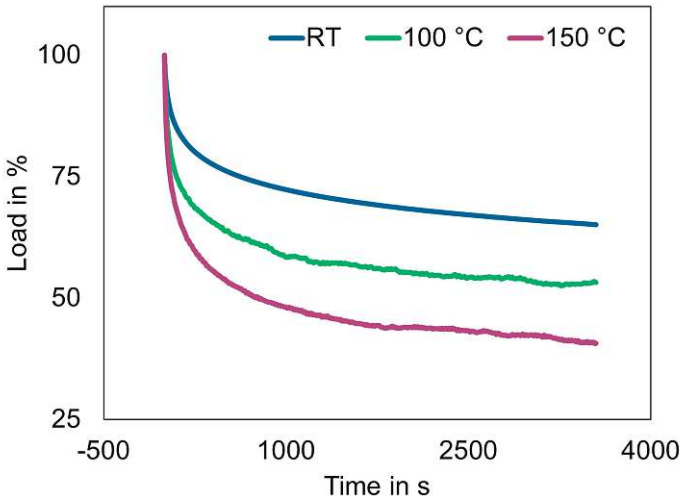

Figure 25: Sample normalized stress-relaxation curves.

To determine the stress exponent, the initial step is plotting stress as a function of time. The next is to average the data, for each type of sample up to five stress-relaxation curves were recorded. Then the stress gets differentiate by time and the derivation in MPa/s is plotted against the stress in MPa. After a logarithmic transformation of both axes, the slope of the linear regression can be measured, which corresponds to the stress exponent and is depicted in Fig. 26.

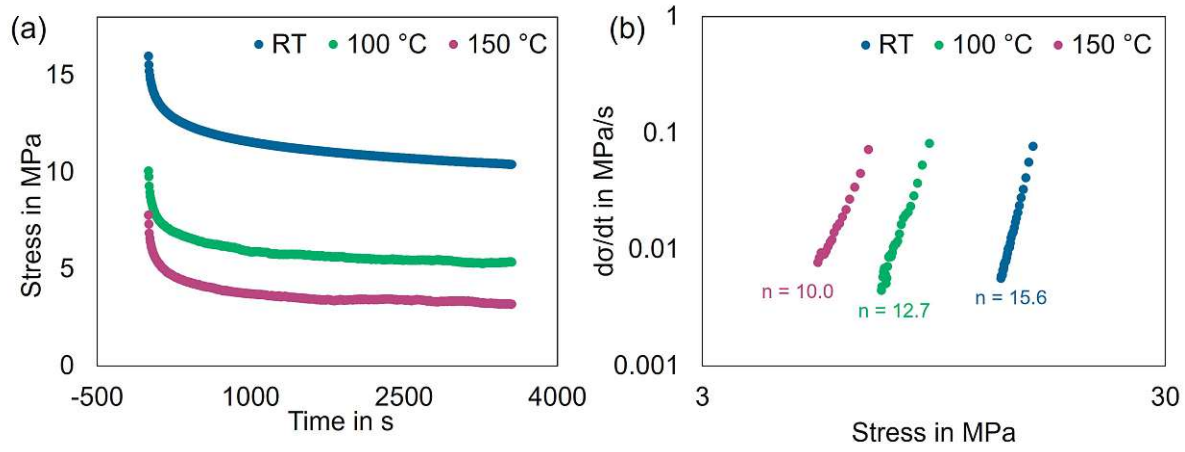

Figure 26: (a) Sample stress-relaxation curves (b) calculation of the stress exponent.

3. Results and Discussion

This chapter focuses on the analysis and discussion of the experimental findings. All the relevant data and detailed measurements are provided in the appendix.

3.1. Microstructure Analysis

A brief overview of the microstructure before and after ageing for 20 days at 180 °C is given in Fig. 27. The most significant difference can be seen between the aged and the as reflow samples. During thermal treatment the Cu_3Sn phase increases tenfold and the morphology of the Cu_6Sn_5 phase changes from scallop to a planar type. It is also noticeable that only very small Sn_3Ag precipitations can be seen in the solder of the as reflow samples, whereas they are clearly recognizable large ones in the solder and IMC of the aged samples. When comparing the as reflow IMCs with each other, it is evident that not only the size decreases with the addition of cobalt but also the morphology changes since there are less hills, which are further apart, and also more rounded. Looking at the aged SEM images no change of the IMC size can be seen with the naked eye and also no morphology change is noticeable. Other studies also report the change of the morphology from scallop type to planar type during ageing and the decrease of Cu_6Sn_5 growth with 0.10 % cobalt nanoparticle additions.[36]

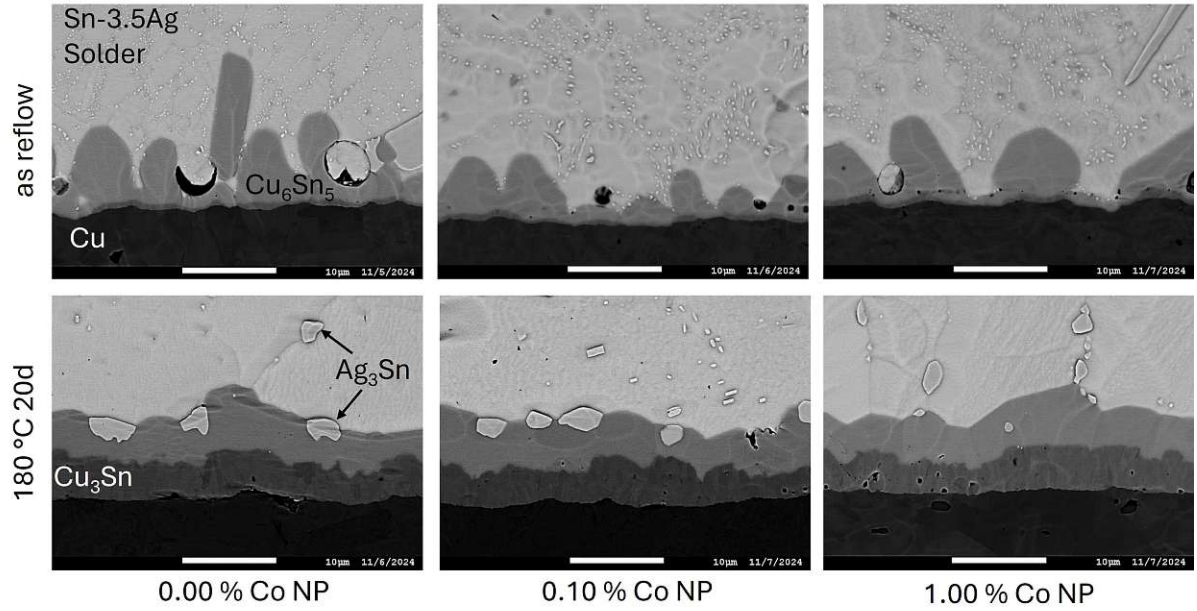

Figure 27: Microstructural overview at different cobalt nanoparticle concentrations in the as reflow state and after 20 days of ageing at 180 °C.

Figure 28 shows the microstructure changes for variating cobalt nanoparticle concentrations before and after ageing at 120 °C for 20 days. In the as reflow condition, light microscope images, the Cu_3Sn phase can barely be seen. However, an inhibited growth of Cu_6Sn_5 with 0.10 and 1.00 % Co NP additions is evident. The IMC morphology of

the Cu_6Sn_5 layer without additions is scallop type, which is typical and widely reported in literature.[37] With cobalt additions the morphology changes to a rather flat with a few with more distant humps. Further away bulges can be seen with 0.10 and 1.00 % Co NP additions compared to 0.25 and 0.50 %. After ageing for 20 days at 120 °C the Cu_3Sn phase is clearly detectable, but no differences can be seen with varying nanoparticle contents. The amount of Cu_6Sn_5 phase appears smallest with 0.10 and 1.00 % Co NP additions. However, the amount of total hills is quite similar with 0.00 to 0.50 %, even tough they are the smallest size at 0.10 %. The shape of the bulges is rather spike without additions compared to their round appearance with additions. Only a few hills can be seen with 1.00 % cobalt nanopowder additions, even tough they appear quite big. Comparing the microstructure before and after ageing, a significant increase of the Cu_3Sn phase is visible after the thermal treatment. However, the Cu_6Sn_5 layer appears only slightly bigger and the morphology changes to more evenly distributed bulges. In both cases the total IMC appeared smallest with 0.10 and 1.00 % Co NP additions.

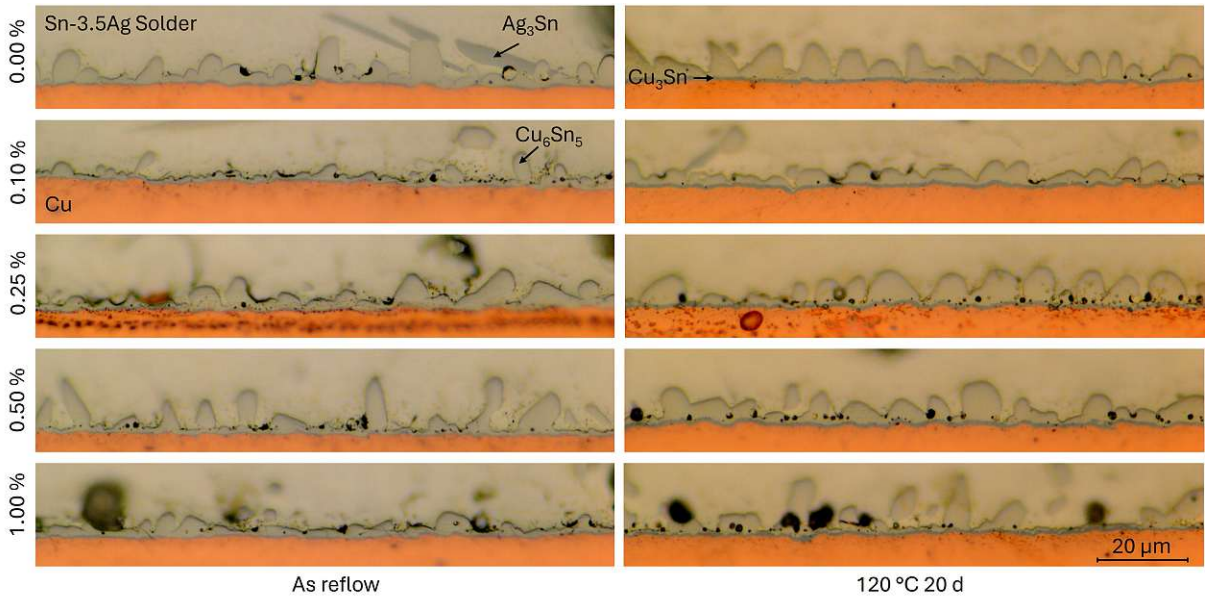

Figure 28: Microstructural overview at different cobalt nanoparticle concentrations in the as reflow state and after 20 days of ageing at 120 °C.

The thermal treatment at 180 °C for 10 and 20 days is compared in Fig. 29. After 10 days the Cu_3Sn phase is clearly visible but no difference is detectable with variating cobalt nanoparticle concentrations. Taking a look at Cu_6Sn_5 layer it is evident that it is the smallest with 0.10 % additions. Also the morphology of the phase is quite flat even tough there are still a few bigger bulges and without cobalt nanoparticles even some needle like structures can be seen. Focusing on the 20 days aged specimen, the Cu_3Sn phase exhibits a slight decline with 0.50 and 1.00 % cobalt nanopowder additions. The Cu_6Sn_5 layer appears still the smallest with only 0.10 %, but for all cobalt variations a quite similar planar shape can be seen. Noticeable is that for the first time a few Sn_3Ag precipitations can be seen in and on top of the IMC. Comparing the different ageing time, an increase in both Cu_3Sn and Cu_6Sn_5 phase formation can be seen with longer thermal treatment durations. The shape of the Cu_3Sn does not change, however the Cu_6Sn_5 layer

appears more planar with less bulges and also contains some visible Sn_3Ag precipitations. In both conditions, the total IMC was found to be smallest with the addition of 0.10 % and 1.00 % Co nanoparticles.

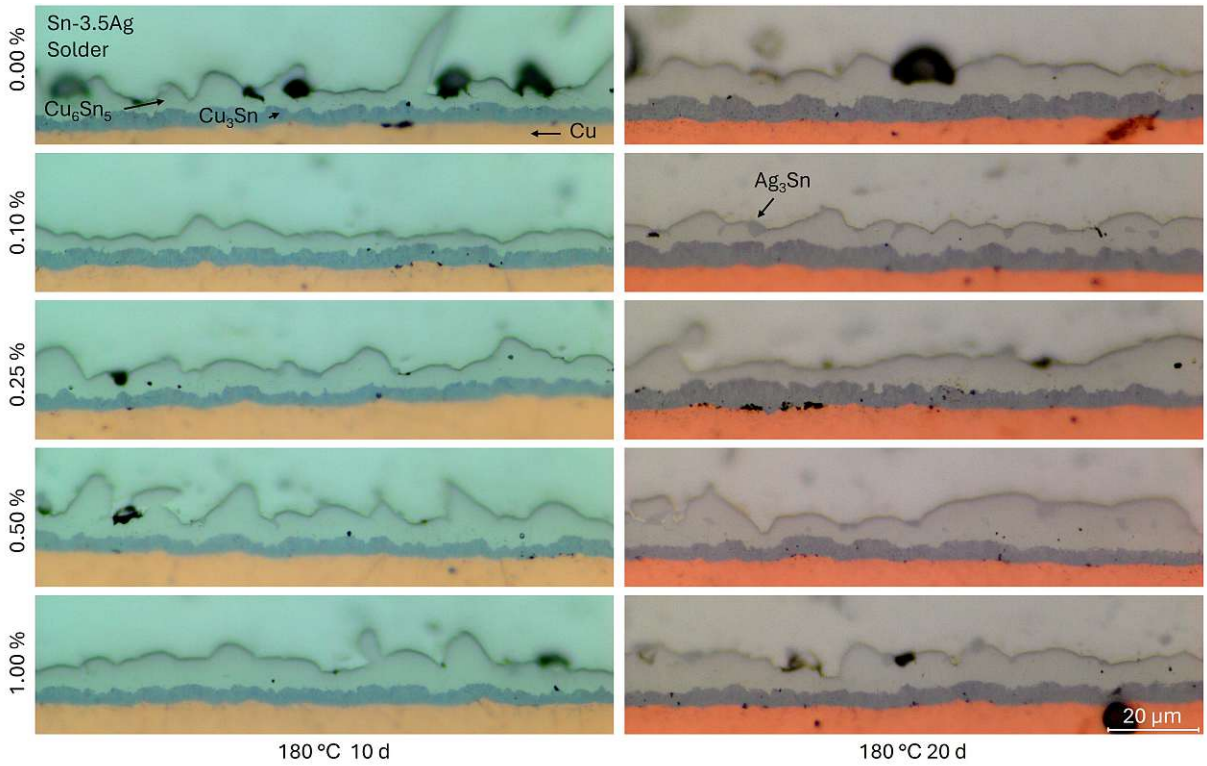

Figure 29: Microstructural overview at different cobalt nanoparticle concentrations after 10 and 20 days of ageing at 180 °C.

EDS mappings, of the solder and Cu_6Sn_5 phase with 0.10 % Co NP addition, which where recorded using transmission electron microcopy are depicted in Fig. 30. In the bright field image a Cu_6Sn_5 lamella can be seen surrounded by the Sn-3.5Ag solder containing a few Sn_3Ag precipitations. Comparing the Cu and Sn mapping the solder and IMC can be can be clearly distinguished and the Ag mapping also fits with the expected Sn_3Ag precipitations. Focusing on the Cobalt mapping a slight decrease can be seen within the IMC, however, due to the low amounts of cobalt, which may be under the detection limit, this pattern could also appear because of the close X-ray emission lines of cobalt and tin. The high-angle annular dark-field image also shows that nearly any cobalt could be measured and it also presents the Sn_3Ag composition well.

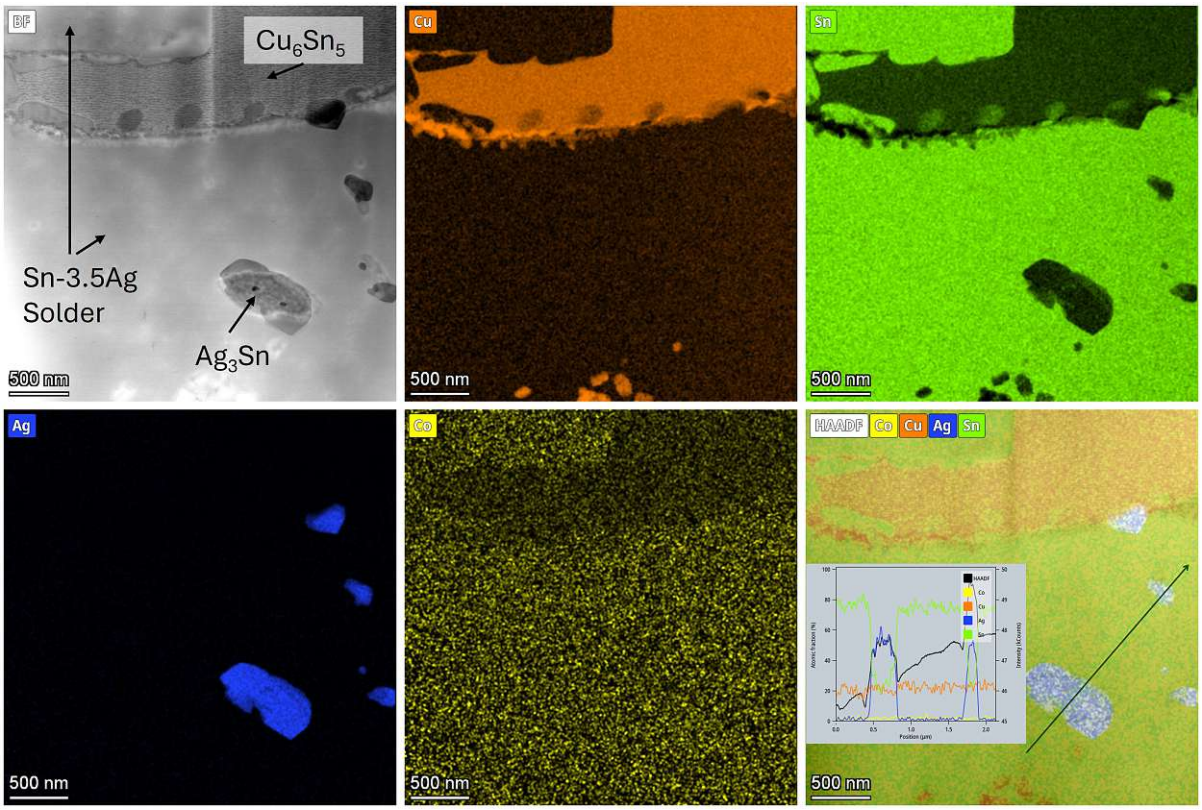

Figure 30: EDS mapping of the solder and Cu_6Sn_5 phase with 0.10 % Co NP additions recorded with TEM

Since nearly no free cobalt could be detected more mappings where done, in order to detect possible agglomerates. Two agglomerates with a size of about 200 nm could be found in the specimen with 1.00 % cobalt nanoparticle additions. These are presented in Fig. 31. In the samples with only 0.10 % no agglomerates where detected. Figure 30 and 31 were created and provided by Farzad Khodabakhshi.

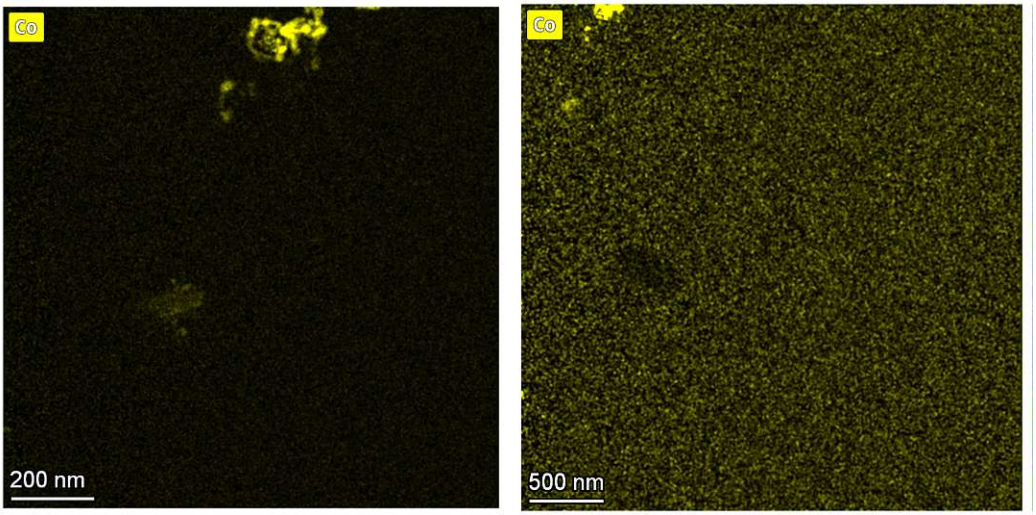

Figure 31: Cobalt mapping with agglomerates of specimen with 1.00 % cobalt nanoparticle additions.

Figure 32 depicts the samples after deep etching, giving a top look at the IMC, more specifically the Cu_6Sn_5 layer. Comparing the images it is apparent that with the addition of cobalt nanopowder, the hills on the surface become smaller and more uniform, on top oft that the number of Cu_6Sn_5 grains also increased. The morphology of the specimen without nanoparticles appears more sharper-edged. Huang et al. (2024)[19], reported the same behaviour of the Cu_6Sn_5 grain refinement with small amounts of cobalt additions, but also recorded grain coarsening with higher additions. Nasir Bashir et al. (2022)[38] suggests that the stronger thermodynamic affinity between Co and Sn, compared to Cu and Sn, promotes short range ordering between Co and Sn, leading to an increased nucleation rate and therefore smaller grain size. The study also proposes that the addition of cobalt suppresses the undercooling rate also leading to grain refinement.

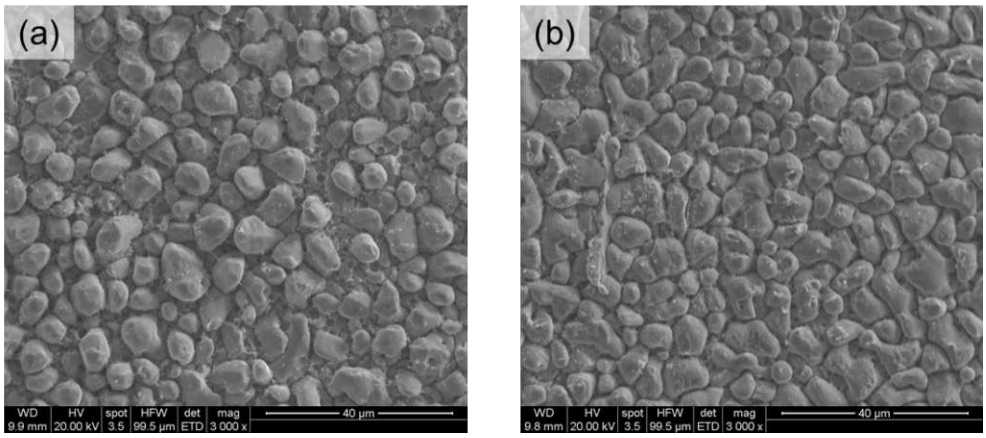

Figure 32: Deep etched samples with (a) 0 % Co NP and (b) 0.1 % Co NP.

3.2. IMC Thickness

The effect of cobalt nanoparticle content on the IMC growth is pictured in Fig. 33 for as reflow and 20 days at 120 °C aged specimen. Focusing on the as reflow samples no significant changes can be seen in the Cu_3Sn-phase. However, for the Cu_6Sn_5-phase the growth has been suppressed by a third with 0.10 % Co NP. With higher additions, the thickness increases again but remains lower than that of the sample without any additions. Other studies, like Sujan et al. (2013)[18] discovered the same trend. However they recorded a higher decrease which is about a half, this difference could be due to the different type and amount of flux used or variating soldering and testing conditions. Nonetheless, at 1.00 % cobalt nanoparticles, the thickness decreases, though not to the same extent as with 0.10 % Co NP. For the solder joints with the thermal treatment at 120 °C for 20 days, nearly the same trend is achieved with no significant change of the Cu_3Sn-phase, and the same decrease-increase-decease patter of the Cu_6Sn_5-phase can be seen, with a slightly lower increase at 0.10 % Co NP.

Comparing the as reflow and heat treated sample, the overall thickness of the IMC exhibits a slight increase after ageing at 120 °C as a result of the doubling the size of the Cu_3Sn-phase, with still no significant changes at different cobalt nanoparticle contents. In contrast, only minimal growth of about 0.4 μm can be detected in the Cu_6Sn_5-phase

across all Co nanoparticle variations. The exact values are shown in table 5, and the individual thickness measurements can be found in tables A16 and A17 in the appendix.

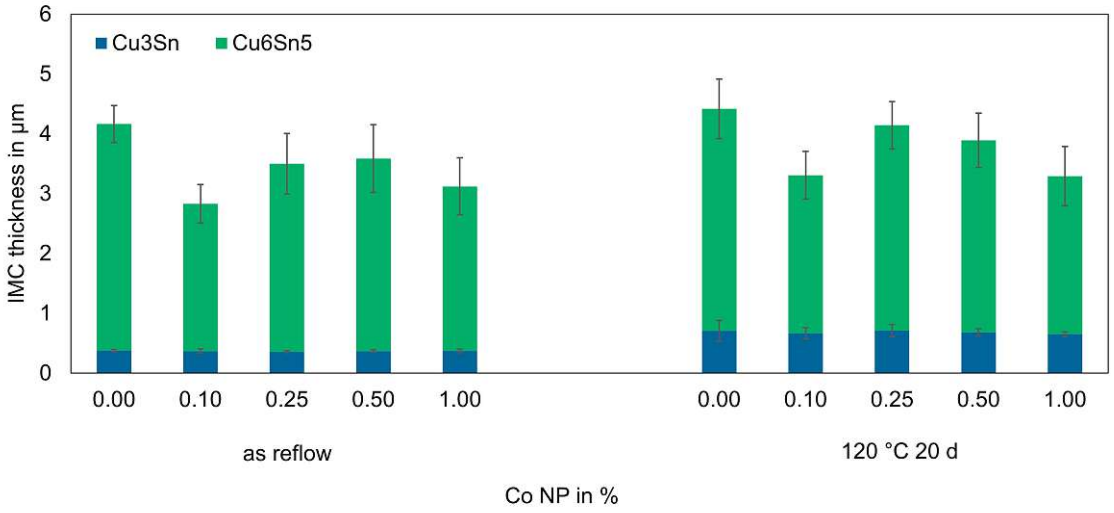

Figure 33: IMC thickness of as-reflowed samples and those aged at 120 °C for 20 days.

Thermal treatment	Co NP	IMC thickness in μm Cu $_3$Sn	Cu $_6$Sn $_5$	total IMC
As reflow	0.00 %	0.38 ∓ 0.02	3.66 ∓ 0.31	4.04 ∓ 0.31
	0.10 %	0.37 ∓ 0.04	2.34 ∓ 0.32	2.71 ∓ 0.32
	0.25 %	0.36 ∓ 0.02	3.02 ∓ 0.50	3.38 ∓ 0.50
	0.50 %	0.37 ∓ 0.02	3.02 ∓ 0.56	3.39 ∓ 0.56
	1.00 %	0.37 ∓ 0.03	2.81 ∓ 0.48	3.18 ∓ 0.48
120 °C 20 d	0.00 %	0.71 ∓ 0.17	4.01 ∓ 0.50	4.72 ∓ 0.54
	0.10 %	0.67 ∓ 0.09	2.77 ∓ 0.40	3.44 ∓ 0.32
	0.25 %	0.71 ∓ 0.10	3.43 ∓ 0.40	4.15 ∓ 0.48
	0.50 %	0.68 ∓ 0.06	3.42 ∓ 0.45	4.10 ∓ 0.44
	1.00 %	0.65 ∓ 0.04	3.20 ∓ 0.50	3.85 ∓ 0.47

Table 5: IMC thickness values with variating amounts of Co NP additions in as reflow condition and aged for 20 day at 120 °C

The influence of thermal ageing at 180 °C for 10 and 20 days is presented in Fig. 34. For comparison, the previously discussed as-reflow values are also included. Following 10 days at 180 °C, a slightly different behaviour in the IMC thickness is observed compared to the as-reflow condition. The Cu_3Sn-phase thickness is not constant any more but decreases slightly, with a greater decline, at higher cobalt nanoparticle additions. A difference of about 0.4 μm is observed between the highest and lowest values, at 0.00 % and 1.00 % Co NP content. Changes can also be seen in the previously observed decrease-increase-decease pattern of the Cu_6Sn_5-phase. The first decrease with 0.10 % cobalt nanopowder stays quite the same even tough it is now only reduced by a quarter.

The following increase exceeds earlier observations, with 0.50 and 1.00 % Co NP additions nearly reaching the thickness of the Cu_6Sn_5-phase of the samples with no nanoparticle additions. Furthermore, no decrease is visible at higher concentrations.

Extending the ageing time to 20 days at 180 °C results in similar behaviour as seen after 10 days. The slight decrease of the Cu_3Sn-phase is still present, tough weaker, with a maximum deviation of 0.2 μm. The decrease of the Cu_6Sn_5-phase with 0.10 % cobalt nanopowder additions, is even further reduced to about a fifth. Contrary to before, the following rise does not exceed the IMC thickness without additions. A comparison of Cu_3Sn growth across different thermal treatments reveals a nearly tenfold increase from the as-reflow condition to 10 days of ageing at 180 °C, followed by an additional increase of about 25 % after 20 days. An increase of about half the Cu_6Sn_5-phase is also clearly visible after 10 days followed by another third after 20 days. Detailed values are presented in table 6, with corresponding individual thickness measurements available in tables A16, A18 and A19 in the appendix.

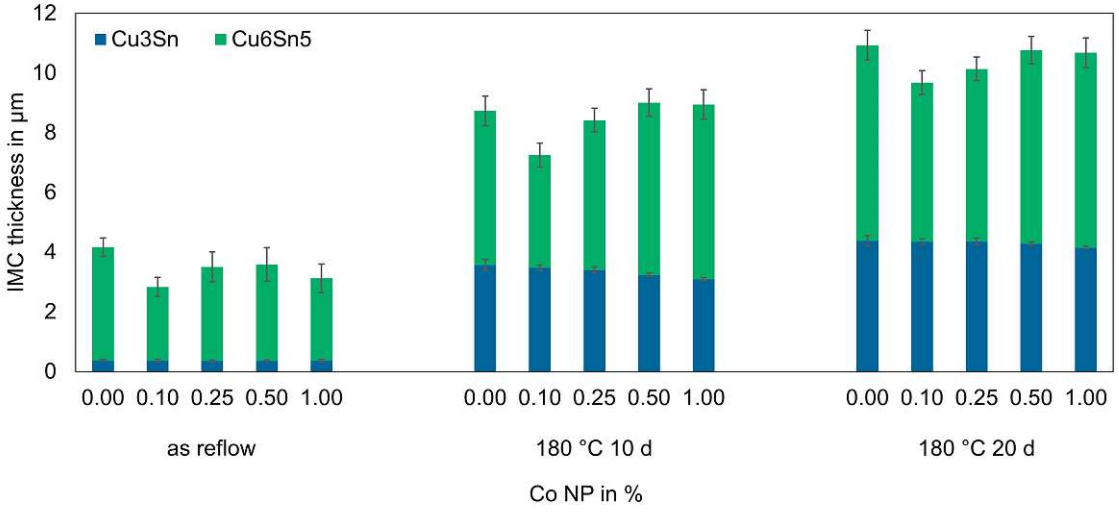

Figure 34: IMC thickness of as-reflowed samples and those aged at 180 °C for 10 and 20 days.

Thermal treatment	Co NP	IMC thickness in μm		
		Cu $_3$Sn	Cu $_6$Sn $_5$	total IMC
As reflow	0.00 %	0.38 ∓ 0.02	3.66 ∓ 0.31	4.04 ∓ 0.31
	0.10 %	0.37 ∓ 0.04	2.34 ∓ 0.32	2.71 ∓ 0.32
	0.25 %	0.36 ∓ 0.02	3.02 ∓ 0.50	3.38 ∓ 0.50
	0.50 %	0.37 ∓ 0.02	3.02 ∓ 0.56	3.39 ∓ 0.56
	1.00 %	0.37 ∓ 0.03	2.81 ∓ 0.48	3.18 ∓ 0.48
180 °C 10 d	0.00 %	3.51 ∓ 0.13	5.15 ∓ 0.45	8.66 ∓ 0.54
	0.10 %	3.48 ∓ 0.05	3.77 ∓ 0.26	7.25 ∓ 0.27
	0.25 %	3.41 ∓ 0.11	5.01 ∓ 0.58	8.42 ∓ 0.52
	0.50 %	3.24 ∓ 0.13	5.76 ∓ 0.96	9.01 ∓ 0.91
	1.00 %	3.10 ∓ 0.15	5.84 ∓ 0.83	8.94 ∓ 0.89
180 °C 20 d	0.00 %	4.39 ∓ 0.15	6.54 ∓ 0.41	10.93 ∓ 0.50
	0.10 %	4.35 ∓ 0.06	5.32 ∓ 0.74	9.68 ∓ 0.75
	0.25 %	4.37 ∓ 0.23	5.77 ∓ 0.58	10.14 ∓ 0.60
	0.50 %	4.28 ∓ 0.18	6.48 ∓ 0.36	10.77 ∓ 0.43
	1.00 %	4.15 ∓ 0.11	6.52 ∓ 0.51	10.68 ∓ 0.46

Table 6: IMC thickness values with variating amounts of Co NP additions in as reflow condition and aged for 10 and 20 day at 180 °C

The effect of the inhibition of the IMC growth with the addition of cobalt NP in the Cu_6Sn_5-phase, supports the findings in the literature that during reactive dissolution the Co forms the complex compound $(Cu,Co)_6Sn_5$.[7] According to literature a possible reason behind the rising growth at higher cobalt contents may be that more nanoparticles get dissolved into the solder which also increases the copper consumption leading to a thicker IMC.[18] On the other hand the enhancement of the growth at higher cobalt concentrations could potentially be explained through segregation and aggregation of the NP, as shown in Fig. 31, leading to less available particles during reactive dissolution.

Given that the proportions of the IMC thickness remain relatively constant throughout ageing, it is also quite intriguing to examine the parabolic growth of IMC thickness as presented in Fig. 35. However, it should also be noted that the thermally treated samples are not identical to the reflow samples that were subsequently aged, but were independently fabricated and the measured thickness also shows a non negligible standard deviation. Observation of the total IMC in (c) indicates that an increase in cobalt content correlates with an accelerated growth of the total IMC. The same results are obtained in (b) for the Cu_6Sn_5-layer. Contrary the Cu_3Sn-layer in (a) shows exactly the opposite behaviour with an accelerated growth at lower cobalt concentrations. Haseeb et al. (2017)[6] observed the same trends.

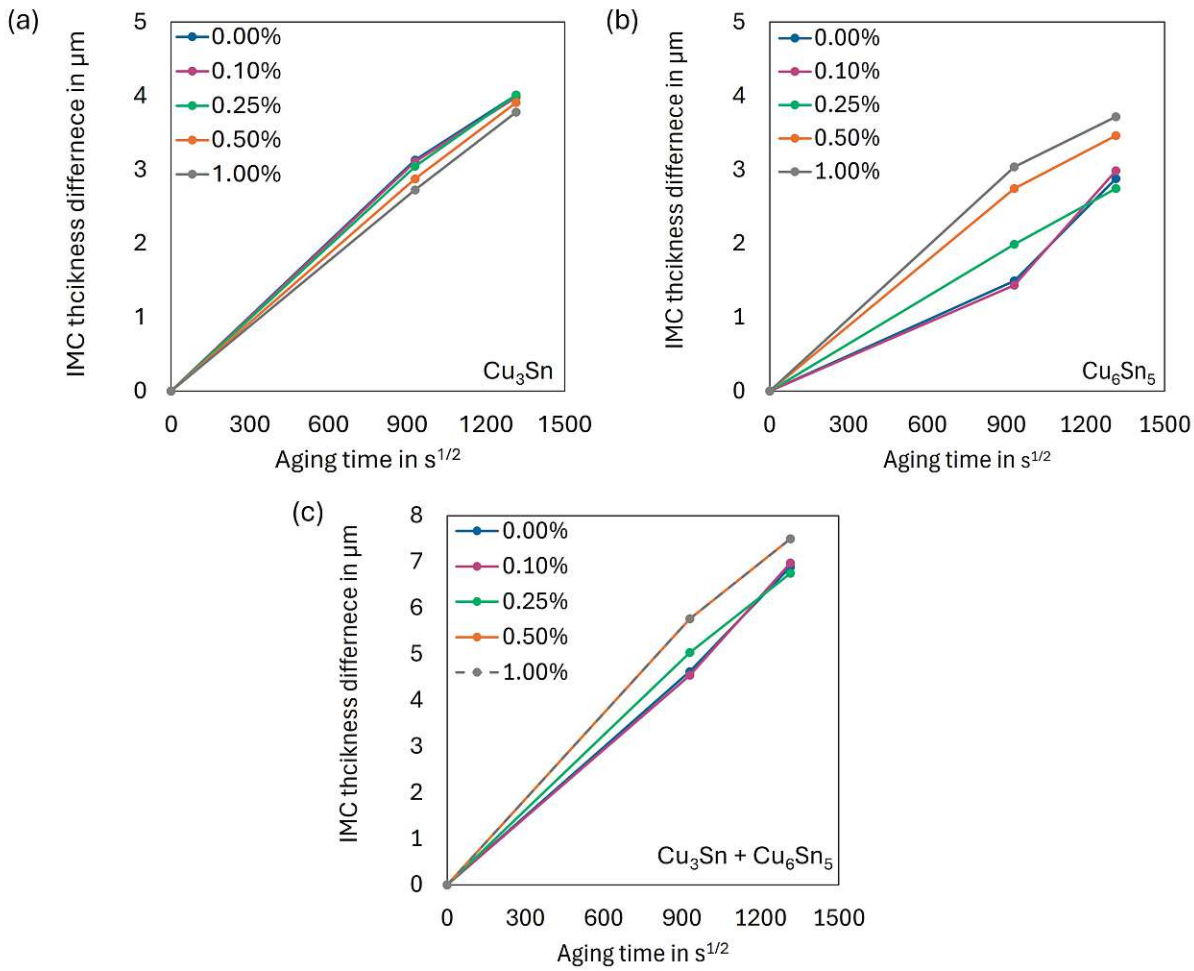

Figure 35: IMC thickness change during ageing at 180 °C for the (a) Cu_3Sn-layer, (b) Cu_6Sn_5-layer and (c) total IMC.

3.2.1. Determination of Activation Energy

To gain further insights into the growth behaviour, the diffusion coefficients and activation energies were calculated and are illustrated in Fig. 36, the calculated slopes can be found in the appendix in the tables A21, A20 and A22. Taking a closer look at the diffusion coefficients in table 7 it can be seen that the Cu_6Sn_5-layer and the total IMC generally tended to slightly increase with the addition of cobalt NP. An elevated diffusion coefficient implies quicker particle movement and accelerated IMC growth, aligning well with Fig. 35 (b) and (c), which demonstrate a greater IMC thickness increase when cobalt nanoparticles are introduced. In contrast, the diffusion coefficient of the Cu_3Sn-layer tends to decrease marginal which also fits with the behaviour in Fig. 35 (a). When analysing the diffusion coefficients at 120 °C and 180 °C in Fig. 36 (a) and (b), it is evident that an increase in temperature leads to an enhanced diffusion coefficient. Very interesting is also that at 120 °C the Cu_6Sn_5-layer has the higher diffusion coefficient, however, at 180 °C the Cu_3Sn-layer has the higher diffusion. Which means that at higher temperatures the growth of the Cu_3Sn-layer gets promoted.

The activation energy of Cu_3Sn tends to rises with the addition of cobalt nanopowder, this means more energy is necessary to form it thus it grows slower. This fits well with the lower diffusion coefficients with cobalt addition. For the Cu_6Sn_5-layer and total IMC the expectations where not fulfilled. Following the higher diffusion coefficients with the addition of cobalt, a lower activation energy was expected, but no clear trend could be identified. A possible reason for this behaviour could be the different starting intermetallic compound thicknesses. Since the parabolic growth behaviour inhibits the growth of thicker IMCs which means more time and energy is necessary, to reach the same thickness increase, than it would be with a thin layer. Thus, a lower activation energy is reasonable for thinner IMCs such as with 0.10 and 0.25 % cobalt nanopowder. Mouratidis et al. (2014)[39], also suggests that with an increasing joint thickness the activation energy increases. When looking at the difference between the activation energy of the IMC layers in general it can be seen that the Cu_3Sn has an higher activation energy and therefore needs more energy to form and grows slower.

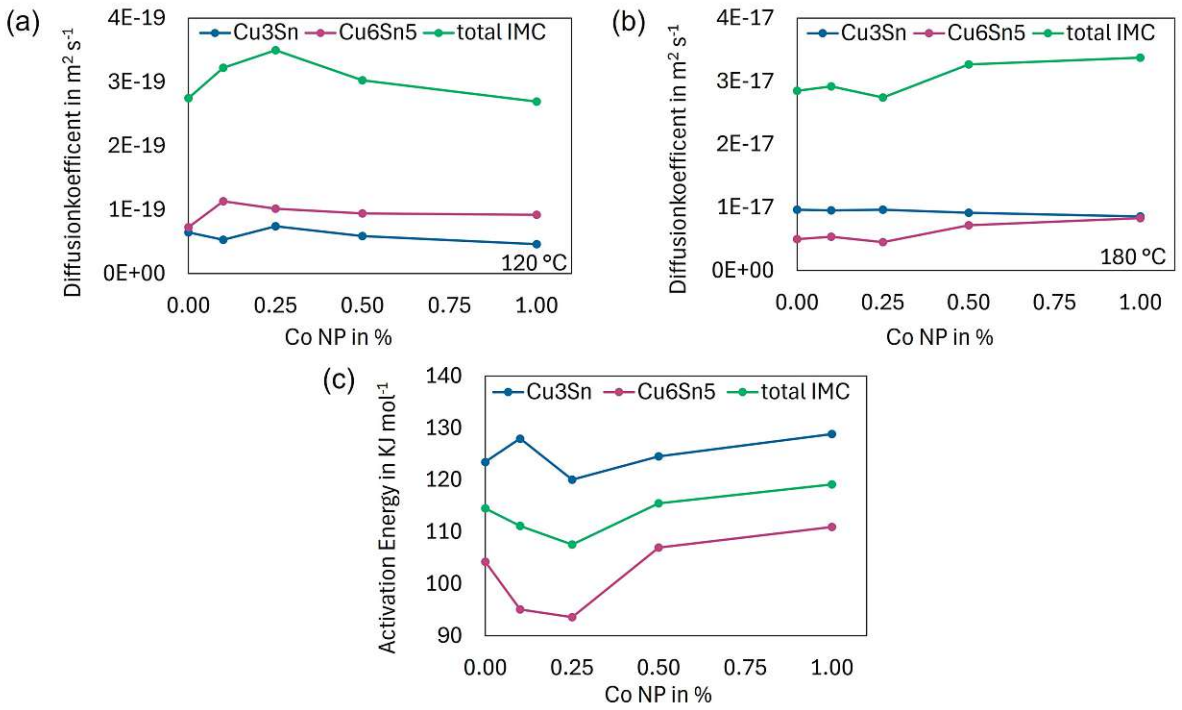

Figure 36: Cobalt NP content against (a) the diffusion coefficient at 120 °C and (b) 180 °C (c) and the activation energy.

Table 7: Diffusion coefficients at 120 and 180 °C.

		Diffusion coefficient in m^2 s^{-1}		
Temperatur	**Co NP**	**Cu3Sn**	**Cu6Sn5**	**total IMC**
120 °C	0.00 %	6.47E-20	7.27E-20	2.75E-19
	0.10 %	5.33E-20	1.14E-19	3.23E-19
	0.25 %	7.44E-20	1.02E-19	3.50E-19
	0.50 %	5.91E-20	9.44E-20	3.03E-19
	1.00 %	4.63E-20	9.25E-20	2.70E-19
180 °C	0.00 %	9.65E-18	3.79E-18	2.85E-17
	0.10 %	9.53E-18	5.36E-18	2.92E-17
	0.25 %	9.66E-18	6.34E-18	3.10E-17
	0.50 %	9.19E-18	7.21E-18	3.38E-17
	1.00 %	8.58E-18	3.80E-18	3.38E-17

Table 8: Activation energy at different cobalt NP contents.

	Activation energy in kJ mol^{-1}		
Co NP	**Cu_3Sn**	**Cu_6Sn_5**	**total IMC**
0.00 %	123.5	104.3	114.5
0.10 %	127.9	95.1	111.1
0.25 %	120.1	93.6	107.6
0.50 %	124.5	107.0	115.5
1.00 %	128.9	110.9	119.2

Table 9 shows activation energies reported in literature. Comparing the measured values with the ones achieved from Haseeb et al. (2010)[40], it is evident that the absolute activation energy received in this study is about 40 kJ mol^{-1} higher. However the general trend agrees, with the highest activation energy for the Cu_3Sn phase followed by the total IMC. Since paste mixing was used, the cobalt content can not be directly compared, assuming that the most suitable concentration has been used, it is reasonable to compare it with 0.10 %, assuming that demonstrated the best properties in this study. In both cases the activation energy for the Cu_6Sn_5-phase and the total IMC decrease and increases for the Cu_3Sn-phase, with the addition of cobalt. Since the values differed significantly, additional studies were consulted, and Mayappan et al. (2022)[41] was found, where the values were much more consistent and the overall trend remained the same.

Table 9: Reported activation energy values in the literature

		Activation energy in kJ mol^{-1}		
Reference	Solder	**Cu_3Sn**	**Cu_6Sn_5**	**total IMC**
Haseeb et al. (2010)[40]	SAC	80.69	52.27	77.70
	SAC + 0.75 % CO	94.73	33.32	40.55
Mayappan et al. (2022)[41]	SAC	102.10	97.86	-

3.3. Shear Testing Results

To develop an understanding of the mechanical properties of solder joints shear tests where conducted with samples undergoing different thermal treatments and various cobalt nanoparticle contents. The evaluated shear strength is presented in Fig. 37 with the corresponding values in table 10 and the results of the individual measurements in tables A23 and A24 in the appendix. Focusing on the as reflow specimen an increase in shear strength about 13 % can be seen with the addition of 0.10 and 0.25 % Co NP compared to no additions. However, with further additions a decline can be seen. More specifically including 0.50 % Co NP lead to no significant change whereas the shear strength even worsened at 1 % compared to no additions. Lee et al. (2008) [22] achieved the same trend, an increase at low addition levels, followed by a decrease at higher addition levels. However, they reached double the increase compared to this study, with a rise of 28 %, reasons for these differences may include the varying techniques used to incorporate the nanoparticles, as well as the different sample type, since they used ball shear test samples.

Literature suggests that a possible reasons for the increase of shear strength with small additions is the grain refinement of the Cu_6Sn_5 phase, which could be seen in Fig. 32. The decrease with further additions could be explained by the agglomeration and segregation of cobalt, shown in Fig. 31, which results in a disrupted matrix leading to higher internal stress. Therefore, the solder joint is more prone to failure under external stress.[19]

After ageing for 20 days at 120 °C a different trend is visible, with 0.10 % Co NP the shear strength decreases about 5 %, contrary to expectations. However, at 0.25 % the shear strength rises and is about 6 % higher than without nanoparticles. The renewed decrease at 0.50 and 1.00 % is in accordance with the behaviour at as reflow conditions. After 20 days at 180 °C the highest rise in shear strength is visible at 0.1 % cobalt nanopowder with about 15 % compared to no additions, but even tough the shear strength is still higher with 0.25 % the increase is only about 7 %. Higher additions, 0.50 and 1.00 % again lead to nearly no strength increase.

Comparing the different thermal treatments, the highest shear strength was reached testing the as reflow samples. A decline about 23 % and 20 % was observed after ageing for 20 days at 120 and 180 °C. Interesting is that the shear strength does not differ a lot between the 120 and 180 °C treatment, even tough the IMC thickness is twice as big at 180 °C. Chen et al. (2006)[42] also reports a decrease in shear strength after thermal ageing. As a reason for this behaviour, it is suggested that the Sn_3Ag precipitations coarsen and that the particle density also decreased trough agglomeration leading to a generally weaker particle strengthening effect after thermal treatment, which could be the reason why similar shear strength was achieved with both thermal treatment. However Poon et al. (2000)[43] states that with an increase of the Cu_6Sn_5-layer, which happens during thermal ageing, the ductility decreases and thereby acts as an crack imitation site.

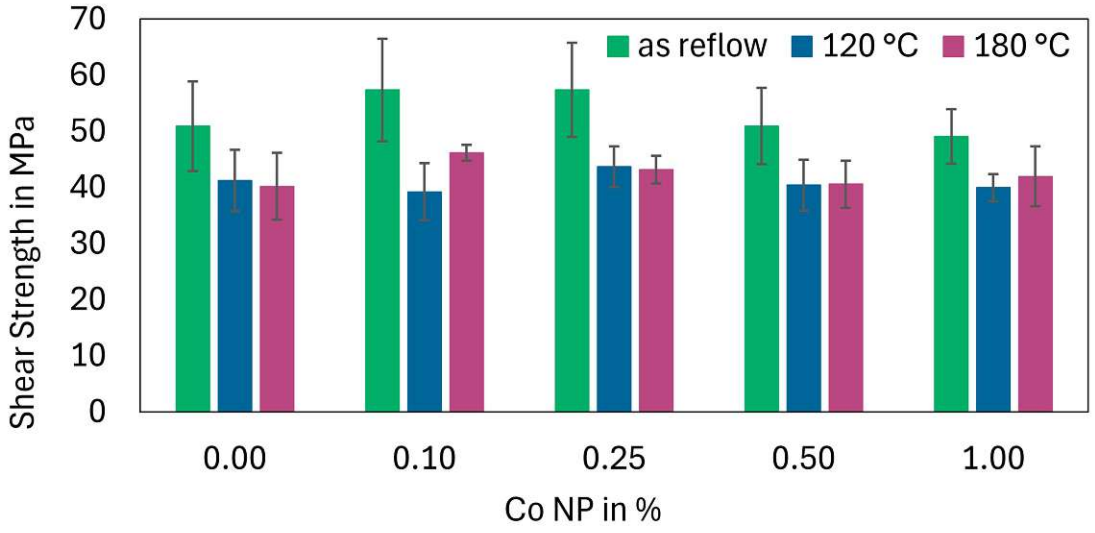

Figure 37: Shear strength of the solder joints with different cobalt NP contents and thermal treatments obtained by using push-off samples.

Thermal treatment	Shear strength in MPa 0.00 %	0.10 %	0.25 %	0.50 %	1.00 %
as reflow	51 ∓ 8	57 ∓ 9	57 ∓ 8	51 ∓ 7	49 ∓ 5
120 °C 20 d	41 ∓ 5	39 ∓ 5	44 ∓ 4	40 ∓ 5	40 ∓ 2
180 °C 20 d	40 ∓ 6	46 ∓1	43 ∓ 2	41 ∓ 4	42 ∓ 5

Table 10: Shear strength at various cobalt NP contents and thermal treatments.

The fracture surfaces of specimen with 0.00 and 0.10 % cobalt nanoparticle additions, before an after ageing at 180 °C for 20 days, are depicted in Fig. 38 and 39. Focusing on the as reflow condition in Fig. 38, a quasi-brittle failure mode can be seen with both 0.00 and 0.10 %. The main part of the fracture consists of brittle IMC, with only about 10 % ductile fracture in the solder. In (c) and (d), a close-up of the ductile honeycomb fracture can be seen, while (e) and (f) show the brittle IMC with some areas of transcrystalline fracture in the Cu_6Sn_5 phase. In general, no difference can be observed on the fracture surface with or without cobalt nanoparticle additions. After ageing at 180 °C for 20 days depicted in Fig. 39, the same quasi-brittle failure mode, with about the same amounts of brittle and ductile fracture, can be seen. The close up of the ductile zone in (c) and (d) reveals no difference with varying cobalt additions. However, compared to the as reflowed condition, the honeycombs appear less deep and more evenly distributed. In the brittle zones shown in (e) and (f), the transcrystalline fracture in the Cu_6Sn_5 phase is visible again and even appears more pronounced. In general, it can be said that the fracture mode does not change with the addition of nanoparticles, and only slight changes can be observed after thermal treatment

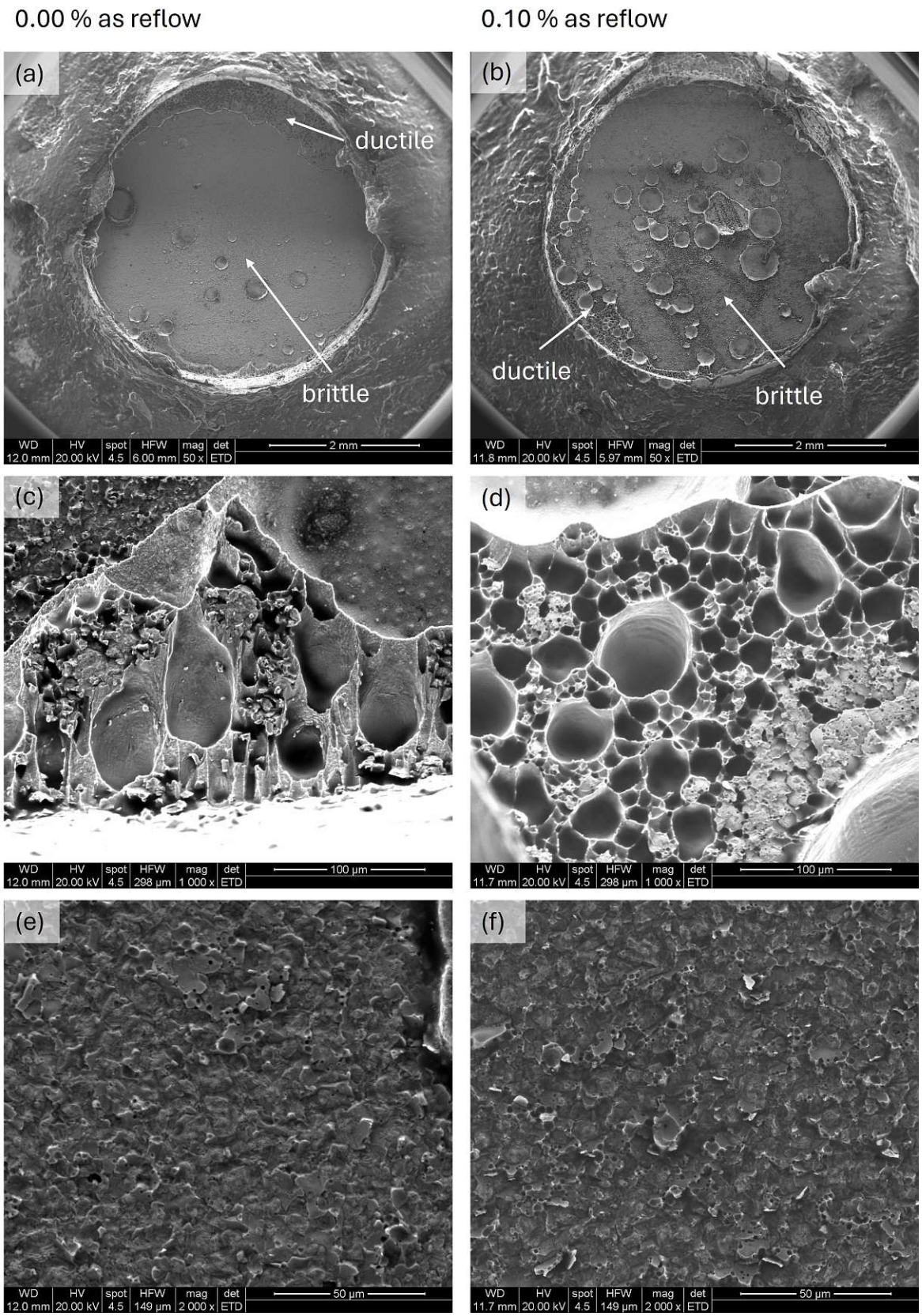

Figure 38: Fracture surfaces of samples in the as-reflowed condition with 0.00 % Co NPs: (a) overview, (b) ductile zone, (c) brittle zone; and with 0.10 % Co NPs: (d) overview, (e) ductile zone, (f) brittle zone.

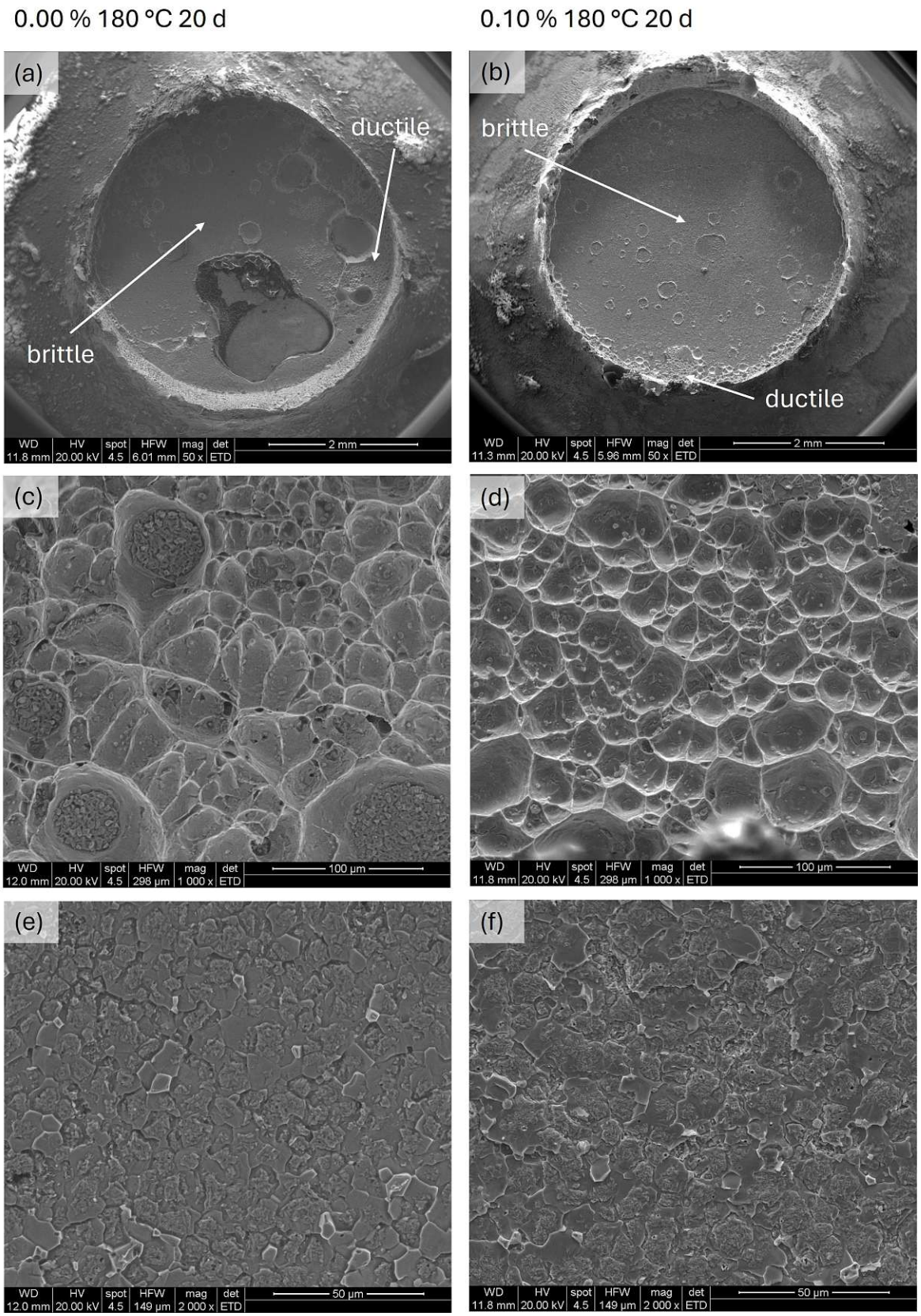

Figure 39: Fracture surfaces of samples after ageing for 20 days at 180 °C with 0.00 % Co NPs: (a) overview, (b) ductile zone, (c) brittle zone; and with 0.10 % Co NPs: (d) overview, (e) ductile zone, (f) brittle zone.

3.4. Stress-Relaxation Behaviour

Whenever the term 'aged' is used in the next chapter, it specifically refers to samples exposed to 180 °C for 20 days.

3.4.1. Pretests and Shear Strength

In order to determine the initial load for the stress relaxation tests, pretests were conducted in which the shear stress was recorded. For each sample type one to two pretest where carried out, the results and the calculated starting load is shown in table 11. However, it is also important to note that, in general, a higher staring load is expected to result in a greater stress drop.[44]

Table 11: Results of the pretests and calculated starting load for the SRT.

Temperature treatment	Testing temperature	Co NP	Load in N Average	SRT start
as reflow	RT	0.00%	349	275
		0.01%	410 ∓ 9	300
		0.25%	372 ∓ 8	290
		1.00%	354 ∓ 24	275
	100 °C	0.00%	222 ∓ 18	170
		0.01%	204 ∓ 8	160
		0.25%	183 ∓ 11	150
		1.00%	209 ∓ 2	160
	150 °C	0.00%	139	80
		0.01%	175 ∓ 3	130
		0.25%	115 ∓ 26	100
		1.00%	149 ∓ 7	115
180 °C 20 d	RT	0.00%	230	175
		0.01%	258 ∓ 8	200
		0.25%	260 ∓ 10	200
		1.00%	257 ∓ 20	195
	100 °C	0.00%	140	100
		0.01%	153 ∓ 4	115
		0.25%	154 ∓ 14	115
		1.00%	130 ∓ 15	95
	150 °C	0.00%	99	75
		0.01%	122∓ 21	90
		0.25%	98 ∓ 10	70
		1.00%	96 ∓ 4	70

Figure 40 illustrates the shear stress results obtained from pretests and shear tests conducted with varying concentrations of cobalt nanoparticles, different thermal treatments,

and diverse testing temperatures. The trend of achieving higher shear strength with low concentrations of cobalt nanoparticles, which was already observed in the push-off shear tests, continues. When comparing the different thermal treatments it can be observed that the increase in shear strength, with cobalt addition is higher for the as reflow samples, and that shear strength in general is also higher compared to the 20 days aged samples. When evaluating the different testing temperatures it is visible that the shear strength decreases with higher temperatures, nevertheless, the proportion between the different cobalt contents stays approximately the same. Examining the absolute values of shear strength, it can be observed that for the as reflowed samples, approximately 32 MPa is achieved, while for the thermally aged samples, around 23 MPa is reached when tested at room temperature. In comparison, the shear strength values obtained from the push-off shear tests are significantly higher, at approximately 53 MPa and 43 MPa, respectively. This demonstrates that the absolute values cannot be compared between these two testing methods, since the achieved shear strength is about twice as high for the push-off shear tests, which may be due to the different testing speed. However, the overall proportions remain consistent across these methods, even tough the increase of shear strength with 0.1 % cobalt nanoparticle additions is higher for the button samples, with about 14 %, compared to only 6 % for the lap-shear joints. A possible reason for the different results is, that different sample types where used, the cross section of them can be seen in Fig. 41. Comparing them shows that the button samples still have the excess solder, which strengthens the joint leading to higher shear strength. The exact values can be found in table 12 and individual results of each test are given in tables A25, A26, A27, A28, A29 and A30 in the appendix.

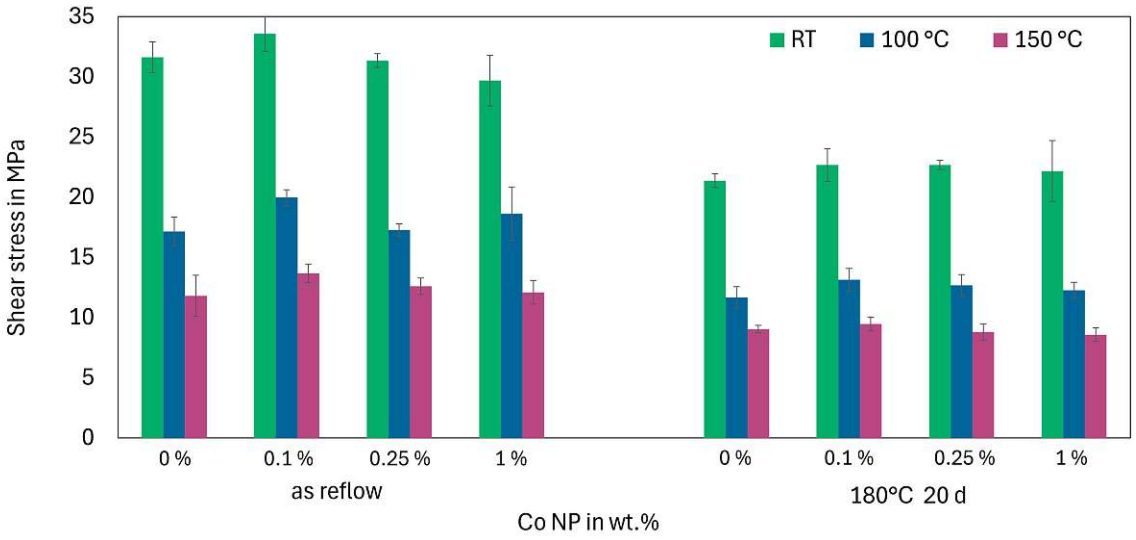

Figure 40: Shear stress of the lap-shear joints with different cobalt NP contents, thermal treatments and testing temperatures.

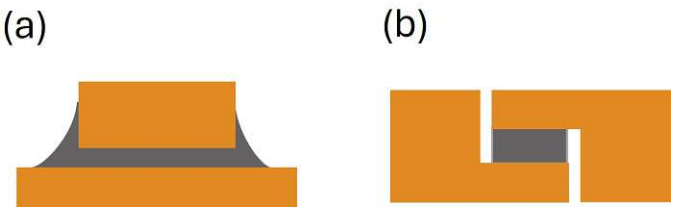

Figure 41: Cross section of (a) a button sample and (b) a lap-shear joint.

Table 12: Results of the shear tests with the lap-shear joint specimen.

Temperature treatment	Testing temperature	Co NP	Shear strength in MPa
as reflow	RT	0.00%	31.6 ∓ 1.3
		0.01%	33.6 ∓ 1.5
		0.25%	31.4 ∓ 0.6
		1.00%	29.7 ∓ 2.1
	100 °C	0.00%	17.1 ∓ 1.2
		0.01%	20.0 ∓ 0.6
		0.25%	17.3 ∓ 0.5
		1.00%	18.6 ∓ 2.2
	150 °C	0.00%	11.8 ∓ 1.7
		0.01%	13.7 ∓ 0.8
		0.25%	12.6 ∓ 0.7
		1.00%	12.1 ∓ 1.0
180 °C 20 d	RT	0.00%	21.4 ∓ 0.6
		0.01%	22.7 ∓ 1.4
		0.25%	22.7 ∓ 0.4
		1.00%	22.2 ∓ 2.5
	100 °C	0.00%	11.7 ∓ 0.9
		0.01%	13.2 ∓ 0.9
		0.25%	12.7 ∓ 0.9
		1.00%	12.3 ∓ 0.6
	150 °C	0.00%	9.0 ∓ 0.3
		0.01%	9.5 ∓ 0.6
		0.25%	8.8 ∓ 0.7
		1.00%	8.6 ∓ 0.6

3.4.2. Stress-Relaxation Test Results

The smoothed recorded stress relaxation curves and their average curves are depicted in Fig. 42, 43, 44, 45, 46 and 47. The data is presented for different cobalt nanoparticle contents, testing temperatures and thermal treatments, providing a comprehensive overview of the measured data. In the figures, (a) consistently represents 0.00 %, (b) corresponds to 0.10 %, (c) to 0.25 %, and (d) to 1.00 % cobalt nanopowder addition in

the flux. During the smoothing process, all recorded values were averaged over a time window of 5 seconds to reduce fluctuations and obtain a more stable representation of the data.

a) As Reflow Samples

i. Tested at Room Temperature

Figure 42 highlights that the starting load was the highest for 0.01 % Co NP and the lowest for 0.00 and 1.00% Co NP. For all cobalt content variations it can be seen, that the stress varies at least about 2 MPa in the beginning, tough the difference is most pronounced at 0.00 % Co NP. However, when looking at the stress after one hour, the values for 0.00 % Co NP are very close to each other in contrast to the others.

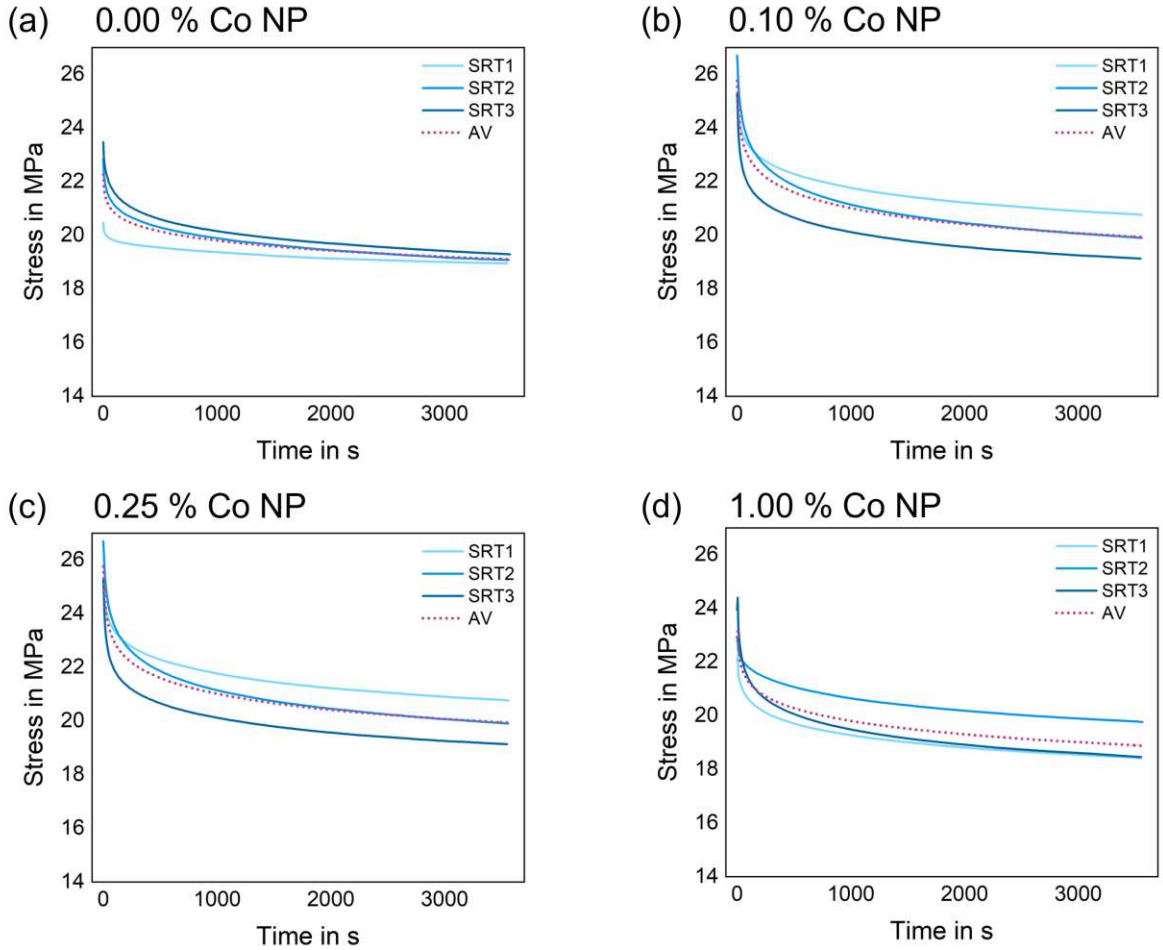

Figure 42: Stress relaxation curves for as reflowed samples tested at room temperature with varying cobalt NP content.

ii. Tested at 100 °C

In contrast to the previous curves, it can be seen in Fig. 43 that the curves fluctuate significantly more at the higher test temperatures, even tough they are smoothed. For the 0.25 % Co NP the individual curves fit together very well and at 0.00 and 0.25 % cobalt nanoparticles the starting values are almost identical. At 0.00 % Co NP it is noticeable that although the start and end values fit together very well, the curves in the middle range deviate from each other more strongly. A large contrast in the starting stress is visible for 0.10 % cobalt nanoparticles, but also reaches the highest stress values again.

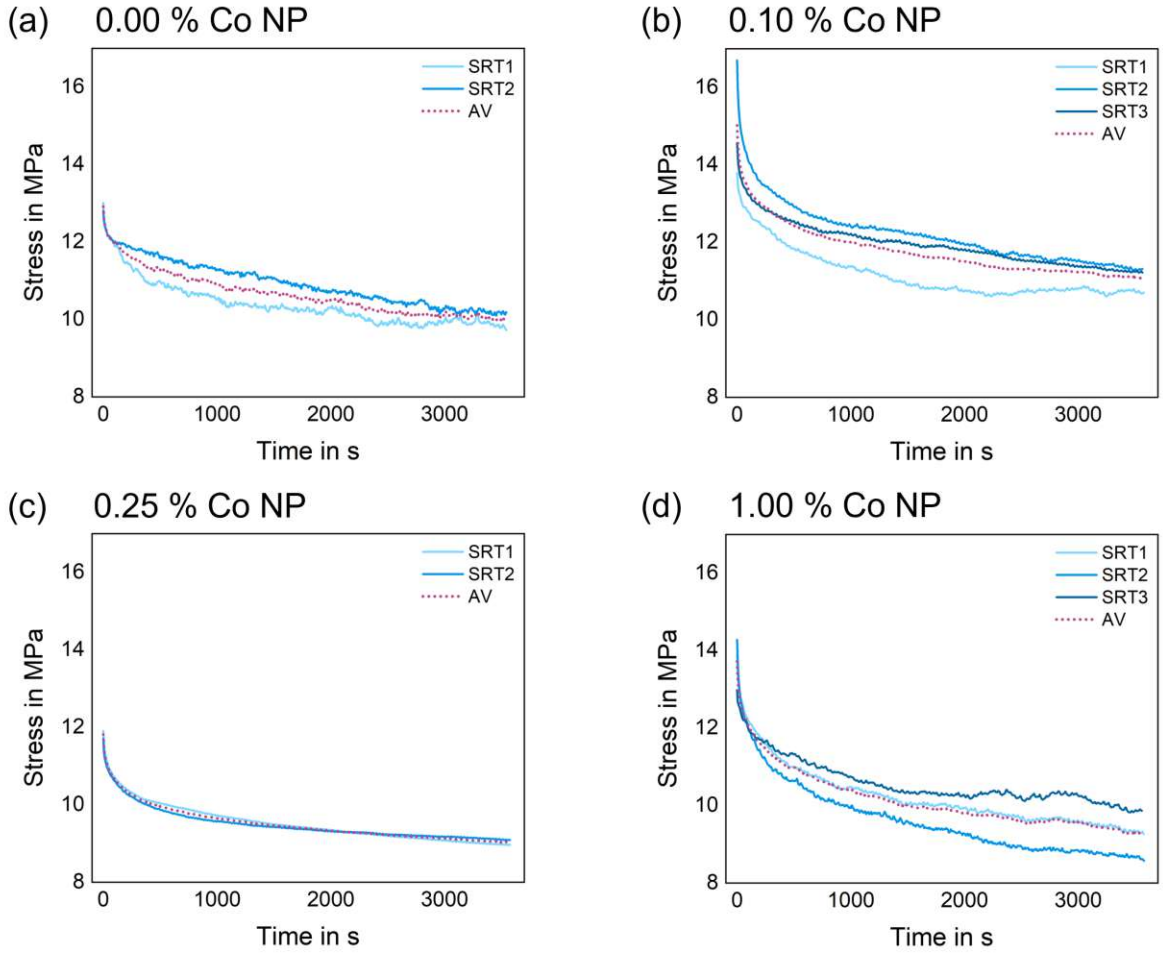

Figure 43: Stress relaxation curves for as reflowed samples tested at 100 °C with varying cobalt NP content.

iii. Tested at 150 °C

It is evident that the 0.00 % Co NP curves, in Fig. 44 differ quite from each other, because the SRT1 curve has a significantly steep decline, despite the higher starting stress. It is also noticeable that the curves with 0.10 % Co NP falls more sharply towards the end and are significantly further away from the steady state than the previous curves. The curves do not fluctuate noticeably more at a test temperature of 150 °C than at 100 °C, but it is observable that in comparison to before the curves are usually very close together at the beginning and move further apart towards the end. As in the previous cases, the stress values at 0.10 % Co NP are again highest, due to the higher starting load.

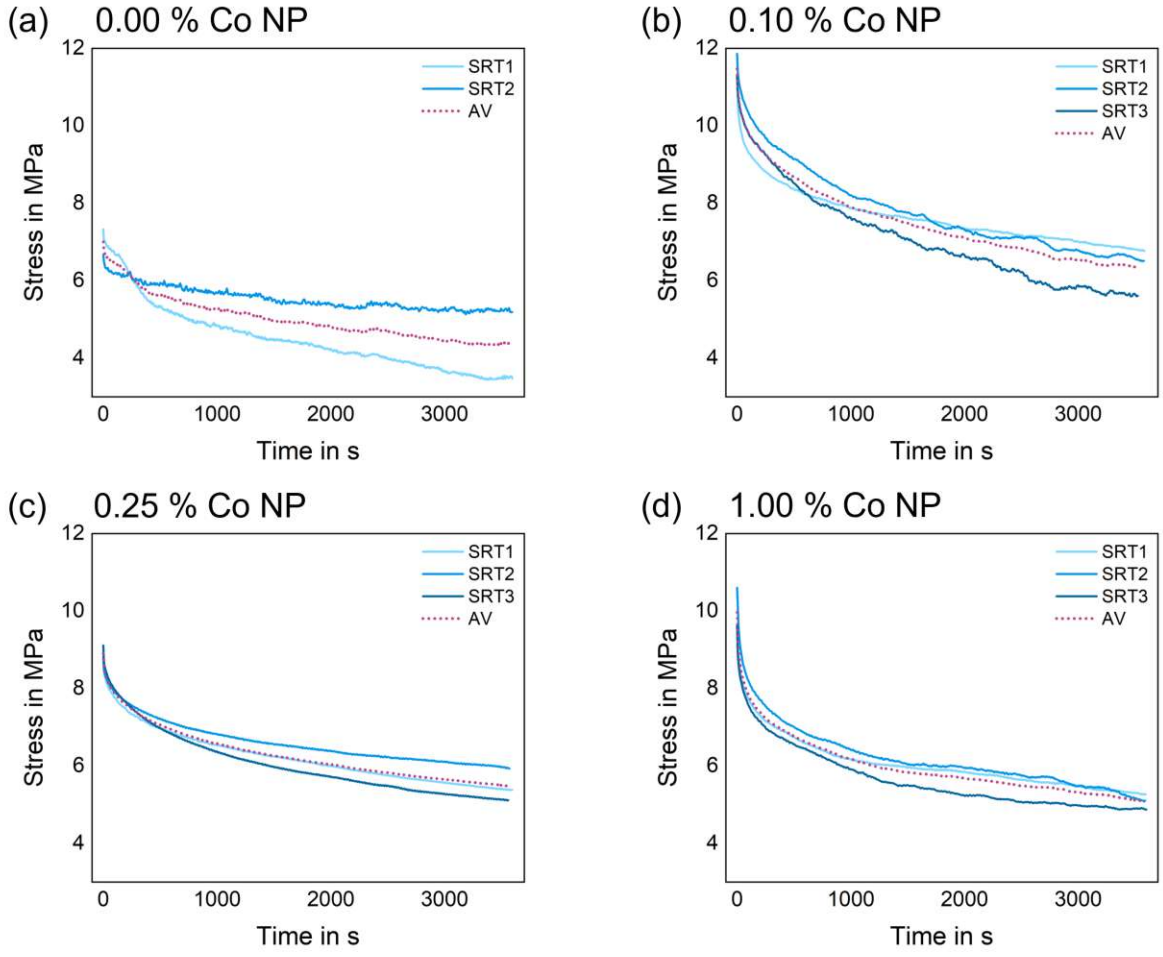

Figure 44: Stress relaxation curves for as reflowed samples tested at 150 °C with varying cobalt NP content.

b) Thermally Aged Samples at 180 °C for 20 Days

i. Tested at Room Temperature

It is noticeable in Fig. 45 that the starting stress is the lowest at 0.01 % cobalt nanoparticles although the highest load was applied there. At 0.00 and 1.0 % Co NP the starting stress varies greatly, whereas at 0.10 and 0.25 % it remains almost the same. It is also evident that at 0.00 and 0.25 % cobalt nanoparticles the curves are very close to each other, whereas at 0.10 and 1.00 % each one deviates more strongly.

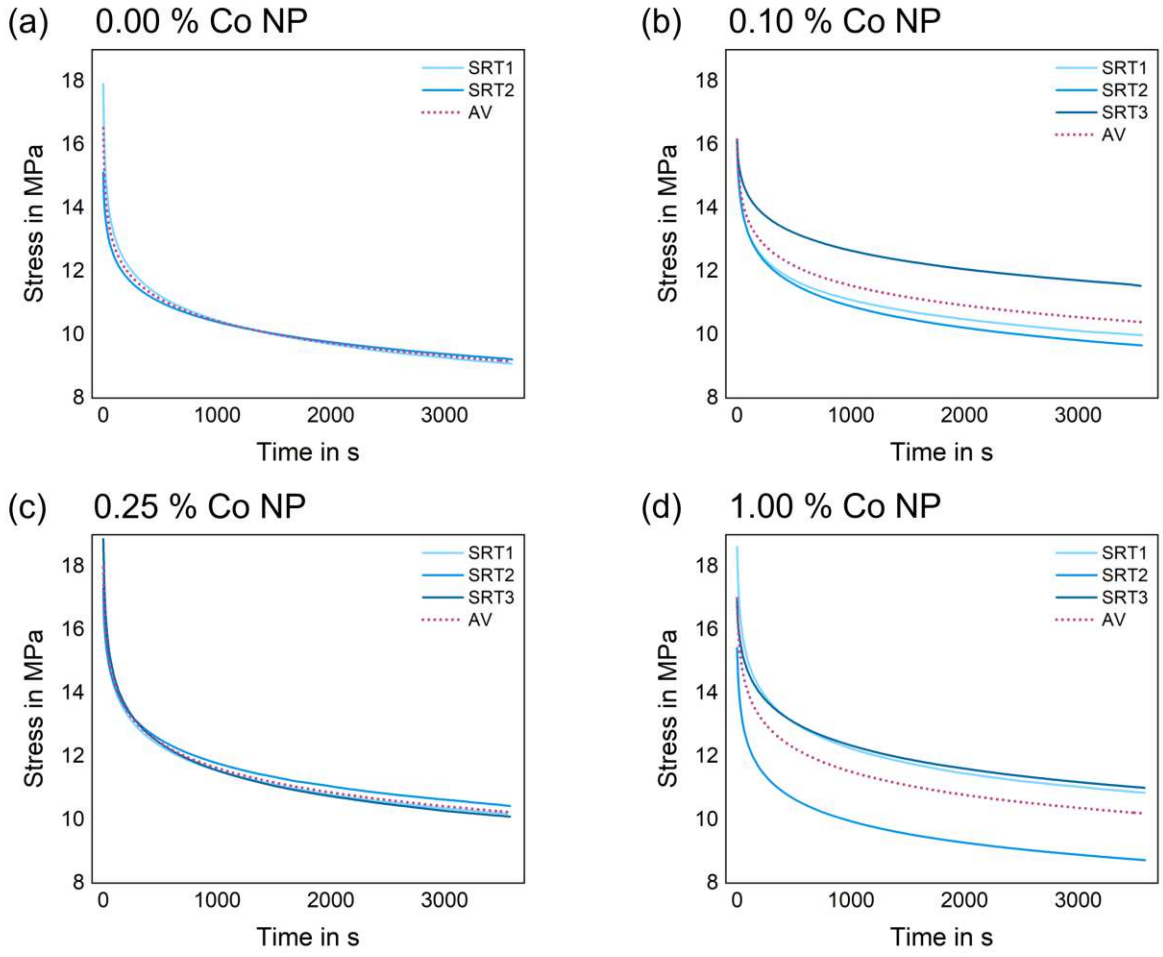

Figure 45: Stress relaxation curves for aged samples tested at room temperature with varying cobalt NP content.

ii. Tested at 100 °C

In figure 46, the 0.00 % Co NP curves are particularly striking, since the starting stress is very similar and the curves are almost identical. The starting values are generally very close to each other except for 0.25 % cobalt nanoparticles. As with the non-aged curves, they are more irregular at higher test temperatures. The 0.10 % Co NP curves deliver lower start stress values than the 0.25 %, despite the same start load, but they are still higher than the other curves with a lower starting load.

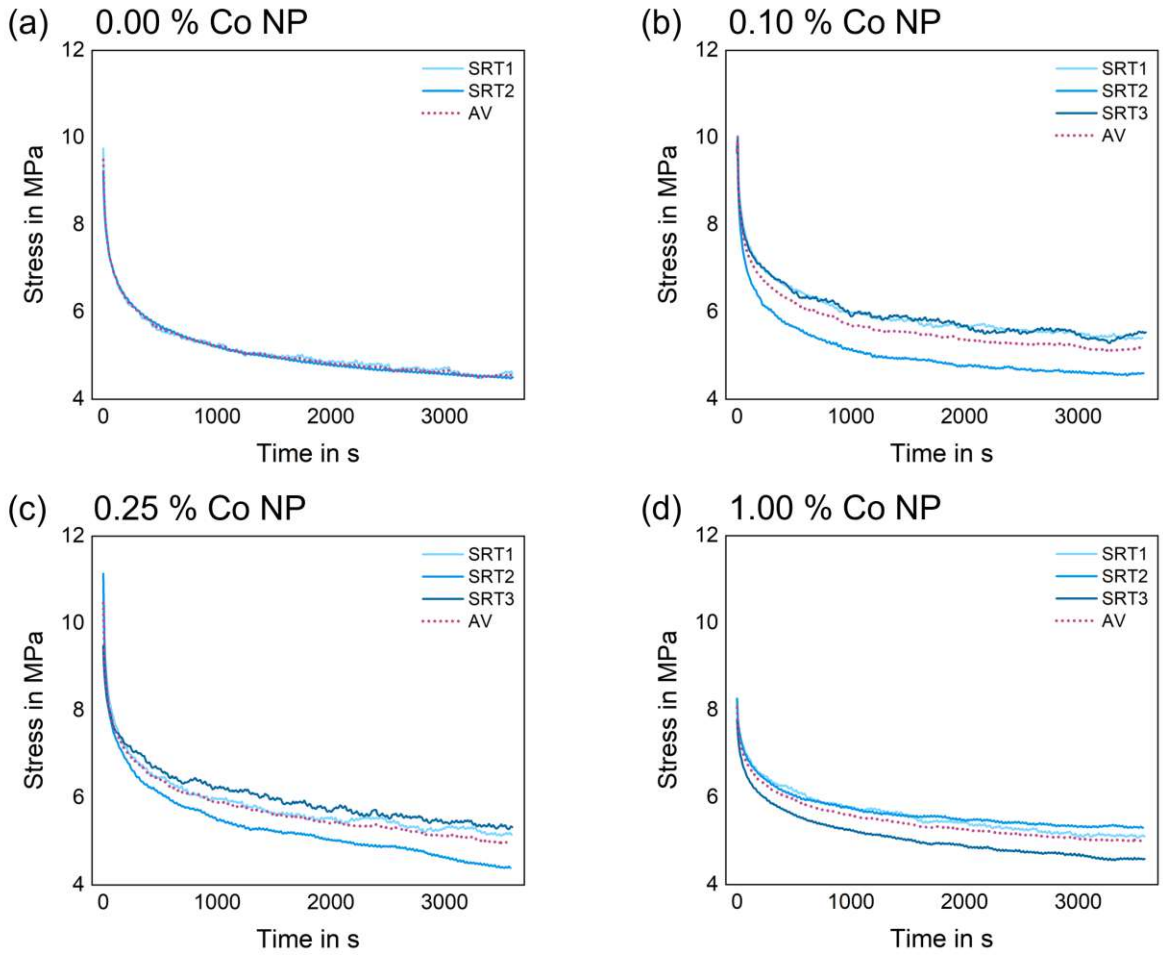

Figure 46: Stress relaxation curves for aged samples tested at 100 °C with varying cobalt NP content.

iii. Tested at 150 °C

In Fig. 47, this time all starting values of the respective cobalt concentrations are relatively close to each other and the highest are again reached by 0.00 % Co NP. At 0.00 and 0.10 % Co NP the curves are again very similar, although the others do not deviate too much from each other either. It is also evident that additional measurements have little impact on the average curve.

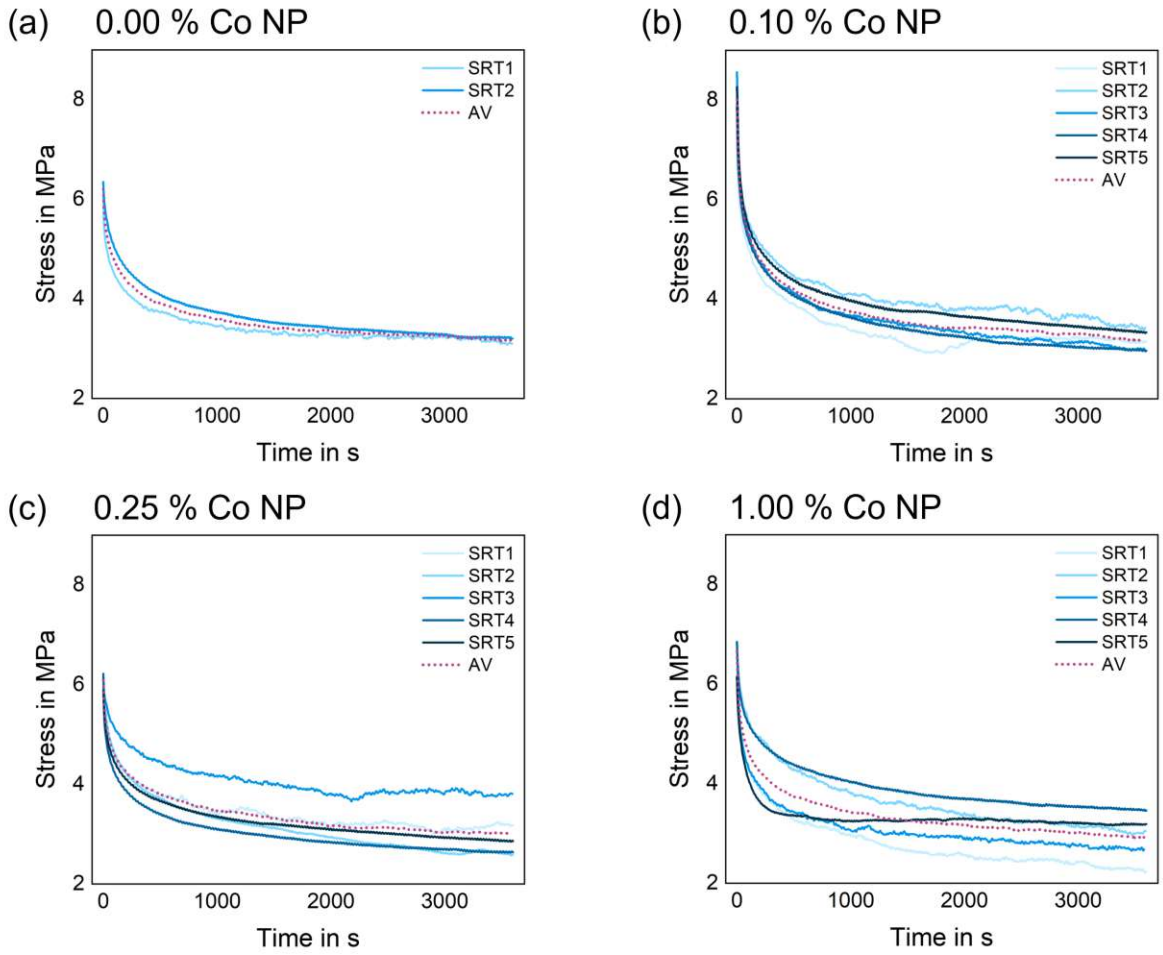

Figure 47: Stress relaxation curves for aged samples tested at 150 °C with varying cobalt NP content.

The following analysis is based on the average curves presented in the chapter 'Stress-Relaxation Test Results'.

3.4.3. Comparison at Different Testing Temperatures

a) As Reflow Samples

Figure 48 shows that in all cases the room temperature measurements relax the least followed by the tests conducted at 100 °C. It can also be noticed that the averaged curves still show stronger fluctuations in the tests above room temperature. It is also interesting that it seems as if the steady state is even further away in the 150 °C tests, since the curves fall relatively sharply in contrast to lower test temperatures. By comparing the distance between the curves, it is apparent that the room temperature and 100 °C curves are always closer to each other than 150 °C, which is usually two to three times as far away. This distance becomes even larger after longer testing periods, whereas the distance between room temperature and 100 °C remains fairly constant after an initial drop.

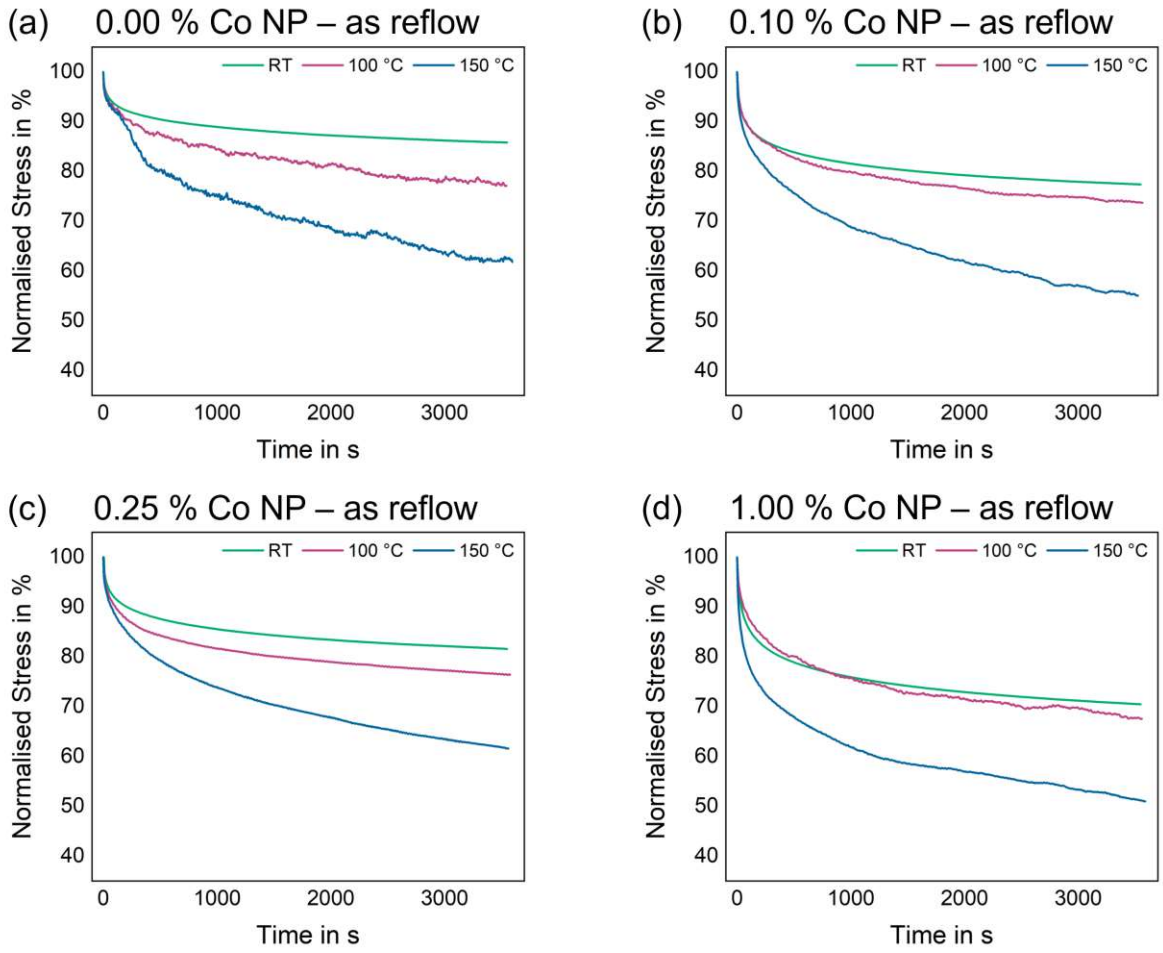

Figure 48: Stress relaxation curves with varying testing temperatures for the as reflow samples.

b) Aged samples

What is very unexpected about the curves in Fig. 49 is that the curves show a different correlation with temperature compared to the as reflow samples, even tough it is commonly known that the relaxation rate increases with rising test temperature. At 0.00 and 0.10 % Co NP, the samples tested at 100 °C relax slightly more than those tested at 150 °C, the same is the case at 1.00 %, where they relax slightly more at room temperature than at 100 °C. A possible reason for this behaviour, could be the strongly varying starting load due to the different shear strengths. It is also interesting that the drop in all curves is close to steady state, and the 150 °C tests do not drop significantly more as it was the case with the as reflow curves. The distances between the curves also vary greatly, at 0.0 and 0.10 % Co NP they are very close to each other whereas at 0.25 % they are far apart and, most strikingly, are about the same distance from each other, which is a completely different behaviour than for the as reflow tests, where room temperature and 100 °C where close and 150 °C was further away, as is the case at 1.00 %.

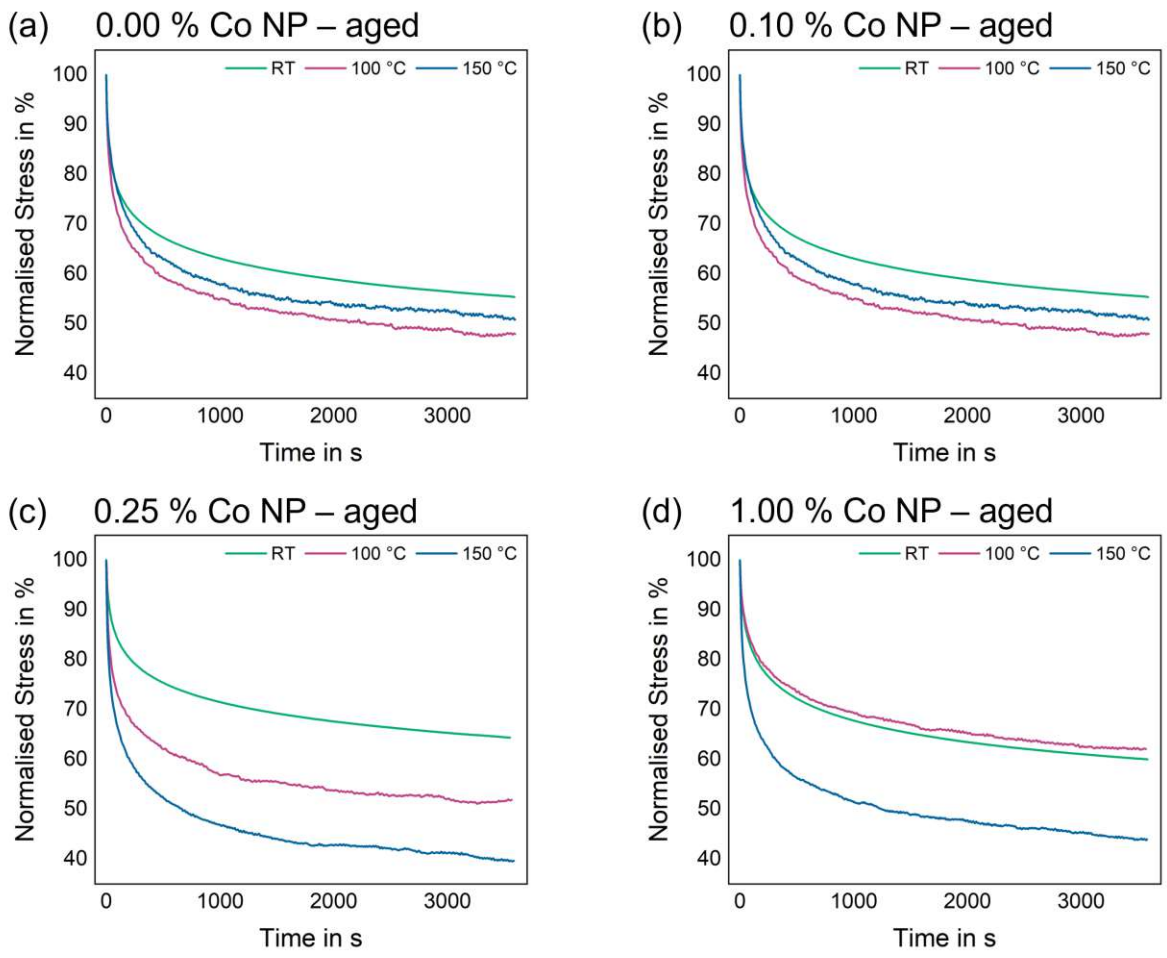

Figure 49: Stress relaxation curves with varying testing temperatures for the aged samples.

3.4.4. Comparison of As Reflowed and Aged Samples

a) Tested at room temperature

Taking a look at Fig. 50 it can be seen that for all cobalt NP variations the aged sample relaxes more than the as reflow, as it was expected, since the thermal treatment causes grain coarsening, which in turn reduces the strength. Interesting is that for the specimen without cobalt addition the difference between the curves is the largest, although the one at 0.25 % Co NP is also rather larger compared to the others. In all cases, it also looks as if the curves of the aged samples fall somewhat more sharply, what means that they are further away from steady state, but the difference is only small.

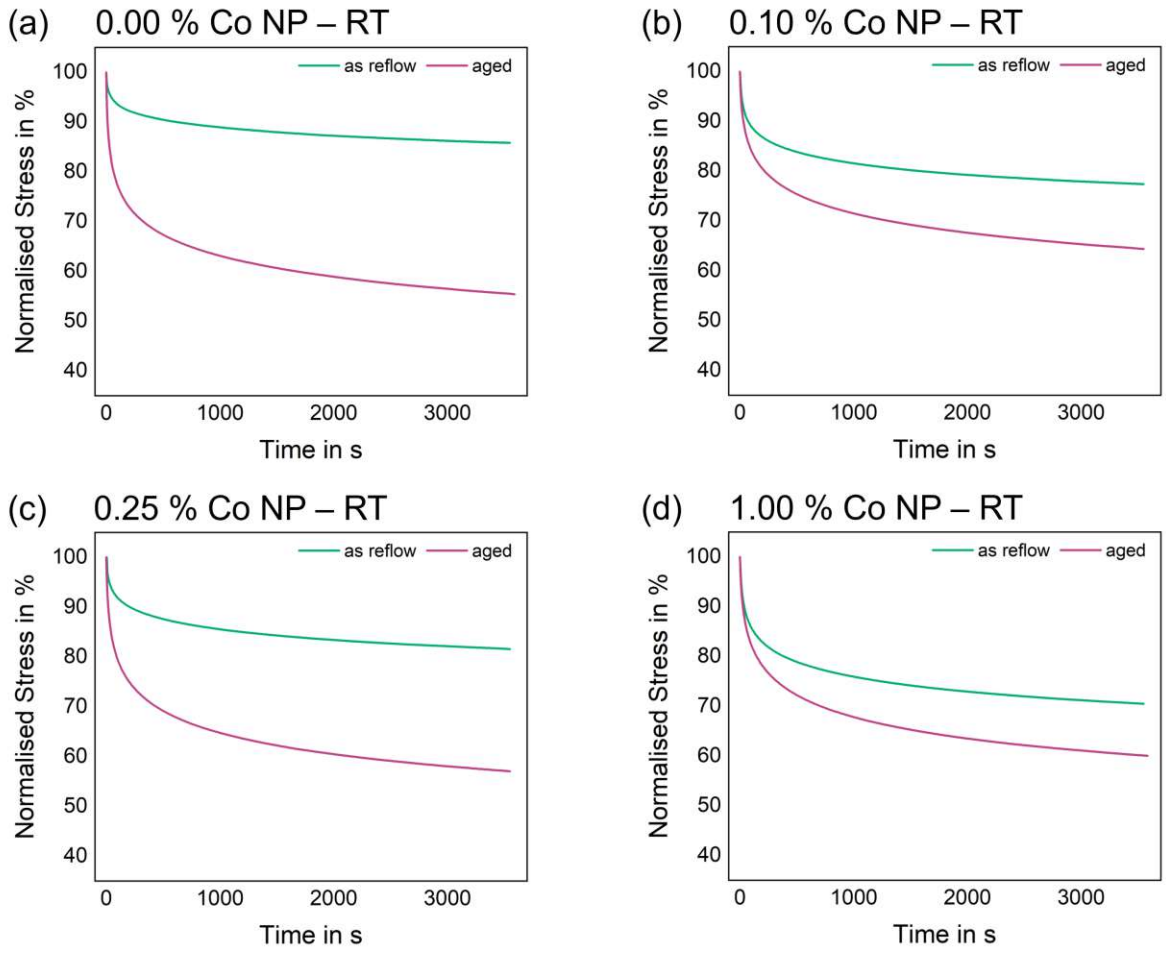

Figure 50: Stress relaxation curves with varying thermal treatments for the room temperature samples.

b) Tested at 100 °C

As in the test at room temperature, the test at 100 °C in Fig. 51 the curve of the samples without Co NP has the largest distance between the aged and the reflow curve, although the distance between the 0.10 and 0.25 % cobalt nanopowder curves is also large. As before, the curves of the aged specimens relax more than those of the as reflowed samples. Interestingly, at 100 °C test temperature, there is no noticeable difference between the decay rates of the curves with different thermal treatments, with the decay being more similar to that of the aged specimens from the room temperature tests.

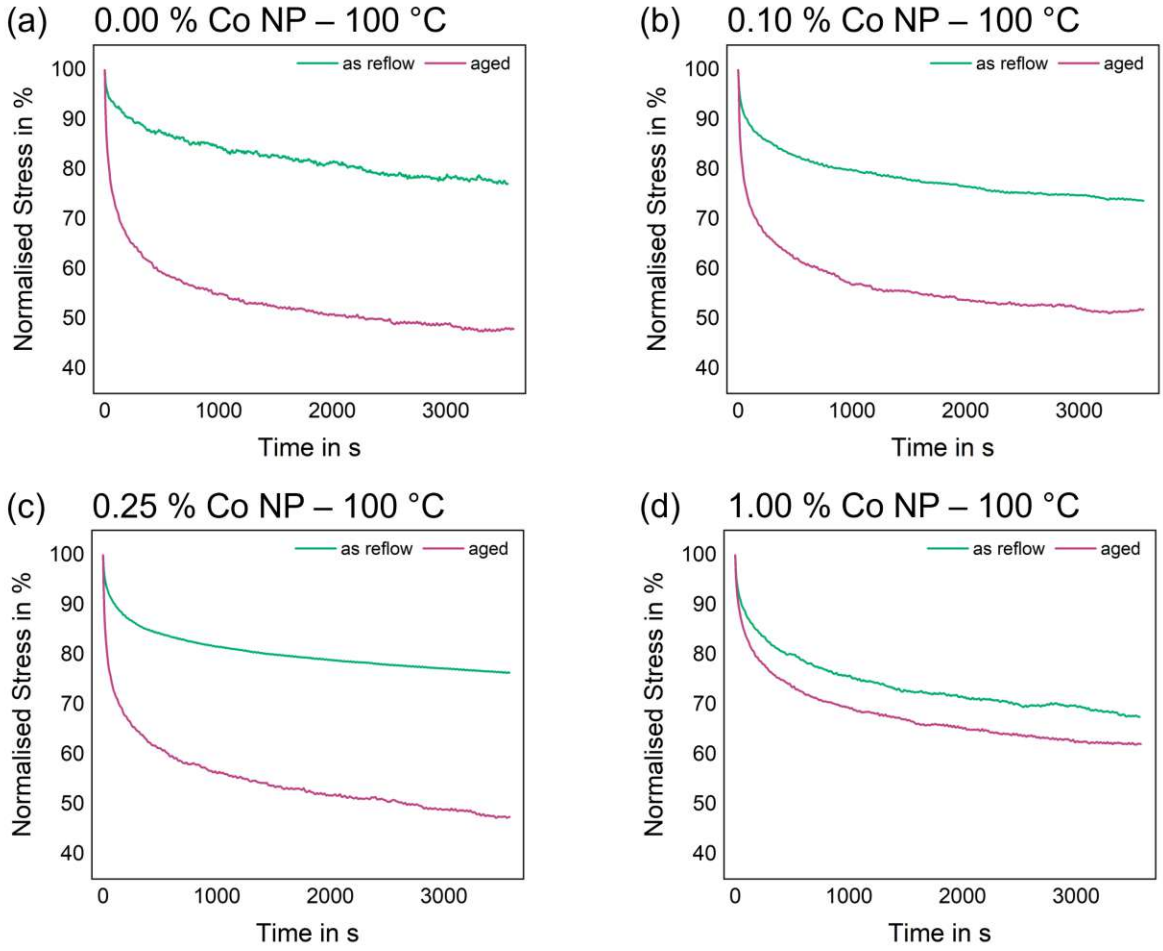

Figure 51: Stress relaxation curves with varying thermal treatments for the 100 °C samples.

c) Tested at 150 °C

Figure 52 shows the same behaviour that we have already seen at other test temperatures, in particular, that the curves of the aged samples relax significantly more. What is unusual in comparison to the other test temperatures is that all curves with different thermal treatments are approximately the same distance apart. The distance is roughly the average of the previous curves, falling between the smallest and largest distances observed at lower temperatures. It is also interesting that, in contrast to before, the curves of the as reflow specimen seem to fall more sharply. However, it must also be noted that the distance between the 1.00 % Co NP curves is again the smallest, just like at the other two test temperatures before.

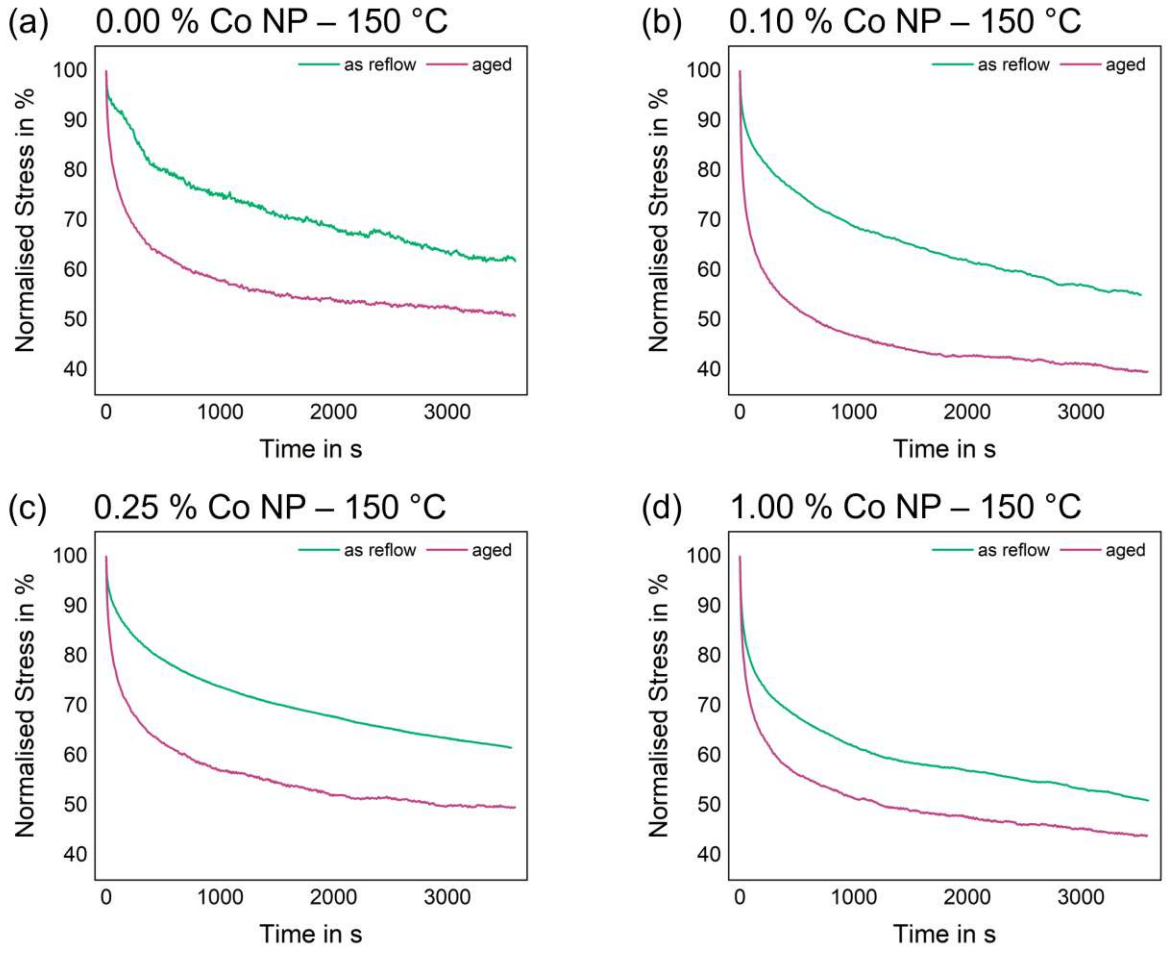

Figure 52: Stress relaxation curves with varying thermal treatments for the 150 °C samples.

3.4.5. Influence of Cobalt Content

In general, Fig. 53 shows that the curves of the samples with different cobalt NP contents fit well together in each diagram, except for the aged 1.00 % Co NP curve tested at 100 °C, depicted in Fig. 53 (d). The effect that the curves fluctuate more at higher test temperatures is also clearly visible in this overview. When comparing the decay between the curves for the different thermal treatments in general, it can be seen that the aged curves decay faster and more sharply.

When evaluating the different testing temperatures, it is evident that, both for the as reflow and the aged samples, the curves decrease more and more with increasing testing temperatures. Observing the drop after a few minutes, it is noticeable that at higher test temperatures, the curve remains further from the steady state, meaning it continues to decline more steeply, compared to lower temperatures.

Looking at the variation of the Co NP addition in the as reflow specimens, it is visible that at all test temperatures, 0.00 % Co NP relaxes the least, followed by 0.25 and 0.10 %. So, in general, the addition of cobalt nanoparticles leads to higher stress drop in as reflow condition.

However the aged specimen act different. There the addition of cobalt nanoparticles decreases the stress drop, except for the tests conducted at 150 °C. Upon examining the 150°C curves, one might initially suspect them to be outliers, leading to the decision to conduct further tests. However, subsequent experiments yielded the same results, indicating that a significant change must occur at elevated temperatures. To gain more insight, additional microstructural examinations are needed.

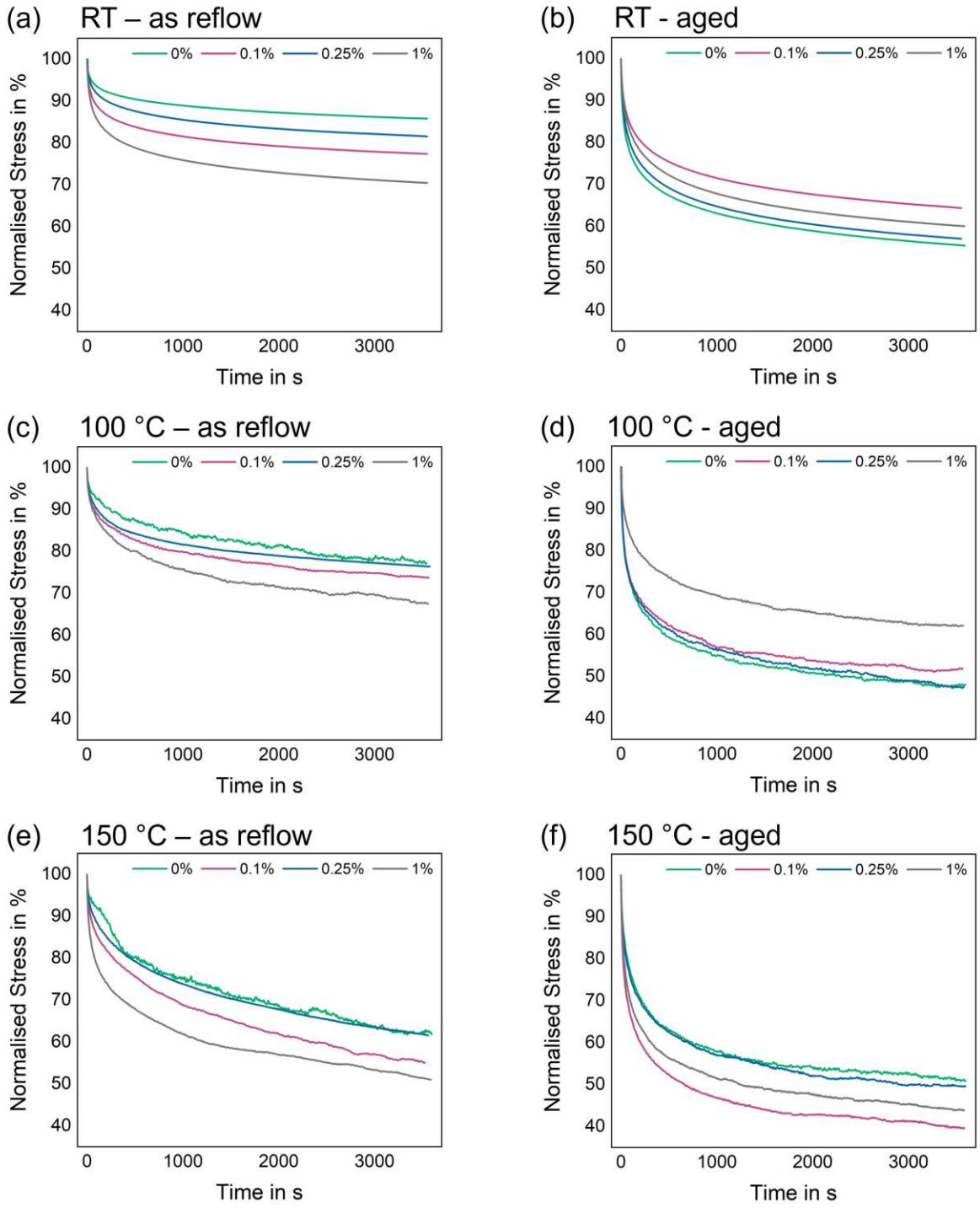

Figure 53: Stress relaxation curves with varying cobalt NP content.

3.4.6. Relaxation Behaviour

Table 13 reveals, that the load drop exhibits considerable variations and large standard deviations. To compare the results with and without cobalt nanoparticle additions, a linear fit was applied to the load drop data, which is depicted in Fig. 54. However, due to the significant deviation of the 0.10 % sample aged at 100 °C displayed in Fig. 54 (b), it was excluded from the fitting process. The values of the relaxation results for the single curves are in table A31 in the appendix. In general, the values for each test temperature are very close to each other and often within the standard deviation of the other cobalt contents. However, the linear regression of the as reflow condition reveals a slight increase in load drop with the addition of cobalt. After ageing the gradient is even weaker. Zimprich et al. (2009)[45] determined that the stress drop depends on the solder gap size, more specifically it decreases for thinner gaps due to the lack of ductility. This could explain the lower stress drop observed without additions. As the greater IMC thickness in the absence of cobalt results in smaller solder gap with decreased ductility, that is less capable of absorbing stress. This is also consistent with the lower impact observed in the aged samples, since the difference in IMC thickness is smaller too. It is also noticeable that in as reflow condition with 0.25 % additions, the load drop tends to be lower, while at 0.10 %, it appears slightly above the fit line, even though both concentrations achieved high shear strength. However, this trend is not observed in the aged samples.

Focusing on the different test temperatures, it is clear that that the load drop increases with rising test temperatures, due to the general increase of ductility in metals at higher temperatures. Similar results where achieved from Jadhav et al. (2001)[32]. They reported a stress drop of 10 % at 25 °C and 37 % at 150 °C aligning well with the results of 14 and 42 % in this study. A large increase in load drop is visible comparing the values before and after ageing. This may be explained by the agglomeration, coarsening and reduced number of Sn_3Ag precipitates in the solder bulk after thermal ageing, as already shown in Fig. 27, which results in increased ductility.[46]

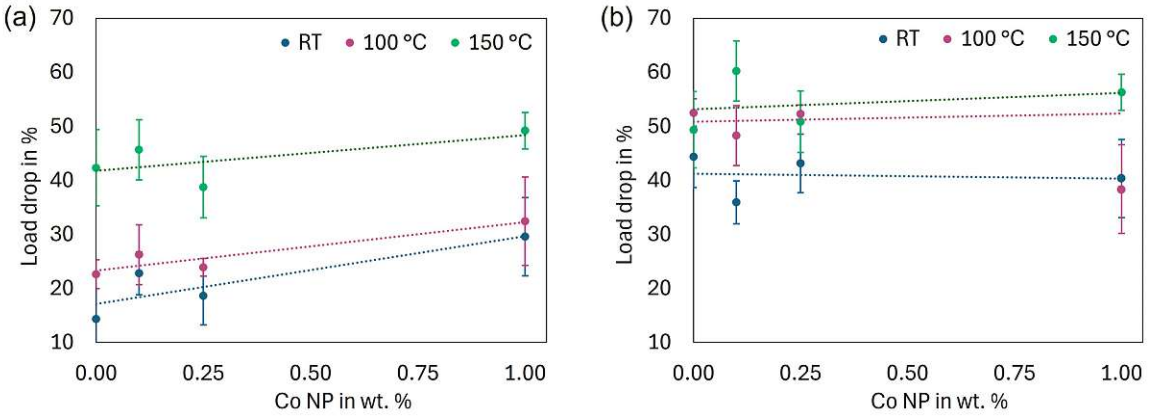

Figure 54: Relaxation behaviour at different Co Np contents for (a) as reflow and (b) aged specimen.

Table 13: Comparison of load drop before and after ageing at different testing temperatures and with varying cobalt nanoparticle contents

Temperature treatment	Testing temperature	Co NP	Load drop in %
as reflow	RT	0.00%	14 ∓ 6
		0.01%	23 ∓ 4
		0.25%	19 ∓ 5
		1.00%	30 ∓ 7
	100 °C	0.00%	23 ∓ 3
		0.01%	26 ∓ 6
		0.25%	24 ∓ 2
		1.00%	32 ∓ 8
	150 °C	0.00%	42 ∓ 7
		0.01%	46 ∓ 6
		0.25%	39 ∓ 6
		1.00%	49 ∓ 3
180 °C 20 d	RT	0.00%	44 ∓ 7
		0.01%	36 ∓ 6
		0.25%	43 ∓ 3
		1.00%	40 ∓ 5
	100 °C	0.00%	52 ∓ 1
		0.01%	48 ∓ 5
		0.25%	52 ∓ 8
		1.00%	42 ∓ 3
	150 °C	0.00%	49 ∓ 1
		0.01%	60 ∓ 4
		0.25%	51 ∓ 8
		1.00%	56 ∓ 8

3.4.7. Stress Exponent Analysis

In general a higher stress exponent suggests dislocation-controlled creep, which is controlled by the climb and annihilation of dislocations. In contrast, a lower stress exponent proposes diffusion-controlled creep, where the material deforms through vaccenic diffusion, which is more sensitive to temperature.[47]

The stress exponent was determined in the high stress region and the results at different temperatures are depicted in Fig. 55. It can be seen that the stress exponent decreases at higher testing temperatures, but it is also important to point out that the scales differ on the two digrams. Probable factors contributing to this are the general increase of diffusion at higher temperatures. The increased grain boundary sliding also leads to a diminished stress dependency leading to lower stress exponent values.[47] This means that the mechanism moves from dislocation-controlled creep at lower temperatures to a rather diffusion-controlled creep at higher temperatures. The general increase in ductility of metals at higher temperatures could also play an important role in this result.

Comparing the as reflow and aged values, with respect to the different scales, it can be seen that the values are more or less halved after the thermal treatment. Potential explanations for this include that the dislocations introduced by soldering and rapid cooling in air, recover during ageing leading to less dislocations and therefore less strength. The grain coarsening and thus the reduction of grain boundaries and dislocations further enhances this effect. Sidhu et al. (2008)[48] suggest that Sn_3Ag particles act as barriers to dislocation motion and since they tend to coarsen during the ageing process, this leads to an decrease of the creep resistance. Another important factor is that the IMC grows and coarsens too, leading to more brittleness that can introduce cracks which have an negative impact on the stress exponent. The diagrams also demonstrate that with 0.10 % cobalt NP addition the stress exponent reaches the highest values except the aged specimen tested at 150 °C. However the aged samples tested at 150 °C, have almost the same values regardless of the cobalt content, possible reason for this behaviour will be discussed in the next paragraph.

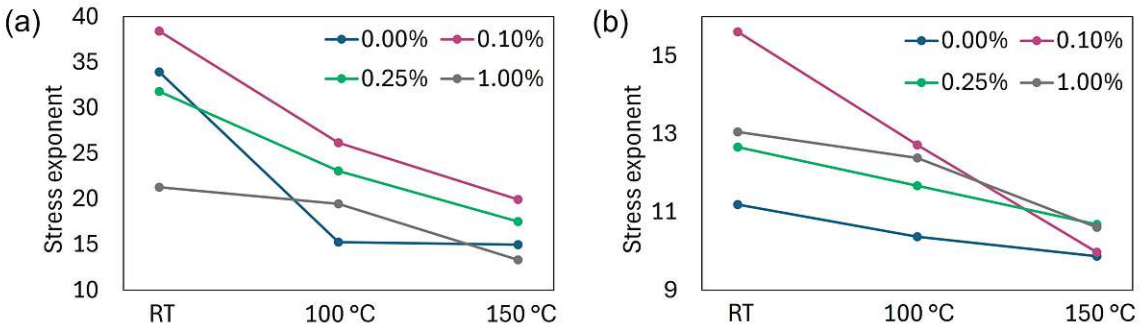

Figure 55: Stress exponent at different testing temperatures for (a) as reflow and (b) aged specimen.

Figure 56 outlines the influence of cobalt nanoparticles on the stress exponent and therefore the creep resistance. The specific values are presented in Table 14. It is also important to note, that the stress exponent is calculated based on the steep decline observed in the initial minutes of the stress relaxation test, meaning that it reflects the early deformation behaviour, far from the point of failure. Compared to the relaxation which represents the whole test and depends rather on the general thickness of the solder gap.

In as reflow condition 0.10 % cobalt nanoparticle additions lead to the highest stress exponent. As discussed earlier the addition of 0.10 % leads to a finer Cu_6Sn_5-phase, shown in Fig. 32, and therefore higher strength.[19] Noticeable is that the stress exponent decreases again with the addition of more than 0.10 % Co NP. This might be explained by the segregation and agglomeration of the nanoparticles, as seen in Fig. 31, causing them to be ineffective or even increase the stress concentration which could lead to the formation of cracks and therefore the decrease of the stress exponent.

After ageing the increase with 0.10 % cobalt nanoparticle addition is diminished, and even completely vanished at 150 °C. Reasons for this behaviour could be that the improvements, discussed in the earlier chapters, with 0.10 % additions are in general reduced after ageing. That the cobalt content for aged specimen tested at 150 °C has no impact on the stress exponent could be, because of the change from a dislocation-controlled creep, to a rather diffusion controlled creep with higher temperatures.[47] This could lead to the influence of bulk tin being so great that the IMC no longer has any visible effect.

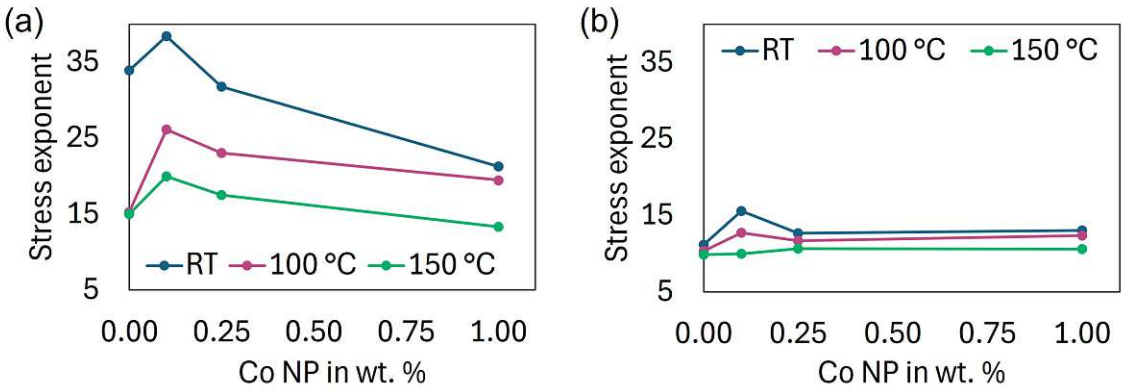

Figure 56: Stress exponent with different Co NP contents for (a) as reflow and (b) aged specimen.

Thermal treatment	Testing temperature	Co NP	Stress exponent
as reflow	RT	0.00 %	33.9
		0.10 %	38.4
		0.25 %	31.8
		1.00 %	21.3
	100 °C	0.00 %	15.3
		0.10 %	26.2
		0.25 %	23.1
		1.00 %	19.5
	150 °C	0.00 %	15.0
		0.10 %	20.0
		0.25 %	17.5
		1.00 %	13.3
180 °C 20 d	RT	0.00 %	11.2
		0.10 %	15.6
		0.25 %	12.7
		1.00 %	13.1
	100 °C	0.00 %	10.4
		0.10 %	12.7
		0.25 %	11.7
		1.00 %	12.4
	150 °C	0.00 %	9.9
		0.10 %	10.0
		0.25 %	10.7
		1.00 %	10.6

Table 14: Measured stress exponent.

Table 15 provides an overview of literature values for the stress exponent in the high stress region of solder joints without nanoparticles. Since nanoparticle enhanced solders are a relatively recent innovation, no studies for direct comparison could be found. When comparing them with each other, they display a marked difference. Zimprich et al. (2008)[45] suggest this could be because of variations of the measurement parameters like, the size and type of specimen, the sample preparation or the strain rate used. The decrease at higher testing temperatures observed in this study is consistent with findings reported in the literature. The stress exponent tested at room temperature does not match any of the references but lies between the values. However, testing at higher temperatures resulted in similar values as those reported by Magnien J. (2015)[49].

Table 15: Reported high stress region stress exponent values in the literature

Reference	Solder	Stress exponent	
		Room temperature	120/125 °C
Jadhav et al. (2001)[32]	Sn-3.5Ag	12.2	10
Zimprich et al. (2008)[45]	Sn-3.5Ag	11	6
Magnien J. (2015)[49]	SAC	121.0	13.0

4. Conclusion

This study investigates the addition of cobalt nanoparticles to the flux and how it influences the mechanical performance of Cu/Sn3.5Ag solder joints, with a specific focus on creep behaviour. The motivation for this research lies in the restriction of lead containing solders and also the ongoing miniaturization in electronics industry. Since lead-free solder joints have not yet reached the mechanical stability of lead-based joints, further improvements are necessary to improve their reliability. A promising possibility is the incorporation of cobalt nanoparticles to the flux, as earlier studies have shown, that incorporating nanoparticles can improve the strength of the solder joint. However, the creep characteristics still remain largely unexplored, which is why this study aims to provide new insights into their behaviour.

The results of this study demonstrate that the inclusion of Co NP in solder joints generally improves their mechanical performance when compared to traditional lead-free solders. A detailed examination of the microstructure shows that the growth of the Cu_6Sn_5 phase could be reduced and a more even morphology was exhibited. This effect could also be observed through deep etching. The highest performance was measured with an addition of 0.10 % Co NP. This trend is in agreement with the findings of Sujan et al. (2013)[18]. After the initial growth at soldering, the IMC growth rate remained largely unaffected by small amounts of cobalt. However, with higher Co NP concentrations, a faster growth of Cu_6Sn_5 phase and a reduction in Cu_3Sn phase were measured. This reduction in brittle IMC growth results in improved long-term stability during use. The calculated diffusion coefficients reflect this trend, by increasing for the Cu_6Sn_5 phase and decreasing for the Cu_3Sn phase with the addition of cobalt nanopowder. Consistent results were reported in the study conducted by Haseeb et al. (2017)[6]. The push-off shear tests showed a 13 % increase in performance with lower Co NP concentrations. Revealing a higher resistance to failure, thereby indicating potential for improved durability and reliability in more demanding applications. The same trend was achieved in the pre- and shear tests for the stress-relaxation tests and was also reported by Lee et al. (2008)[22]. However, no substantial results could be obtained for the relaxation behaviour, due to its strong dependence on the solder gap size. Significant results are observed for the stress exponent with 0.10 % cobalt nanopowder additions, suggesting solder with small amounts of Co NP maintain their structural integrity better under prolonged mechanical stress leading to an improved creep resistance. Since the addition of nanoparticles solders is a rather novel approach, no comparative data for the stress exponent was available. However, the solder without additions was comparable, and reviewing with Jadhav et al. (2001)[32], Zimprich et al. (2008)[45] and Magnien J. (2015)[49] confirmed that the obtained values fall within the expected range.

These findings underline that cobalt nanoparticle doped solders could be a promising alternative, especially in areas where solder joints are exposed to high mechanical loads and thermal cycles. However, further studies are needed to evaluate the long-term stability of the solder under different environmental conditions, assess their wettability, and optimize the cobalt content for industrial applications. Future research should also investigate alternative nanoparticle reinforcements to achieve similar or even better improvements.

References

[1] John H Lau and Ning-Cheng Lee. *Assembly and Reliability of Lead-Free Solder Joints*. eng. 1st ed. 2020. Singapore: Springer Singapore, 2020. ISBN: 9811539200. URL: 10.1007/978-981-15-3920-6.

[2] European Parliament and Council. *Directive 2002/95/EC on the Restriction of the Use of Certain Hazardous Substances in Electrical and Electronic Equipment (RoHS)*. Official Journal of the European Union L 37, 13.2.2003, pp. 19-23. 2003. URL: https://eur-lex.europa.eu/legal-content/DE/TXT/?uri=CELEX:32002L0095.

[3] Jasbir Bath. *Lead-Free Soldering*. Springer New York, NY, 2007. ISBN: 978-0-387-32466-1. DOI: https://doi.org/10.1007/978-0-387-68422-2.

[4] Wen-ming TANG et al. „Solid state interfacial reactions in electrodeposited Cu/Sn couples“. In: *Transactions of Nonferrous Metals Society of China* 20.1 (2010), pp. 90–96. ISSN: 1003-6326. DOI: https://doi.org/10.1016/S1003-6326(09)60102-3. URL: https://www.sciencedirect.com/science/article/pii/S1003632609601023.

[5] Venkatesh Sivasubramaniam et al. „Interfacial Intermetallic Growth and Strength of Composite Lead-Free Solder Alloy Through Isothermal Aging“. In: *J. Electron. Mater.* 37 (Oct. 2008), pp. 1598–1604. DOI: 10.1007/s11664-008-0524-2.

[6] A. S. M. A Haseeb et al. „Effects of Metallic Nanoparticles on Interfacial Intermetallic Compounds in Tin-Based Solders for Microelectronic Packaging“. In: *Journal of Electronic Materials* (May 2017), pp. 1–16. DOI: 10.1007/s11664-017-5591-9.

[7] G.K. Sujan, A.S.M.A. Haseeb, and A.B.M. Afifi. „Effects of metallic nanoparticle doped flux on the interfacial intermetallic compounds between lead-free solder ball and copper substrate“. In: *Materials Characterization* 97 (2014), pp. 199–209. ISSN: 1044-5803. DOI: https://doi.org/10.1016/j.matchar.2014.10.002. URL: https://www.sciencedirect.com/science/article/pii/S1044580314002940.

[8] Liang Zhang and K.N. Tu. „Structure and properties of lead-free solders bearing micro and nano particles“. In: *Materials Science and Engineering: R: Reports* 82 (2014), pp. 1–32. ISSN: 0927-796X. DOI: https://doi.org/10.1016/j.mser.2014.06.001. URL: https://www.sciencedirect.com/science/article/pii/S0927796X14000680.

[9] Irina Wodak et al. „Hybrid solder joints: the effect of nanosized ZrO2 particles on morphology of as-reflowed and thermally aged Sn–3.5Ag solder joints“. In: *Applied Nanoscience* 13 (July 2023). DOI: 10.1007/s13204-023-02912-4.

[10] Andriy Yakymovych et al. „Morphology and Shear Strength of Lead-Free Solder Joints with Sn3.0Ag0.5Cu Solder Paste Reinforced with Ceramic Nanoparticles“. In: *Journal of Electronic Materials* 45 (Aug. 2016). DOI: 10.1007/s11664-016-4832-7.

[11] L.C. Tsao. „An investigation of microstructure and mechanical properties of novel Sn3.5Ag0.5Cu–XTiO2 composite solders as functions of alloy composition and cooling rate“. In: *Materials Science and Engineering: A* 529 (2011), pp. 41–48. ISSN: 0921-5093. DOI: https://doi.org/10.1016/j.msea.2011.08.053. URL: https://www.sciencedirect.com/science/article/pii/S0921509311009476.

[12] Y. Wang, X. Zhao, X. Xie, et al. „Effects of nano-SiO_2 particles addition on the microstructure, wettability, joint shear force and the interfacial IMC growth of Sn3.0Ag0.5Cu solder“. In: *Journal of Materials Science: Materials in Electronics* 26.12 (2015), pp. 9387–9395. DOI: 10.1007/s10854-015-3151-8. URL: https://doi.org/10.1007/s10854-015-3151-8.

[13] Asit Kumar Gain, Y.C. Chan, and Winco K.C. Yung. „Effect of additions of ZrO2 nano-particles on the microstructure and shear strength of Sn–Ag–Cu solder on Au/Ni metallized Cu pads“. In: *Microelectronics Reliability* 51.12 (2011), pp. 2306–2313. ISSN: 0026-2714. DOI: https://doi.org/10.1016/j.microrel.2011.03.042. URL: https://www.sciencedirect.com/science/article/pii/S0026271411001764.

[14] Sara Hawi et al. „Development of carbonaceous tin-based solder composite achieving unprecedented joint performance“. eng. In: *Emergent materials (Online)* 4.6 (2021), pp. 1679–1696. ISSN: 2522-5731.

[15] Pham Van Son, Atsushi Fujitsuka, and Koji I. Ohshima. „Influence of 0.03 wt.% Carbon Black Addition on the Performance of Sn-3.5Ag Lead-Free Solder“. In: *Journal of Electronic Materials* 41.7 (2012), pp. 1893–1897. DOI: 10.1007/s11664-012-2023-8. URL: https://doi.org/10.1007/s11664-012-2023-8.

[16] Ze Zhu et al. „Effect of the size of carbon nanotubes (CNTs) on the microstructure and mechanical strength of CNTs-doped composite Sn0.3Ag0.7Cu-CNTs solder“. In: *Materials Science and Engineering: A* 727 (2018), pp. 160–169. ISSN: 0921-5093. DOI: https://doi.org/10.1016/j.msea.2018.05.002. URL: https://www.sciencedirect.com/science/article/pii/S0921509318306427.

[17] Huayu Sun, Y.C. Chan, and Fengshun Wu. „Effect of CNTs and Ni coated CNTs on the mechanical performance of Sn57.6Bi0.4Ag BGA solder joints“. In: *Materials Science and Engineering: A* 656 (2016), pp. 249–255. ISSN: 0921-5093. DOI: https://doi.org/10.1016/j.msea.2016.01.045. URL: https://www.sciencedirect.com/science/article/pii/S0921509316300430.

[18] G.K. Sujan, A.S.M.A Haseeb, and Amalina Ma. „Effects of metallic nanoparticle doped flux on interfacial intermetallic compounds between Sn-3.0Ag-0.5Cu and copper substrate“. In: *Proceedings of the 2013 IEEE 15th Electronics Packaging Technology Conference, EPTC 2013* (Dec. 2013), pp. 21–26. DOI: 10.1109/EPTC.2013.6745676.

[19] Xi Huang et al. „Investigating the impact of cobalt incorporation on the transformation of Cu6Sn5 layer to (Cu, Co)6Sn5: Microstructural and mechanical insights“. In: *Materials Characterization* 212 (2024), p. 113934. ISSN: 1044-5803. DOI: https://doi.org/10.1016/j.matchar.2024.113934. URL: https://www.sciencedirect.com/science/article/pii/S1044580324003152.

[20] Shengyan Shang et al. „Enhancement of hardness of bulk solder by doping Cu nanoparticles at the interface of Sn/Cu solder joint“. In: *Microelectronic Engineering* 208 (2019), pp. 47–53. ISSN: 0167-9317. DOI: https://doi.org/10.1016/j.mee.2019.01.009. URL: https://www.sciencedirect.com/science/article/pii/S0167931718303915.

[21] Linmei Yang, Shiran Ma, and Guowan Mu. „Improvements of microstructure and hardness of lead-free solders doped with Mo nanoparticles“. In: *Materials Letters* 304 (2021), p. 130654. ISSN: 0167-577X. DOI: https://doi.org/10.1016/j.matlet.2021.130654. URL: https://www.sciencedirect.com/science/article/pii/S0167577X21013513.

[22] Jung-Sub Lee et al. „Effects of Co addition in eutectic Sn–3.5Ag solder on shear strength and microstructural development“. In: *Microelectronic Engineering* 85.7 (2008), pp. 1577–1583. ISSN: 0167-9317. DOI: https://doi.org/10.1016/j.mee.2008.03.002. URL: https://www.sciencedirect.com/science/article/pii/S0167931708001433.

[23] Bakhtiar Ali et al. „Impact toughness, hardness and shear strength of Fe and Bi added Sn-1Ag-0.5Cu lead-free solders“. In: *Microelectronics Reliability* 63 (2016), pp. 224–230. ISSN: 0026-2714. DOI: https://doi.org/10.1016/j.microrel.2016.05.004. URL: https://www.sciencedirect.com/science/article/pii/S0026271416301019.

[24] Pei Yao, Ping Liu, and Jim Liu. „Effects of multiple reflows on intermetallic morphology and shear strength of SnAgCu–xNi composite solder joints on electrolytic Ni/Au metallized substrate“. In: *Journal of Alloys and Compounds* 462.1 (2008), pp. 73–79. ISSN: 0925-8388. DOI: https://doi.org/10.1016/j.jallcom.2007.08.041. URL: https://www.sciencedirect.com/science/article/pii/S0925838807016751.

[25] A.S.M.A. Haseeb and Tay See Leng. „Effects of Co nanoparticle addition to Sn–3.8Ag–0.7Cu solder on interfacial structure after reflow and ageing“. In: *Intermetallics* 19.5 (2011), pp. 707–712. ISSN: 0966-9795. DOI: https://doi.org/10.1016/j.intermet.2011.01.009. URL: https://www.sciencedirect.com/science/article/pii/S0966979511000239.

[26] A. Aspalter et al. „Hybrid solder joints: morphology and shear strength of Sn–3.0Ag–0.5Cu solder joints by adding ceramic nanoparticles through flux doping“. In: *Applied Nanoscience* 10 (Apr. 2020). DOI: 10.1007/s13204-020-01398-8.

[27] J.-H Shim et al. „Thermodynamic Assessment of the Cu-Sn System“. In: *Zeitschrift fuer Metallkunde/Materials Research and Advanced Techniques* 87 (Mar. 1996), pp. 205–212. DOI: 10.1515/ijmr-1996-870310.

[28] Chang-Seok Oh et al. „A thermodynamic study on the Ag-Sb-Sn system“. In: *Journal of Alloys and Compounds* 238.1 (1996), pp. 155–166. ISSN: 0925-8388. DOI: https://doi.org/10.1016/0925-8388(95)02191-4. URL: https://www.sciencedirect.com/science/article/pii/0925838895021914.

[29] Mike Judd and Keith Brindley. „5 - Flux“. In: *Soldering in Electronics Assembly (Second Edition)*. Ed. by Mike Judd and Keith Brindley. Second Edition. Oxford: Newnes, 1999, pp. 89–108. ISBN: 978-0-7506-3545-5. DOI: https://doi.org/10.1016/B978-075063545-5/50007-8. URL: https://www.sciencedirect.com/science/article/pii/B9780750635455500078.

[30] Norliza Ismail et al. „Flux Modification for Wettability and Reliability Improvement in Solder Joints“. In: *Advances in Soldering Technology for Electronic Packaging*. Springer, 2022. Chap. 9, [Seitenangabe einfügen]. DOI: 10.1007/978-3-030-93441-5_9. URL: https://www.researchgate.net/publication/358944120.

[31] William D Callister and David G Rethwisch. *Materialwissenschaften und Werkstofftechnik : eine Einführung*. ger. 1. Aufl. Weinheim: Wiley-VCH, 2013. ISBN: 3527330070.

[32] S. G. Jadhav et al. „Stress Relaxation Behavior of Composite and Eutectic Sn-Ag Solder Joints“. In: *Journal of Electronic Materials* 30.9 (2001), pp. 1197–1205. DOI: 10.1007/s11664-001-0150-8. URL: https://doi.org/10.1007/s11664-001-0150-8.

[33] W. Bang et al. „The correlation between stress relaxation and steady-state creep of eutectic Sn-Pb“. In: *Journal of Electronic Materials* 34 (Jan. 2005), pp. 1287–1300. DOI: 10.1007/s11664-005-0252-9.

[34] Fuqian Yang and Lingling Peng. „Impression creep of Sn3.5Ag eutectic alloy“. In: *Materials Science and Engineering: A* 409.1 (2005). Micromechanics of Advanced Materials II, pp. 87–92. ISSN: 0921-5093. DOI: https://doi.org/10.1016/j.msea.2005.03.119. URL: https://www.sciencedirect.com/science/article/pii/S0921509305007975.

[35] L. E. Jackson. „Techniques for Investigating the Structures of Tin-Base and Lead-Base Bearing Metals by Scanning Electron Microscopy“. In: *Microstructural Science* 9 (1981), pp. 107–118. ISSN: 0026-0800. DOI: 10.1016/0026-0800(81)90035-5.

[36] G.K. Sujan et al. „Interfacial reaction, ball shear strength and fracture surface analysis of lead-free solder joints prepared using cobalt nanoparticle doped flux“. In: *Journal of Alloys and Compounds* 695 (2017), pp. 981–990. ISSN: 0925-8388. DOI: https://doi.org/10.1016/j.jallcom.2016.10.219. URL: https://www.sciencedirect.com/science/article/pii/S0925838816333540.

[37] G. Zeng, S. Xue, L. Zhang, et al. „A review on the interfacial intermetallic compounds between Sn–Ag–Cu based solders and substrates“. In: *Journal of Materials Science: Materials in Electronics* 21.5 (2010), pp. 421–440. DOI: 10.1007/s10854-010-0086-y. URL: https://doi.org/10.1007/s10854-010-0086-y.

[38] M.N. Bashir and A.S.M.A. Haseeb. „Grain size stability of interfacial intermetallic compound in Ni and Co nanoparticle-doped SAC305 solder joints under electromigration“. In: *Journal of Materials Science: Materials in Electronics* 33 (2022), pp. 14240–14248. DOI: 10.1007/s10854-022-08352-0. URL: https://doi.org/10.1007/s10854-022-08352-0.

[39] T. Mouratidis. „The Effect of Joint Thickness on Intermetallic Growth in the In52Sn48(Liquid)/Cu(Solid) Diffusion Couple“. In: *Journal of Electronic Materials* 53.1 (2024), pp. 418–431. DOI: 10.1007/s11664-023-10764-5. URL: https://doi.org/10.1007/s11664-023-10764-5.

[40] S.L. Tay, A. S. M. A Haseeb, and Mohd Johan. „Effect of addition Cobalt nanoparticles on Sn-Ag-Cu lead-free solder“. In: *2010 12th Electronics Packaging Technology Conference, EPTC 2010* (Dec. 2010), pp. 433–436. DOI: 10.1109/EPTC.2010.5702678.

[41] Ramani Mayappan et al. „Activation energy for Cu–Sn intermetallic in CNT-reinforced Sn–1.0Ag–0.5Cu solder“. In: *Soldering Surface Mount Technology* 32.2 (2020), pp. 65–72. DOI: 10.1108/SSMT-07-2019-0025. URL: https://doi.org/10.1108/SSMT-07-2019-0025.

[42] W.-M. Chen, P. McCloskey, and S.C. O'Mathuna. „Isothermal aging effects on the microstructure and solder bump shear strength of eutectic Sn37Pb and Sn3.5Ag solders“. In: *Microelectronics Reliability* 46.5 (2006), pp. 896–904. ISSN: 0026-2714. DOI: https://doi.org/10.1016/j.microrel.2005.06.006. URL: https://www.sciencedirect.com/science/article/pii/S0026271405001356.

[43] N.M. Poon et al. „Residual shear strength of Sn-Ag and Sn-Bi lead-free SMT joints after thermal shock“. In: *IEEE Transactions on Advanced Packaging* 23.4 (2000), pp. 708–714. ISSN: 1521-3323. DOI: 10.1109/6040.883762.

[44] Jing-Hua Zheng et al. „Comparative Study of Creep and Stress Relaxation Behaviour during Ageing of 7050 Aluminum Alloy“. In: *Metals* 13.4 (2023). ISSN: 2075-4701. DOI: 10.3390/met13040778. URL: https://www.mdpi.com/2075-4701/13/4/778.

[45] P. Zimprich, U. Saeed, B. Weiss, et al. „Constraining Effects of Lead-Free Solder Joints During Stress Relaxation“. In: *Journal of Electronic Materials* 38 (2009), pp. 392–399. DOI: 10.1007/s11664-008-0604-3.

[46] X. Zhao, W. Zhang, C. Wang, et al. „Effect of Aging Time on Ductile–Brittle Transition Behaviors of Sn-3.5Ag Solder“. In: *Journal of Electronic Materials* 52 (2023). Issue Date: January 2023, pp. 471–476. DOI: 10.1007/s11664-022-10013-1.

[47] Karuna Ratnakaran Athul et al. „A Review of Different Creep Mechanisms in Mg Alloys Based on Stress Exponent and Activation Energy“. In: *Advanced Engineering Materials* 18.5 (2016), pp. 770–794. DOI: https://doi.org/10.1002/adem.201500393. eprint: https://advanced.onlinelibrary.wiley.com/doi/pdf/10.1002/adem.201500393. URL: https://advanced.onlinelibrary.wiley.com/doi/abs/10.1002/adem.201500393.

[48] Günter Gottstein and Sandra Korte-Kerzel. *Materialwissenschaft und Werkstofftechnik: Physikalische Grundlagen*. 5th ed. Life Science and Basic Disciplines (German Language). Springer Vieweg Berlin, Heidelberg, 2025. ISBN: 978-3-662-68325-5. DOI: 10.1007/978-3-662-68326-2. URL: https://doi.org/10.1007/978-3-662-68326-2.

[49] Julien Magnien. „Investigation of mechanical behavior and failure mechanisms in miniaturized solder interconnects“. en. In: (2015). DOI: 10.25365/THESIS.37284. URL: https://utheses.univie.ac.at/detail/33045.

List of Figures

List of Tables

Appendix

Measurements of the IMC thickness

	Cu_3Sn thickness in μm			Cu_6Sn_5 thickness in μm			$Cu_3Sn + Cu_6Sn_5$ thickness in μm		
	above	below	total	above	below	total	above	below	total
	0.382	0.380	-	-	-	-	3.524	4.192	-
0.00 %	0.356	0.401	-	-	-	-	4.316	3.805	-
	-	-	-	-	-	-	4.254	4.143	-
Average	0.369	0.391	0.380	3.785	3.786	3.659	4.032	4.047	4.039
SD	0.019	0.015	0.019	0.441	0.211	0.310	0.441	0.210	0.309
	0.371	0.392	-	-	-	-	2.968	2.450	-
0.10 %	0.321	0.402	-	-	-	-	2.803	2.229	-
	-	-	-	-	-	-	2.709	3.086	-
Average	0.346	0.397	0.372	2.596	2.323	2.336	2.827	2.588	2.707
SD	0.035	0.007	0.036	0.136	0.445	0.323	0.131	0.445	0.321
	0.383	0.356	-	-	-	-	4.011	3.732	-
0.25 %	0.346	0.361	-	-	-	-	3.476	2.584	-
	-	-	-	-	-	-	3.433	3.059	-
Average	0.365	0.358	0.361	3.397	2.886	3.021	3.640	3.125	3.382
SD	0.026	0.003	0.016	0.323	0.577	0.505	0.322	0.577	0.504
	0.335	0.384	-	-	-	-	2.823	2.540	-
0.50 %	0.385	0.377	-	-	-	-	3.873	3.818	-
	-	-	-	-	-	-	3.676	3.617	-
Average	0.360	0.381	0.370	3.217	3.071	3.021	3.457	3.325	3.391
SD	0.035	0.005	0.024	0.559	0.687	0.565	0.558	0.687	0.564
	0.330	0.388	-	-	-	-	2.878	3.685	-
1.00 %	0.392	0.388	-	-	-	-	2.977	-	-
	-	-	-	-	-	-	-	-	-
Average	0.361	0.388	0.375	2.566	2.909	2.805	2.927	3.684	3.180
SD	0.044	0.000	0.030	0.125	-	0.428	0.070	-	0.440

Table A16: Measured IMC thickness values for the as reflow samples.

	Cu_3Sn thickness in μm			Cu_6Sn_5 thickness in μm			$Cu_3Sn + Cu_6Sn_5$ thickness in μm		
	above	below	total	above	below	total	above	below	total
0.00 %	0.650	0.847	-	4.274	3.903	-	-	-	-
	0.521	0.818	-	3.798	4.053	-	-	-	-
	0.510	0.902	-	-	-	-	-	-	-
Average	0.560	0.856	0.708	3.778	3.642	4.007	4.338	4.498	4.715
SD	0.078	0.043	0.171	0.337	0.106	0.206	0.345	0.114	0.268
0.10 %	0.643	0.731	-	3.056	2.447	-	-	-	-
	0.617	0.795	-	-	-	-	-	-	-
	0.530	0.703	-	3.197	2.381	-	-	-	-
Average	0.597	0.743	0.670	2.943	2.340	2.770	3.539	3.082	3.440
SD	0.059	0.047	0.093	0.099	0.047	0.399	0.116	0.067	0.409
0.25 %	0.630	0.731	-	3.031	3.823	-	-	-	-
	0.624	0.880	-	3.382	3.757	-	-	-	-
	0.642	0.772	-	2.897	3.705	-	-	-	-
Average	0.632	0.794	0.713	3.103	3.762	3.433	3.735	4.556	4.146
SD	0.009	0.077	0.102	0.251	0.059	0.396	0.251	0.097	0.408
0.50 %	0.632	0.657	-	3.775	3.152	-	-	-	-
	0.639	0.727	-	3.303	-	-	-	-	-
	0.659	0.790	-	-	3.439	-	-	-	-
Average	0.643	0.724	0.684	3.422	3.296	3.417	4.065	4.020	4.101
SD	0.014	0.066	0.062	0.333	0.203	0.265	0.334	0.214	0.273
1.00 %	0.590	0.672	-	3.221	3.057	-	-	-	-
	0.676	0.683	-	3.315	-	-	-	-	-
	0.615	0.677	-	-	-	-	-	-	-
Average	0.627	0.677	0.652	3.268	3.057	3.198	3.895	3.734	3.850
SD	0.044	0.006	0.040	0.067	-	0.131	0.080	-	0.410

Table A17: Measured IMC thickness values for the 120 °C 20 days aged samples.

	Cu_3Sn thickness in μm			Cu_6Sn_5 thickness in μm			$Cu_3Sn + Cu_6Sn_5$ thickness in μm		
	above	below	total	above	below	total	above	below	total
0.00 %	3.649	3.415	-	5.432	4.870	-	-	-	-
	3.521	3.405	-	-	-	-	-	-	-
	3.558	-	-	-	-	-	-	-	-
Average	3.576	3.410	3.509	5.432	4.870	5.151	9.008	8.280	8.661
SD	0.066	0.080	0.102	-	-	0.397	-	-	0.410
0.10 %	3.466	3.538	-	3.472	3.661	-	-	-	-
	3.408	3.536	-	3.809	4.149	-	-	-	-
	3.493	3.430	-	3.556	3.978	-	-	-	-
Average	3.455	3.501	3.478	3.612	3.930	3.771	7.068	7.431	7.249
SD	0.044	0.062	0.054	0.175	0.247	0.259	0.181	0.255	0.264
0.25 %	3.515	3.292	-	4.741	5.466	-	-	-	-
	3.388	3.270	-	4.240	5.564	-	-	-	-
	3.538	3.429	-	4.539	5.525	-	-	-	-
Average	3.480	3.330	3.405	4.506	5.518	5.012	7.987	8.848	8.417
SD	0.081	0.086	0.111	0.252	0.049	0.577	0.265	0.100	0.588
0.50 %	3.325	3.016	-	5.427	6.609	-	-	-	-
	3.287	3.343	-	5.001	7.208	-	-	-	-
	3.335	3.158	-	5.060	6.722	-	-	-	-
Average	3.316	3.172	3.244	4.881	6.666	5.763	9.008		
SD	0.026	0.164	0.131	0.170	0.080	1.020	0.232	0.358	1.028
1.00 %	3.210	3.329	-	5.436	6.438	-	-	-	-
	2.928	3.045	-	5.185	6.312	-	-	-	-
	2.982	3.112	-	5.865	7.499	-	-	-	-
Average	3.040	3.162	3.101	5.311	6.375	5.842	8.535	9.912	8.944
SD	0.150	0.148	0.149	0.177	0.090	0.625	0.375	0.669	0.642

Table A18: Measured IMC thickness values for the 180 °C 10 days aged samples.

	Cu_3Sn thickness in μm			Cu_6Sn_5 thickness in μm			$Cu_3Sn + Cu_6Sn_5$ thickness in μm		
	above	below	total	above	below	total	above	below	total
	4.445	4.348	-	6.392	6.675	-	-	-	-
0.00 %	4.188	4.459	-	6.713	6.298	-	-	-	-
	4.272	4.615	-	5.980	7.173	-	-	-	-
Average	4.302	4.474	4.388	6.362	6.715	6.538	10.663	11.189	10.926
SD	0.131	0.134	0.151	0.367	0.439	0.411	0.390	0.459	0.438
	4.392	4.346	-	4.550	6.183	-	-	-	-
0.10 %	4.316	4.348	-	4.597	6.179	-	-	-	-
	4.272	4.453	-	4.981	5.445	-	-	-	-
Average	4.327	4.382	4.355	4.709	5.936	5.322	9.036	10.318	9.677
SD	0.061	0.061	0.062	0.237	0.425	0.739	0.244	0.429	0.742
	4.205	4.744	-	5.119	6.133	-	-	-	-
0.25 %	4.561	4.281	-	5.024	5.745	-	-	-	-
	4.245	4.187	-	6.117	6.453	-	-	-	-
Average	4.337	4.404	4.371	5.420	6.111	5.765	9.757	10.515	10.136
SD	0.195	0.298	0.228	0.605	0.354	0.583	0.636	0.463	0.626
	4.107	4.333	-	6.051	6.404	-	-	-	-
0.50 %	4.370	4.553	-	6.480	6.784	-	-	-	-
	4.247	4.078	-	6.180	7.007	-	-	-	-
Average	4.241	4.321	4.281	6.237	6.732	6.484	10.478	11.053	10.766
SD	0.132	0.238	0.178	0.220	0.305	0.361	0.257	0.387	0.402
	4.164	4.172	-	5.888	6.734	-	-	-	-
1.00 %	4.282	4.009	-	5.863	6.948	-	-	-	-
	4.053	4.246	-	6.813	6.889	-	-	-	-
Average	4.166	4.142	4.154	6.188	6.857	6.523	10.355	10.999	10.677
SD	0.115	0.122	0.106	0.541	0.111	0.506	0.553	0.164	0.517

Table A19: Measured IMC thickness values for the 180 °C 20 days aged samples.

Calculation of the diffusion coefficients and activation energy

	Slope			Diffusion coefficient in $m^2\ s^{-1}$		
Co NP	Cu_3Sn	Cu_6Sn_5	total IMC	Cu_3Sn	Cu_6Sn_5	total IMC
0.00%	3.11E-03	2.23E-03	5.34E-03	9.65E-18	4.98E-18	2.85E-17
0.10%	3.09E-03	2.32E-03	5.40E-03	9.53E-18	5.36E-18	2.92E-17
0.25%	3.11E-03	2.13E-03	5.24E-03	9.66E-18	4.53E-18	2.74E-17
0.50%	3.03E-03	2.68E-03	5.72E-03	9.19E-18	7.21E-18	3.27E-17
1.00%	2.93E-03	2.88E-03	5.81E-03	8.58E-18	8.30E-18	3.38E-17

Table A20: Slope and diffusion coefficient for 180 °C.

	Slope			Diffusion coefficient in $m^2\ s^{-1}$		
Co NP	Cu_3Sn	Cu_6Sn_5	total IMC	Cu_3Sn	Cu_6Sn_5	total IMC
0.00%	2.54E-04	2.70E-04	5.24E-04	6.47E-20	7.27E-20	2.75E-19
0.10%	2.31E-04	3.37E-04	5.68E-04	5.33E-20	1.14E-19	3.23E-19
0.25%	2.73E-04	3.19E-04	5.92E-04	7.44E-20	1.02E-19	3.50E-19
0.50%	2.43E-04	3.07E-04	5.50E-04	5.91E-20	9.44E-20	3.03E-19
1.00%	2.15E-04	3.04E-04	5.19E-04	4.63E-20	9.25E-20	2.70E-19

Table A21: Slope and diffusion coefficient for 120 °C.

	Slope			Activatin engergy in $kJ\ mol^{-1}$		
Co NP	Cu_3Sn	Cu_6Sn_5	total IMC	Cu_3Sn	Cu_6Sn_5	total IMC
0.00 %	-14849	-12541	-13774	123	104	115
0.10 %	-15389	-11435	-13367	128	95	111
0.25 %	-14440	-11260	-12938	120	94	108
0.50 %	-14975	-12864	-13890	125	107	115
1.00 %	-15498	-13345	-14333	129	111	119

Table A22: Slope and activation energy

Measurements of the push-off shear tests

Co NP	Load in N	Shear strength in MPa
0.00 %	478.30	40.5
	653.52	53.8
	708.36	57.7
	796.36	66.2
	675.71	56.0
	495.73	41.4
	578.33	49.6
	652.74	53.2
	561.49	45.8
	539.65	45.5
Average	614.02	51.0
SD	100.55	8.0
0.10 %	659.57	54.4
	483.33	40.7
	732.61	59.0
	913.61	73.3
	844.68	68.4
	620.77	50.8
	763.45	62.2
	650.30	53.7
	639.77	56.4
	632.38	54.9
Average	694.05	57.4
SD	123.30	9.1
0.25 %	653.99	53.1
	880.29	72.6
	715.29	60.3
	727.72	58.4
	536.80	43.8
	647.40	53.0
	578.56	47.3
	734.55	59.6
	789.16	63.9
	765.49	62.1
Average	702.93	57.4
SD	101.72	8.4

Table A23: Load and shear stength of the push-off shear tests, part 1.

Co NP	Load in N	Shear strength in MPa
0.50 %	520.98	42.6
	562.97	45.2
	598.62	48.5
	728.17	58.9
	685.74	55.4
	487.42	40.6
	607.57	50.4
	731.14	58.7
	631.47	51.1
	730.22	58.2
Average	628.43	51.0
SD	88.94	6.8
1.00 %	549.09	47.2
	555.91	46.4
	695.17	57.7
	551.82	46.1
	581.74	48.1
Average	586.75	49.1
SD	61.99	4.9

Table A24: Load and shear stength of the push-off shear tests, part 2.

Measured shear strength of the pre- and sheartests of the SRT samples.

Shear strength	Co NP			
in MPa	0.00 %	0.10 %	0.25 %	1.00 %
PT1	29.8	32.2	30.8	31.0
PT2	-	34.1	30.7	30.8
ST1	32.6	33.9	32.0	29.5
ST2	32.4	35.6	31.5	31.1
ST3	31.6	32.1	31.8	26.1
Avearage	31.6	33.6	31.4	29.7
SD	1.3	1.5	0.6	2.1

Table A25: Shear strength of the pre- and sheartests at room temperature for the as reflow samples at various cobalt NP contents.

Shear strength	Co NP			
in MPa	0.00 %	0.10 %	0.25 %	1.00 %
PT1	17.0	19.2	17.5	19.6
PT2	18.8	20.8	17.9	20.7
ST1	16.7	19.5	17.0	17.9
ST2	16.0	20.4	16.7	15.1
ST3	-	20.0	-	19.8
Avearage	17.1	20.0	17.3	18.6
SD	1.2	0.6	0.5	2.2

Table A26: Shear strength of the pre- and sheartests at 100 °C for the as reflow samples at various cobalt NP contents.

Shear strength	Co NP			
in MPa	0.00 %	0.10 %	0.25 %	1.00 %
PT1	13.8	14.1	12.1	12.7
PT2	-	13.3	13.3	13.4
ST1	10.8	14.8	13.2	11.7
ST2	10.8	12.9	12.8	12.0
ST3	-	13.3	11.7	10.8
Avearage	11.8	13.7	12.6	12.1
SD	1.7	0.8	0.7	1.0

Table A27: Shear strength of the pre- and sheartests at 150 °C for the as reflow samples at various cobalt NP contents.

Shear strength	Co NP			
in MPa	0.00 %	0.10 %	0.25 %	1.00 %
PT1	21.2	22.2	22.5	21.0
PT2	-	21.8	23.3	22.8
ST1	20.9	25.0	22.7	24.6
ST2	22.0	22.8	22.7	18.4
ST3	-	21.6	22.2	24.0
Avearage	21.4	22.7	22.7	22.2
SD	0.6	1.4	0.4	2.5

Table A28: Shear strength of the pre- and sheartests at room temperature for the aged samples at various cobalt NP contents.

Shear strength	Co NP			
in MPa	0.00 %	0.10 %	0.25 %	1.00 %
PT1	12.7	12.5	13.5	12.8
PT2	-	13.8	11.4	12.0
ST1	11.2	14.2	13.1	11.3
ST2	11.2	11.9	12.1	12.6
ST3	-	13.3	13.3	12.7
Avearage	11.7	13.2	12.7	12.3
SD	0.9	0.9	0.9	0.6

Table A29: Shear strength of the pre- and sheartests at 100 °C for the aged samples at various cobalt NP contents.

Shear strength	Co NP			
in MPa	0.00 %	0.10 %	0.25 %	1.00 %
PT1	9.4	9.2	9.5	8.6
PT2	-	10.6	9.0	9.2
ST1	8.9	9.1	9.2	8.1
ST2	8.8	9.8	8.3	9.2
ST3	-	9.1	9.3	8.0
ST4	-	9.3	7.6	8.9
ST5	-	9.2	8.6	7.9
Avearage	9.0	9.5	8.8	8.6
SD	0.3	0.6	0.7	0.6

Table A30: Shear strength of the pre- and shear tests at 150 °C for the aged samples at various cobalt NP contents.

Relaxation behaviour of the SRT samples.

Thermal treatment	Testing temperature	Relaxation after 1 h in % Co NP 0.00 %	0.10 %	0.25 %	1.00 %
as reflow	RT	83.1	81.8	82.7	71.9
		92.2	74.3	86.0	76.8
		81.8	75.6	75.4	62.6
	Average	85.7	77.2	81.4	70.4
	SD	5.7	4.0	5.4	7.2
	100 °C	75.5	77.1	75.0	66.5
		79.3	67.4	77.3	60.0
		-	76.8	-	76.2
	Average	77.4	73.8	76.1	67.6
	SD	2.6	5.5	1.6	8.2
	150 °C	52.7	59.8	61.2	54.3
		62.7	54.6	67.0	47.6
		-	48.7	55.6	50.5
	Average	57.7	54.4	61.3	50.8
	SD	7.0	5.6	5.7	3.4
aged	RT	50.7	61.5	57.2	58.0
		60.7	59.6	60.1	56.3
		-	71.2	53.4	64.8
	Average	55.7	64.1	56.9	59.7
	SD	7.1	6.2	3.3	4.5
	100 °C	46.6	53.8	47.6	62.7
		48.5	45.7	39.5	63.9
		-	55.7	56.0	58.4
	Average	47.5	51.7	47.7	61.7
	SD	1.4	5.3	8.3	2.9
	150 °C	51.2	42.2	53.0	33.8
		50.2	43.9	41.6	43.8
		-	34.9	60.7	39.1
		-	37.5	42.1	50.2
		-	40.4	48.4	51.7
	Average	50.7	39.8	49.2	43.7
	SD	0.7	3.6	8.0	7.5

Table A31: Relaxation after 1 h for differnt thermal treatments and testing temperatures